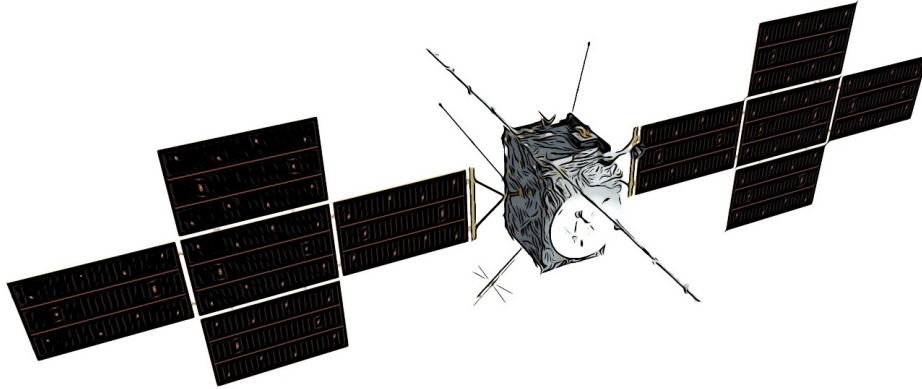




TÉCNICO
LISBOA



Launching the Radiation Hard Electron Monitor aboard the ESA JUICE mission

Francisca Ferreira Santos

Thesis to obtain the Master of Science Degree in

Engineering Physics

Supervisors: Prof. Dr. Patrícia Carla Serrano Gonçalves
Dr. Marco Gui Alves Pinto

Examination Committee

Chairperson: Prof. Mário João Martins Pimenta

Supervisor: Dr. Marco Gui Alves Pinto

Members of the Committee: Dr. Elias Roussos

Prof. Bernardo António Neto Gomes Baptista Tomé

May 2024

Declaration

I declare that this document is an original work of my own authorship and that it fulfills all the requirements of the Code of Conduct and Good Practices of the Universidade de Lisboa.

Acknowledgements

First and foremost, I would like to thank both my supervisors, Patrícia and Marco, whose guidance and support were indispensable for the realisation of this work. A special thanks to Marco for the invaluable conversations, feedback, dedication, and availability, especially during the challenging early months of parenthood. I extend my thanks to LIP and everyone from the institution that, directly or indirectly, contributed to the making of this work.

A huge thanks to my family, specially my parents, for shaping me into who I am today and always did the impossible to support me. A thank you to my brother who has always been just a call away; it has been a pleasure to grow up with you. Thanks to all my friends in Viseu for all the companionship throughout all these years.

For the ones I shared the university experience with, thank you for all the fun and shared struggles throughout the course. To the close friends that I made in these years, thank you for all the endless talking, working and shared adventures, it would not be the same without you. Lastly, a special thanks to Rafael, that listened to all my complaints and worries during this process and still did not run away. Thank you for sharing this journey with me.

Resumo

"Exploradora das Luas Geladas de Júpiter", JUICE, lançada a abril 2024, é uma missão da Agência Espacial Europeia (ESA) que visa explorar o Sistema Joviano. A missão chegará a Jupiter em 2031 após 7.6 anos de percurso interplanetário e, durante 3.5 anos, permanecerá em volta da gigante gasosa e das luas Galileanas.

A bordo da JUICE, como parte dos instrumentos de manutenção e responsável pela monitorização dos níveis de radiação, encontra-se o "Monitor de Eletrões Resistentes a Radiação", RADEM. É constituído por quatro detetores: Detetor Stack Eletrões, EDH; Detetor Stack Protões, PDH; Detetor Stack Iões, HIDH; Detetor de Direcionalidade (DDH). O monitor foi desenhado para medir eletrões (0.3 - 40 MeV), protões (5 - 250 MeV) e iões pesados, desde o Hélio ao Oxigénio (8 - 670 MeV). O DDH, foco deste trabalho, irá medir a distribuição angular dos eletrões incidentes. Durante toda a missão, o RADEM vai contribuir para vários estudos, entre os quais sobre Raios Cósmicos Galácticos (GCRs) e Partículas Solares Energéticas (SEPs).

Nesta tese, as observações feitas pelo DDH de GCRs e SEPs são analisadas. Para uma melhor compreensão dos dados de voo, as funções de resposta de energia do DDH para protões incidentes são apresentadas e detalhadamente analisadas. Com os dados de GCR, informação detalhada sobre a operação em voo de cada sensor do DDH é extraída e a sua validação com modelos teóricos é feita. Para concluir o trabalho, um SEP ocorrido em março 2024 foi selecionado para uma análise da sua distribuição angular.

Palavras-Chave: JUICE, RADEM, Detetor de Direcionalidade, Protões, Raios Cósmicos Galácticos, Partículas Solares Energéticas

Abstract

JUpiter ICy moons Explorer (JUICE), launched in 14th April 2023, is an European Space Agency (ESA) mission to explore the Jovian System. The mission will reach Jupiter in 2031 after an interplanetary cruise of 7.6 years and it will spend 3.5 years touring the giant planet and the Galilean moons.

On board the JUICE spacecraft, as part of the payload support instruments and responsible for the radiation monitoring, is the RADiation Hard Electron Monitor (RADEM). RADEM is composed of four detectors: Electron Detector Head (EDH), Proton Detector Head (PDH), Heavy Ion Detector Head (HIDH) and Directionality Detector Head (DDH). It is designed to measure electrons (0.3 to 40 MeV), protons (5 to 250 MeV) and heavy ions, from Helium to Oxygen (8 to 670 MeV). The DDH, the focus of this work, will measure the angular distribution of incoming electrons. Throughout the mission, RADEM will contribute to various scientific studies including those of Galactic Cosmic Rays (GCRs) and Solar Energetic Particles (SEPs).

In this thesis, the DDH observations of GCRs and SEPs are analysed. For a better comprehension of the flight data, the energy response function of each DDH sensor for incoming protons are presented and thoroughly analysed. With the GCR data, detailed information about each DDH sensor's operation in flight is extracted and its validation with theoretical models is conducted. To conclude the work, a SEP event which occurred in March 2024 was selected for an angular distribution analysis.

Keywords: JUICE, RADEM, Directionality Detector, Protons, Galactic Cosmic Rays, Solar Energetic Particles

Contents

Contents	xi
List of Figures	xiii
List of Tables	xvi
Acronyms	xvii
1 Introduction	1
1.1 The JUICE mission	1
1.1.1 Mission Profile	2
1.1.2 RADEM on the JUICE mission	2
1.2 Thesis Outline	4
2 Interplanetary and Jovian Radiation Environment	5
2.1 Solar Particle Events	5
2.2 Galactic Cosmic Rays	6
2.3 Jovian Magnetosphere	8
2.3.1 Trapped Particles	9
3 RADIation hard Electron Monitor	13
3.1 Working Principle	13
3.1.1 Interaction of particles with matter	14
3.1.2 Silicon Detectors	15
3.1.3 Front-End Eletronics	16
3.2 Detectors	16
3.2.1 Proton and Electron Detector Heads	16
3.2.2 Heavy Ion Detector Head	18
3.2.3 Directionality Detector Head	19
3.3 Flight Configuration	20
4 DDH Response Functions	21
4.1 Geant4 Simulation	21

4.1.1	RADEM model	22
4.2	Response Functions	22
4.2.1	Proton Response Functions	24
5	DDH Flight Data Analysis	31
5.1	Galactic Cosmic Rays Data	31
5.1.1	Sensor Rate Variation	31
5.1.2	Data Validation	37
5.1.2.1	Simulated LT scan	39
5.1.2.2	Commissioning LT scan	40
5.2	Solar Energetic Particle Events	42
5.2.1	Rate correction and Background Subtraction	44
5.2.2	Time evolution of event	46
6	Summary and outlook	51
6.1	Future Work	52
A	Complementary figures - Response Functions	57
B	Complementary data - GCR	59
	Bibliography	63

List of Figures

1.1	Chronograph of JUICE mission events. Adapted from [12].	2
2.1	Solar cycle sunspot number progression. Adapted from [14].	6
2.2	Primary cosmic radiation fluxes of nuclei plotted as particles per energy-per-nucleus vs energy-per-nucleus. From [18].	7
2.3	Schematic comparison of Jupiter's and Earth's magnetosphere [21].	8
2.4	Comparison between the integral electron fluxes in Earth Geosynchronous Orbit and Europa <peak 24h> [24].	9
2.5	Earth's trapped proton environment (left) [25] and trapped electron environment (right) [26].	10
2.6	Expected proton and electron integral fluxes during different phases of the JUICE mission. [11]	10
2.7	Electron Local Pitch Angle distributions of two electron channels of EDP in two different locals during a Galileo encounter with Ganymede (G29) at 28 December 2000. [29]. . . .	11
3.1	RADEM STEP geometry.	13
3.2	Proton and α particle stopping power in Silicon and electron total, radiative and collisional stopping power in Silicon [35, 36, 37].	14
3.3	Schematic of PDH (left), EDH (right) [24].	17
3.4	Schematic of HIDH [24].	18
3.5	Cut view of the DDH (left) [24] and DDH sensor on-flight top-view serialization (right) [40]. The color code corresponds to the different zenith direction: green - 0° ; yellow - 22.5° ; orange - 45° ; red - 67.5° ; blue - background sensors.	19
4.1	Views of the JUICE spacecraft model and RADEM's placement.	22
4.2	Mean deposited energy as a function of proton's incident energy for sensors with same zenith direction.	24
4.3	Average proton response function of sensors with same zenith direction.	26
4.4	Average proton response function of sensors with same zenith direction and respective background sensor.	27
4.5	Average proton response function of sensors with 67.5° zenith direction for three values of LT.	28

4.6	Average proton response function of sensors with same zenith direction and respective background sensor.	29
5.1	Rate per unit area during the month of October for nine selected sensors of the DDH. . .	32
5.2	Sensor average rates of GCR during different time periods from September 2023 to April 2024.	33
5.3	GCR proton differential fluxes computed with PyCreme for five selected months.	37
5.4	Average rate per unit area for each DDH sensor during the month of October and simulated rates using PyCreme. The flight data is coloured according to the zenith angle of the sensor: 0° (green), 22.5° (blue), 45° (orange) and 67.5° (red).	38
5.5	Simulated rates using PyCreme for the period from April 2023 to January 2024 and flight data of the GCR average rate from each month. These values are averaged over the sensors with same zenith direction.	39
5.6	Relation between LT value and count rate registered in four different sensors during the NECP, one corresponding to a different zenith direction.	41
5.7	42
5.8	Count rate per area of DDH sensors during the March SEP event with integration time of 30 minutes.	43
5.9	Correction factor applied to three selected sensors during the March SEP event, each from a different zenith direction, 22.5°:80°, 45°:240° and 67.5°:300°.	44
5.10	March SEP's corrected rate per unit area of the DDH sensors.	45
5.11	Rate per unit area of the March SEP event registered by the sensors D1, D3, D4 and D5 of the PDH. E_0 is the cut-off energy of the given sensor for protons.	46
5.12	Rate per unit area of the March SEP event registered by the sensor 0°:0° and chosen time intervals for posterior analysis.	47
5.13	Average rate per unit area ($s^{-1}cm^{-2}$) of the DDH sensors for the chosen intervals. Each colour bar corresponds to a different zenith direction: 22.5° (blue), 45° (orange) and 67.5°(red). The angular values represent the azimuth direction of each sensor.	48
5.14	Average electron count rates over sensors with same zenith angle for two phases of the JUICE mission. Electrons were simulated omnidirectionality and according to the expected fluxes for each phase. [40]	49
A.1	Deposited energy as a function of the proton incident energy for all DDH sensors.	57
A.2	Proton energy response function of all DDH sensors.	57
A.3	Proton response function of the central sensor, 0° zenith direction for three values of LT and HT.	58
A.4	Average proton response function of sensors with 22.5° zenith direction for three values of LT and HT.	58
A.5	Average proton response function of sensors with 45° zenith direction for three values of LT and HT.	58

B.1	Rate per unit area during the month of October for the central sensor, $0^\circ:0^\circ$, and background sensors of all zeniths of the DDH.	59
B.2	Rate per unit area during the month of October for the nine azimuth sensors with zenith 22.5° of the DDH.	59
B.3	Rate per unit area during the month of October for the nine azimuth sensors with zenith 45° of the DDH.	60
B.4	Rate per unit area during the month of October for the nine azimuth sensors with zenith 67.5° of the DDH.	60

List of Tables

3.1	Energy ranges of detection of RADEM for protons, electrons and heavy ions.	13
3.2	Minimum threshold above noise, maximum threshold, and step size for the three types of thresholds.	16
3.3	Material, dimensions and theoretical proton and electron energy cutoff of absorbers and sensors of PDH. Numbering follows Figure 3.3, from top to bottom.	17
3.4	Material, dimensions and theoretical proton and electron energy cutoff of absorbers and sensors of EDH. Numbering follows Figure 3.3, from top to bottom.	18
3.5	Material and dimensions of absorbers and sensors of HIDH. Numbering follows Figure 3.4, from top to bottom.	18
3.6	Material, dimensions and theoretical proton and electron energy cutoff of absorbers and sensors of DDH.	19
3.7	Thresholds of the DDH for the initial stage of the cruise phase.	20
4.1	Thickness of the 6-side Aluminum box as the equivalent shielding of JUICE spacecraft at RADEM's faces.	22
4.2	Energy interval and correspondent number of generated protons and electrons.	23
5.1	Average rate and standard deviation of DDH sensors with same zenith direction for the periods considered from September 2023 to April 2024.	34
5.2	Average rate error for each sensor in the selected period of September 2023.	35
5.3	Correction factor to apply to each DDH sensor data.	36
5.4	Mean value of the average flight data rate for sensors with same zenith direction and simulated rate during the month of October, 2023. Additional ratio between these two values.	38
5.5	Linear regression parameters for the four sensors under study, relating DAC and MeV units.	41
B.1	Correction factor computed for each DDH sensor (September, October and November). . .	61
B.2	Correction factor computed for each DDH sensor (December, January and February). . .	61
B.3	Correction factor computed for each DDH sensor (March and April).	61

Acronyms

ESA	European Space Agency
JUICE	JUpiter ICy moons Explorer
EPD	Energetic Particle Detector
RADEM	RADiation hard Electron Monitor
PEP	Particle Environment Package
EDH	Electron Detector Head
PDH	Proton Detector Head
HIDH	Heavy Ion Detector Head
DDH	Directionality Detector Head
SEP	Solar Energetic Particles
GCR	Galactic Cosmic Rays
CME	Coronal Mass Ejections
SF	Solar Flares
JOSE	JOvian Specification Environment
LPA	Local Pitch Angle
HG	High-gain ASIC channels
LG	Low-gain ASIC channels
HT	High Threshold
LT	Low Threshold
DAC	Digital-to-Analogue Converter
FOV	Field-Of-View
GEANT4	GEometry ANd Tracking
CAD	Computer Aided Design
STEP	Standard for The Exchange of Product Data
GDML	Geometry Description Markup Language
NECP	Near Earth Commissioning Phase
ISO	International Standard Organisation
JoEE	Jovian Electron Electrons

1 | Introduction

Humanity has benefited much from space exploration. Not only through the development of new technologies that can be used in different sectors of the economy and society, but also by greatly advancing our understanding of the Universe. However, the space environment poses a significant challenge to every spacecraft and therefore, space exploration. One of the major technological consequences of planetary space environment is the radiation impact on spacecraft equipment, both in terms of electromagnetic waves and particles [1]. As a result, modelling and monitoring the radiation environment is a critical task to prevent anomalies and extend the longevity of space missions.

On the 14th April 2023, the European Space Agency (ESA) launched the JUpiter ICy moons Explorer (JUICE) spacecraft. This mission will have as target the Jovian System which encompasses Jupiter, its rings and moons. While the radiation environment on Earth has been widely researched, the same cannot be said for the Jovian system. Over the years, many missions, including Pioneer 10-11 [2, 3], Voyager 1-2 [4], Ulisses [5], Cassini and New Horizons, have visited the Jovian system. However, they did so only for brief periods of time on their way to other targets. So far, only the Galileo mission [6], which carried the Energetic Particle Detector (EPD) and arrived in Jupiter in 1995, was launched particularly to explore the Jovian System and had the capability to do extensive radiation studies (during 8 years). More recently, JUNO [7], a NASA mission, launched in 2011 had the goal of studying Jupiter, although lacked the capability to analyse the radiation environment. Nonetheless, these missions showed a harsh radiation environment with much larger fluxes of electrons than on Earth and with much larger energies. On board of the spacecraft, as part of the payload support instruments and responsible for the radiation monitoring, is the RADiation Hard Electron Monitor (RADEM), capable of measuring electrons, protons and, to some extent, ions [8].

1.1 The JUICE mission

The formation of habitable worlds surrounding gas giants is the underlying premise of JUICE. After the Galileo's mission showed strong evidence of the existence of oceans hidden beneath the icy crusts of Europa, Ganymede and Callisto, icy worlds were hypothesised to be hosts of ecosystems both in and outside the Solar System [9]. Even though these moons are not in the Goldilocks zone, known as the habitable zone, it is believed they have the conditions to sustain life: liquid water, chemical compounds, energy source and time stability [10]. As a result, JUICE has as key scientific objectives the compositional

mapping of the moons' surface and sub-surface, namely the hypothesised sub-surface water reservoirs, as well as the investigation of the physical properties of the icy crusts.

The last part of the mission will focus on Ganymede. This moon will not only provide information on the evolution and possible habitability of frozen moons in general, but also on the role it plays within the Jovian System. Because of its unique internal magnetic field and interactions with the surroundings, it was chosen as the focal point of the mission. Callisto and Europa will round out the Galilean moons comparison. Callisto will provide data from the early Jovian System and Europa will supply information from recent active zones, allowing researchers to concentrate on the formation of surface features [9, 10].

Furthermore, JUICE's advanced payloads will enable broad new studies of Jupiter's atmosphere and magnetosphere, as well as their interactions with Galilean satellites, including gravitational and magnetic couplings. Eleven instruments are carried during the mission to monitor gravity, magnetic field, particle environment, among others [9, 10]. The particle and plasma objectives of JUICE will be the responsibility of PEP (Particle Environmental Package), a suite of six sensors that will provide in-situ measurements and imaging of plasma and particle environment.

1.1.1 Mission Profile

The JUICE spacecraft, launched on April 14th 2023, will reach Jupiter in 2031 after an interplanetary cruise of 7.6 years. JUICE will conduct four flybys as gravity assists during this period: one of the Earth-Moon system, one of Venus and two of Earth. After being placed in orbit around Jupiter, JUICE will carry out a 3.5 year tour of the Jovian system. It will perform 35 flybys of the icy moons Europa, Ganymede and Callisto and finally orbit Ganymede at different altitudes before being disposed in its surface [11]. Figure 1.1 illustrates the various mission events and their chronology.

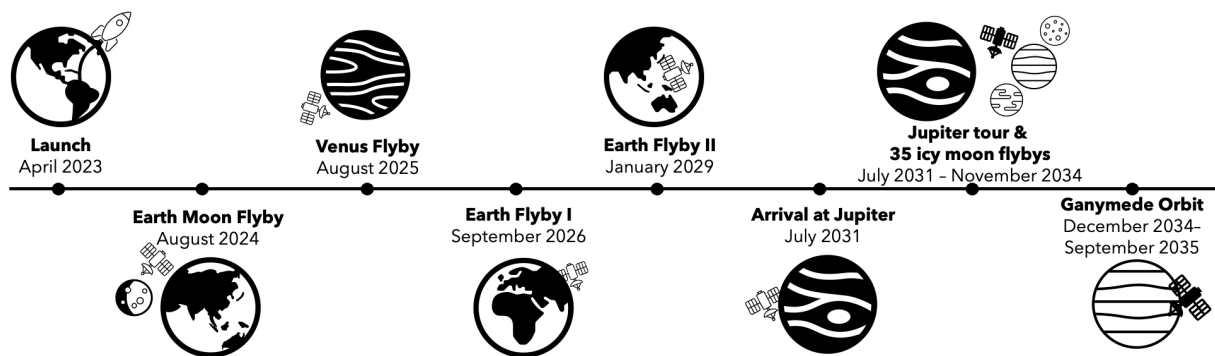


Figure 1.1: Chronograph of JUICE mission events. Adapted from [12].

1.1.2 RADEM on the JUICE mission

RADEM is on board the JUICE spacecraft as a housekeeping instrument. It will detect the high-energy electrons, protons and ions, sending alarm signals to the spacecraft if high radiation levels are reached. Although being considered a payload support instrument, RADEM will give additional and valuable information about the energetic particle population around Jupiter.

Up until now, only the Galileo mission's EPD has taken long term in-situ measurements of Jovian's radiation environment. The detector was a bi-directional telescope with a 4π sr field-of-view since it was mounted in a rotating platform and coupled with the satellite spin. EPD was capable of measuring protons with energies between 0.08-59 MeV, electrons with energies between 0.015-11 MeV and ions species up to Iron in different energy ranges. This instrument had a total mass of 10.5 kg and 6W available [6]. Because RADEM had strict mass constraints (initially of 1kg, altered to 5 kg further in the mission planning) and 1W power limit, the principles used in EPD cannot be used, particularly the rotational system.

RADEM is made up of four detectors: Electron Detector Head (EDH), Proton Detector Head (PDH), Heavy Ion Detector Head (HIDH) and Directionality Detector Head (DDH). The energy range of RADEM extends that of EPD, allowing the improvement of existing models and the better comprehension of the dynamics of the Jovian System. It is designed to measure electrons from 0.3 to 40 MeV, protons from 5 to 250 MeV and discriminate ions from Helium to Oxygen with energies from 8 to 670 MeV at the high particle fluxes of the Jovian System [8]. The DDH will measure electron angular distribution to compensate for the absence of a rotational platform.

Throughout the mission, RADEM will continuously monitor the radiation environment. During cruise, the scientific instruments will only be turned on for specific periods of time, either for calibration or scientific observation campaigns. Thus, RADEM will be essential in completing the set of scientific instruments, not just for the characterisation of Jupiter's harsh radiation environment but also during the cruise phase. Even though being a housekeeping instrument, RADEM will be able to conduct scientific investigations:

- Characterisation of Solar Energetic Particle (SEP) events: not only perform spectral measurements but also assess the particle's angular distribution
- Measurement of Galactic Cosmic Rays (GCR): provides an opportunity to study their modulation, particularly the correlation with solar events and solar activity variations
- Mapping the radiation environment between Venus and Jupiter: during JUICE's cruise phase the solar maximum will be reached (expected in 2025) and one solar cycle will be nearly completed, giving the opportunity of surveying associated risks for future missions
- Measurement of Jovian electrons in the Heliosphere: throughout the cruise phase, the main electron source is Jupiter. RADEM will perform spatial, spectral and angular analysis of these electrons.
- Characterisation of the Jovian radiation environment: obtain the energy spectrum and the angular distributions of trapped particles in Jupiter's magnetosphere and Ganymede, mapping the radiation belts and the influence of the Jovian moons
- Investigate trapped particles' angular distribution in reference to the local magnetic field, tightly correlated with their propagation, transport and dynamics in the Jovian System

1.2 Thesis Outline

The DDH, one of RADEM's detector heads, is the focus of this thesis, specifically its response characterisation and the analysis of its first flight data.

Chapters 2 and 3 introduce the main concepts and technical descriptions essential for the thesis development. Chapter 2 introduces the radiation environment to be encountered at the various stages of the JUICE mission. Besides providing information about the particle sources and their characteristics, it introduces state-of-the-art themes and research for which RADEM, and specifically the DDH, will provide valuable contributions over the mission operation. Chapter 3 provides a technical description of RADEM. It covers the signal processing and details RADEM's detector heads, with particular focus on the DDH. It additionally presents the flight-programmed configurations for the initial months of the cruise phase.

Chapter 4 is dedicated to characterising the DDH. It details the Geant4 simulations conducted to compute the DDH's response function for both of protons and electrons. A thorough examination of the protons' energy response functions is presented in addition to the analysis of the deposited energies by the generated protons. The assessment of the influence of thresholds on the response functions is also performed.

In Chapter 5 the analysis of the flight data is conducted. It is divided into two main sections: the analysis of DDH GCR data and the examination of a selected registered SEP event. The GCR data undergoes a detailed study of each DDH sensor, which is essential for subsequent analysis. Additionally, the Near Orbit Commission Phase is addressed, particularly the threshold scans performed on the GCR data. The second section focuses on the angular distribution of the selected SEP.

Chapter 6 presents the conclusions of this thesis and the future work for the DDH is discussed.

2 | Interplanetary and Jovian Radiation Environment

The three main contributors to the Jovian radiation environment are: charged particles released from the Sun, Solar Energetic Particle (SEP) events; high energy charged particles coming from outside the Solar System, the Galactic Cosmic Rays (GCR); and charged particles trapped in Jupiter's magnetosphere, Trapped Particles (TP). Each contributor has unique properties, particle populations, and particle energies, all of which will be discussed in this chapter.

2.1 Solar Particle Events

The solar activity is manifested by the constant release of charged particles and spurious bursts of electromagnetic radiation and charged particles, including Coronal Mass Ejections (CME) and Solar Flares (SF).

The Solar Wind is a continuous stream of electrons, ions, α -particles and a trace of heavier nuclei with energies of a few keV. It begins as a hot, dense, slow-moving plasma but, as it accelerates outwards, it cools, rarefies, and reaches supersonic speeds before meeting Mercury, in the range 300-1200 km/s. The Solar Wind will then interact with every planet differently, depending on the heliocentric distance, the planet's magnetosphere and local plasma sources. For example, the solar wind is the principal source of magnetospheric plasma on Earth and drives the magnetospheric dynamics. On Jupiter, it is widely accepted that these effects are internally generated instead [13].

CMEs and SFs are responsible for the release of Solar Energetic Particles (SEP), mainly protons with energies that can reach hundreds of MeV and, to a lesser extent, electrons and ions. These events have a high unpredictability and large variability in magnitude, duration and spectral characteristics and, therefore, have to be studied statistically.

SEP events occurrence is linked to solar activity, notwithstanding its stochastic nature. The average duration of the solar cycle is 11 years. The great majority of solar particle flux is supplied throughout a seven-year period known as solar maximum, however, SEP events can still occur during the remaining 4 solar minimum years. Daily measurements of the number of sunspots, linked to the solar activity, have been performed over the years. Results shown that both the duration and activity of each solar cycle varies. In Figure 2.1 the three previous solar cycles are presented along with the predicted measurements

for present one [14]. So far, data taken between 2020 and 2023 reveal that there are more sunspots than what was predicted for solar cycle 25.

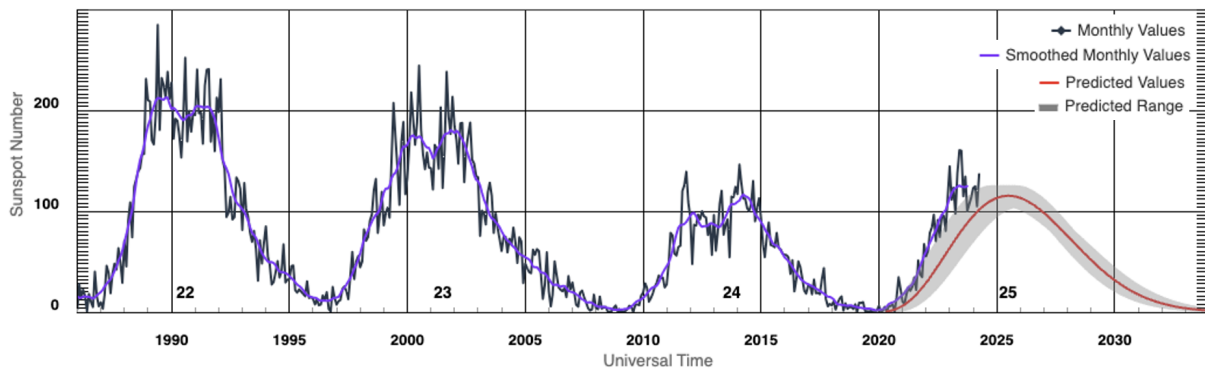


Figure 2.1: Solar cycle sunspot number progression. Adapted from [14].

The flux of a SEP event is known to diminish with distance from the Sun and, along with the shielding provided by Jupiter’s magnetosphere, the influence of SEPs in the Jovian System appears to be negligible [11]. However, these events are of major importance throughout the cruise phase, which will take place during a solar maximum, as can be seen in Figure 2.1. This will be a rare opportunity for measurements of the interplanetary radiation environment, not only from a monitoring perspective, but also from a scientific one. Additionally, the data collected can be compared and combined with information gathered from other missions currently exploring the interplanetary medium, such as BepiColombo [15], Solar Orbiter [16], and the Parker Solar Probe [17].

2.2 Galactic Cosmic Rays

Galactic Cosmic Rays originate from outside the Solar System and consist of protons (~90%) and ion species up to Uranium, although the majority of particles are iron or lighter. Figure 2.2 illustrates the fluxes of primary cosmic radiation for various nuclei as a function of their energy, as measured by several experiments. Despite GCR being an uniform, almost isotropic, low flux of particles, their energies can go up to 10^{21} eV which makes it impossible to shield spacecrafts. Events with such a high energy, on the other hand, have a very low probability. The GCR spectrum decreases with a power law distribution in energy and therefore these particles will not be dominant.

The GCR intensity, for energies below 1 GeV/nucleon, is anticorrelated with the solar cycle meaning that the flux will increase when the solar activity decreases. At solar maximum, nuclei with lower rigidity (momentum per unit of charge) can be attenuated by the solar wind as a consequence of the magnetic force exerted by the Heliosphere, deflecting the particles. GCR fluxes can vary more than one order of magnitude, especially at lower energies.

Moreover, the propagation of GCRs in the heliosphere is affected by additional factors, including solar wind velocity, the magnitude of the interplanetary magnetic field, and changes in solar polarity. Inherent physical mechanisms such as adiabatic cooling and diffusion in the interplanetary magnetic field lead to temporal and spatial fluctuations in their intensities [19]. Approximations and models have been in

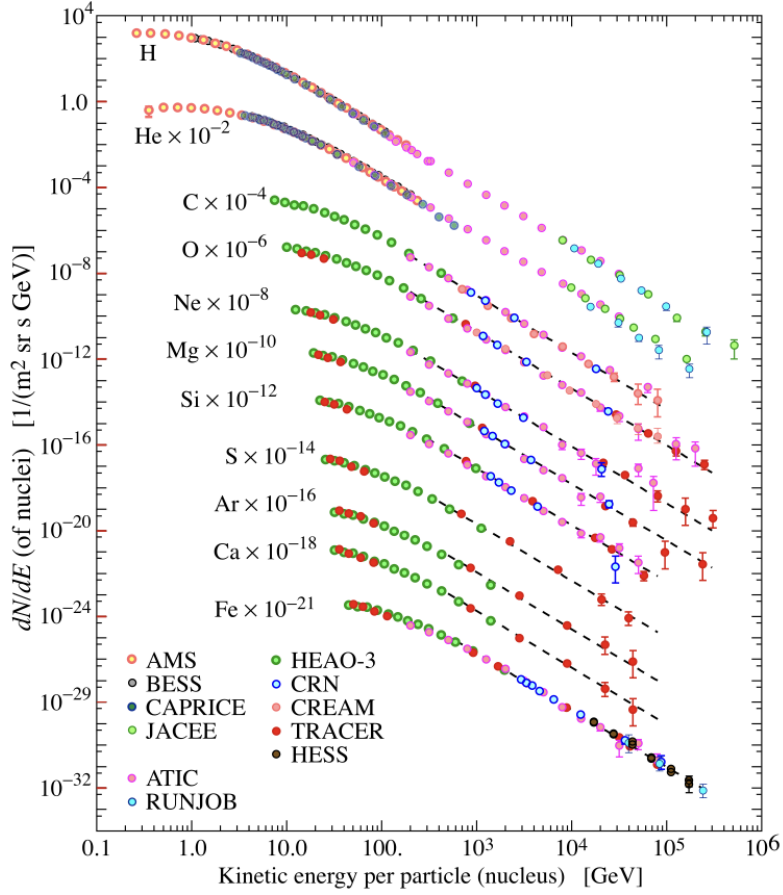


Figure 2.2: Primary cosmic radiation fluxes of nuclei plotted as particles per energy-per-nucleus vs energy-per-nucleus. From [18].

constant development to better describe GCR dynamics. These models can be directly compared and validated with experimental measurements of the radial intensity gradient. These quantity, G_R , is given by the ratio in Equation 2.1, where j_2 and j_1 are the GCR intensities at the heliocentric distances r_1 and r_2 , respectively.

$$G_R = \frac{\ln(j_2/j_1)}{r_2 - r_1} \quad (2.1)$$

The computation of this parameter requires simultaneous measurements of GCR fluxes at different heliocentric distances. Radiation monitors onboard various missions offer extensive datasets that can facilitate such measurements. Recent studies presented results from multi-point GCR measurements conducted by Standard Radiation Environment Monitor (SREM) instruments aboard ESA missions, spanning distances from 1 to 4.5 AU (Astronomic Units), over a complete solar cycle [19]. Additionally, the long and short-time variability of the GCR radial intensity gradient between 1 and 9.5 AU, which are not yet fully understood, were studied [20]. Direct relations with the polarity sign of the solar magnetic field, phase of the solar cycle and quasi-periodic variations of the solar magnetic field were found. Further investigations and follow up studies are essential to better understand GCR transport and dynamics.

As with SEP, GCR particles will not be the main feature of the Jovian environment [11] due to their low flux and the additional shielding provided by Jupiter's strong magnetosphere and planet/moons shadowing.

However, these particles remain important, mainly during cruise phase and Earth/Jupiter orbits, due to their high energies which allows them to cross a spacecraft and affect its electronic components and systems.

2.3 Jovian Magnetosphere

The intrinsic magnetic fields of planets, such as of Jupiter and Earth, carve a cavity out of the solar wind, the magnetosphere, affecting the local particle dynamics. The magnetic moment of Jupiter's magnetic field is 20 000 times larger than the Earth's and, as a result, Jupiter's magnetosphere can be up to 10 times stronger [1]. The Jovian magnetosphere can reach up to 7 million kilometres towards the Sun (day side) and almost to Saturn's orbit in the opposite direction (night side). For comparison, Earth's magnetosphere can only reach ~70 thousand kilometres on the day-side and ~400 hundred kilometres on the night-side.

A schematic comparison of the magnetospheres of Earth and Jupiter, components and shapes are presented in Figure 2.3. The boundary between the magnetosphere and solar wind plasmas is the magnetopause, where solar wind pressure matches the magnetic field. As the pressure exerted by the solar wind varies, this boundary will depend on solar activity. In front of the magnetopause lies the bow shock, a wake-like disturbance in the solar wind caused by its collision with the magnetosphere. The region between these two is called the magnetosheath. While the magnetosphere is compressed by the solar wind on the day-side, it is stretched into a long magnetotail in the night-side which consists of two lobes, separated by a plasma sheet of high particle density.

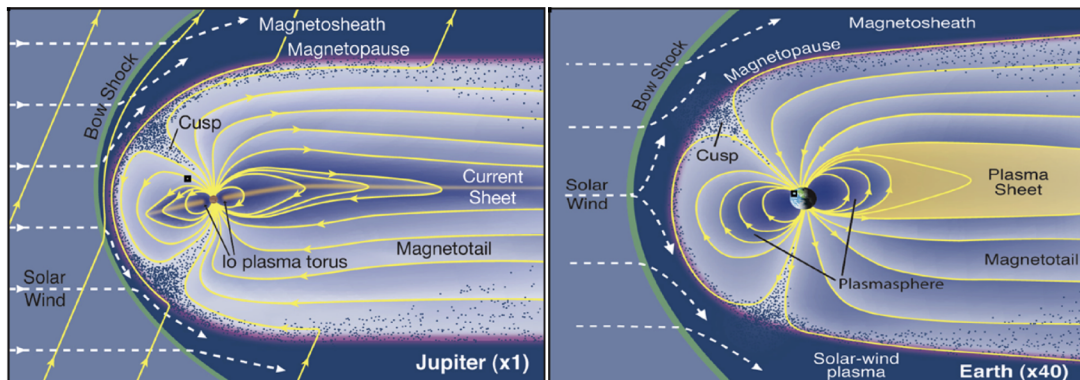


Figure 2.3: Schematic comparison of Jupiter's and Earth's magnetosphere [21].

The Jovian System is an example of a rotationally driven magnetosphere. The bulk of the energy is derived from Jupiter's rotation (rotation period of ~ 10 hours) and the plasma is mainly derived from local planetary sources. In this case by Io, a satellite of the planet [22]. On the other hand, Earth's magnetosphere dynamics are mainly driven by the solar wind.

2.3.1 Trapped Particles

The magnetospheres of planets, such as Earth and Jupiter, are able to contain trapped particles. The stronger the magnetic field, the more energetic particles can be trapped. The population of charged particles stably trapped by Earth's magnetic field consists mainly of protons with energies between 100 keV and several hundred MeV and electrons with energies between a few tens of keV and 10 MeV. Most of these particles are believed to come from the solar wind and others from the interactions of GCR with the Earth's atmosphere.

Unlike Earth, Jupiter's trapped particles are thought to come primarily from the volcanic emissions of Io with an estimated release of ~ 1 ton/s plasma mass. It consists mostly of charged states of S and O that populate a torus region near its orbit. The solar wind is the second most important source but has a considerably lower strength. At last, trapped particles can also be produced by the escape of ions (mainly H^+ and H^{+2}) from the ionosphere of Jupiter and the surface sputtering of the three icy satellites by Jovian plasma [22]. The confined particles in the Jovian magnetosphere are about 10 times more energetic and more abundant than those trapped on Earth, in which proton and electron energies can reach ~ 100 MeV and ~ 1 GeV respectively [23]. Figure 2.4 presents the integral electron fluxes of the trapped electrons in Earth Geosynchronous Orbit (GEO) and in Europa.

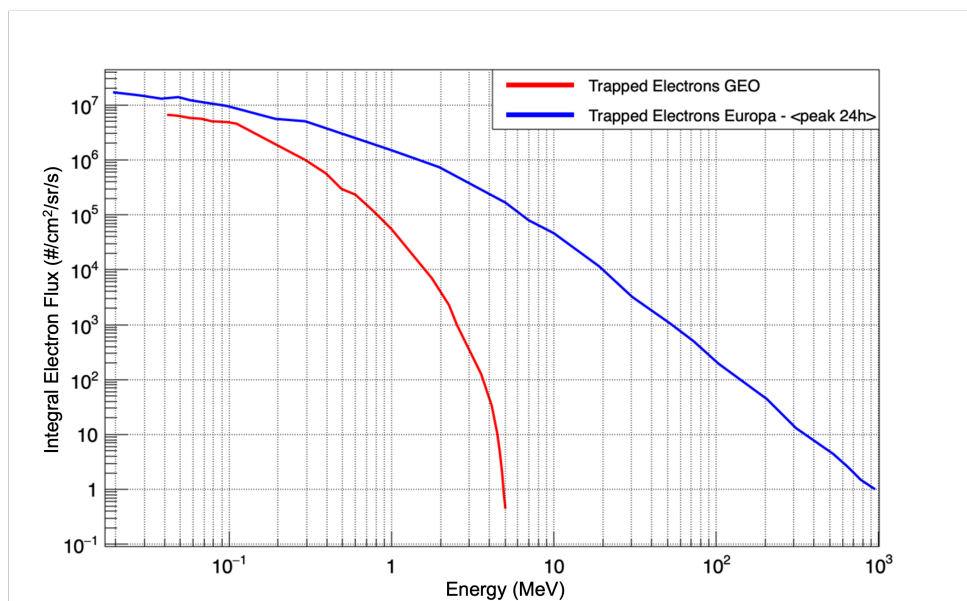


Figure 2.4: Comparison between the integral electron fluxes in Earth Geosynchronous Orbit and Europa <peak 24h> [24].

The Earth's energetic (above 10 MeV) trapped proton population is confined to altitudes below 20 000 km, as it can be seen in Figure 2.5 (left). The trapped electron population is divided into two distinguishable regions of high densities, the Van Allen belts: the inner belt populated by higher energy electrons and the outer belt mostly by electrons with lower energies, Figure 2.5 (right). The Earth's trapped particles will have a pivotal role at the start of the JUICE expedition during the three expected Earth flybys. The extensive knowledge and data from the Earth's radiation belts will offer diverse opportunities for calibrating RADEM and conducting cross-calibrations with other instruments.

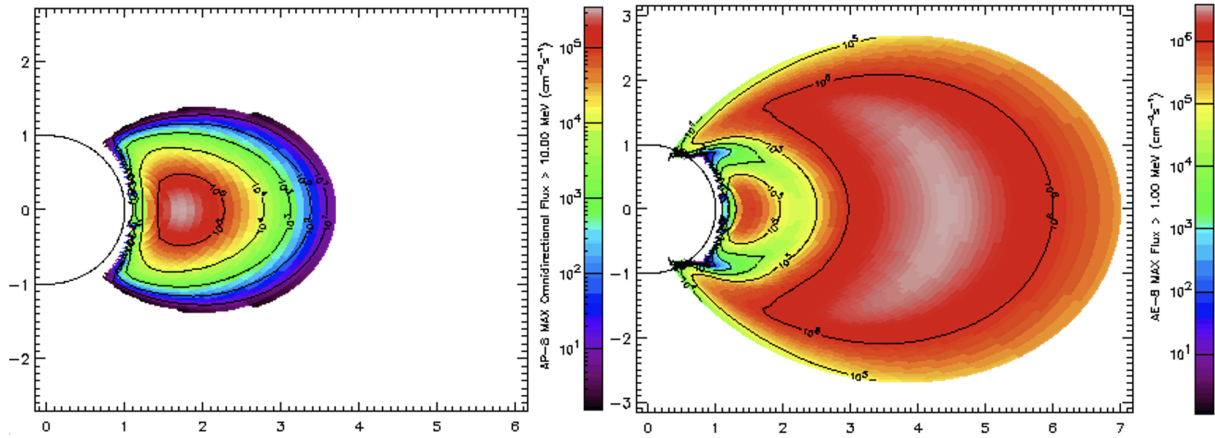


Figure 2.5: Earth's trapped proton environment (left) [25] and trapped electron environment (right) [26].

Similar radiation belts were found by the Galileo mission. The data acquired was used to develop the Jovian Specification Environment (JOSE) model [27]. Jovian's radiation belts surround Io and Europa (orbit radius of 5.99 and 9.39 R_J , $R_J=71492$ km), as well as numerous smaller moons. JUICE's perijove is at Europa which is the stage of the mission that has the harshest environment to be encountered. For this reason, JUICE will only conduct flybys but will not enter its orbit. Ganymede, on the other hand, is in an orbit where particle content fluctuates (orbit radius of 14.97 R_J). The interactions between its magnetic field combined with the Jovian field and the shielding provided by it, will modify the radiation environment around Ganymede and shield it from the Jovian radiation. Therefore, one of JUICES's objectives is to separate all magnetic contributions at the moon [9]. Callisto is the only moon outside the radiation belts but at the same time it is more exposed to GCR and SEP events (orbit radius of 26.33 R_J).

The expected proton and electron fluxes within the Jupiter magnetosphere were calculated by the JUICE Team for different phases of the mission [11]. The analysis used the JOSE model [27] and, specifically for the Ganymede orbit phases, the Ganymede Radiation Environment Engineering Tool (GREET) was additionally implemented. This tool accounts for the reduction of the radiation environment due to Ganymede's magnetic field. Figure 2.6 illustrates the integral fluxes for the different phases.

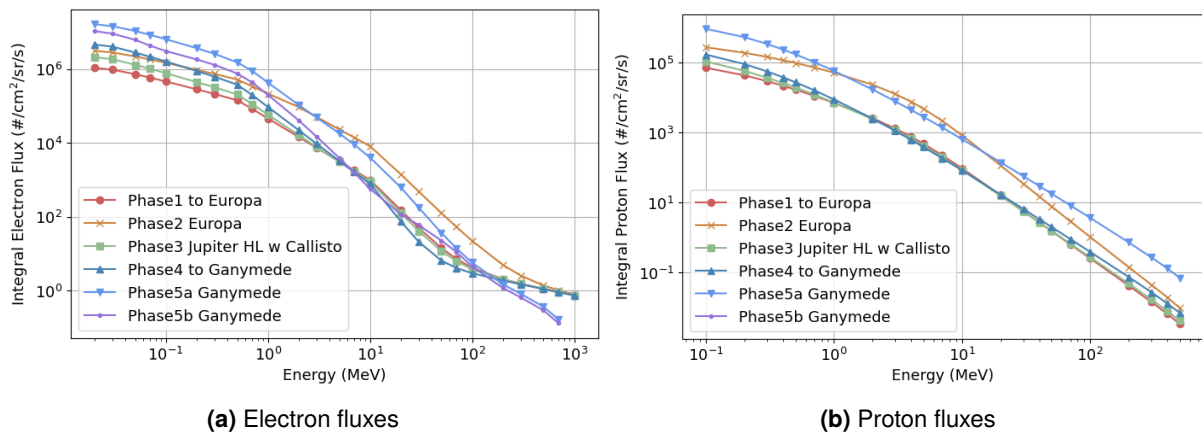


Figure 2.6: Expected proton and electron integral fluxes during different phases of the JUICE mission. [11]

The initial phase involves the JUICE transfer to Europa, followed by the Europa flybys. This phase presents one of the harshest radiation environments encountered during the mission. Phase 3 involves a Jupiter high latitude trajectory with Callisto flybys, followed by the JUICE transfer to its final orbit phase around Ganymede. The Ganymede phase, phase 5, is further divided into various sub-phases, each corresponding to a different orbiting altitude. Phase 5a involves Ganymede orbit insertion and a 5000 km circular orbit, while Phase 5b corresponds to a 500 km altitude circular orbit. The mission plan has undergone some slight alterations, and there may still be further changes in the future. However, the presented estimations provide a good indication of the expected fluxes to be encountered during the mission.

Besides providing information on the energy spectrum of Jupiter's trapped particles, the Galileo mission -specifically EPD- also revealed an angular dependence in the electron fluxes across Jupiter's magnetosphere [28]. The different angular distributions are directly correlated with the dynamics of Jupiter's energetic electrons and are of extreme importance to better understand their origins, acceleration and transport. Additionally, it has been shown that Ganymede has its own trapped particles, despite the shielding provided by its own magnetic field [29]. Figure 2.7 presents the angular distribution of two electron channels of EDP in two different locations during a Ganymede flyby. The maximum Local Pitch Angle (LPA), which is the angle formed between the electron's direction and the local magnetic field, is, in all cases, at 90° , indicative of a trapped flux. Moreover, a count rate increase near 180° is observed, suggesting the presence of an electron beam directed towards the moon's surface [29].

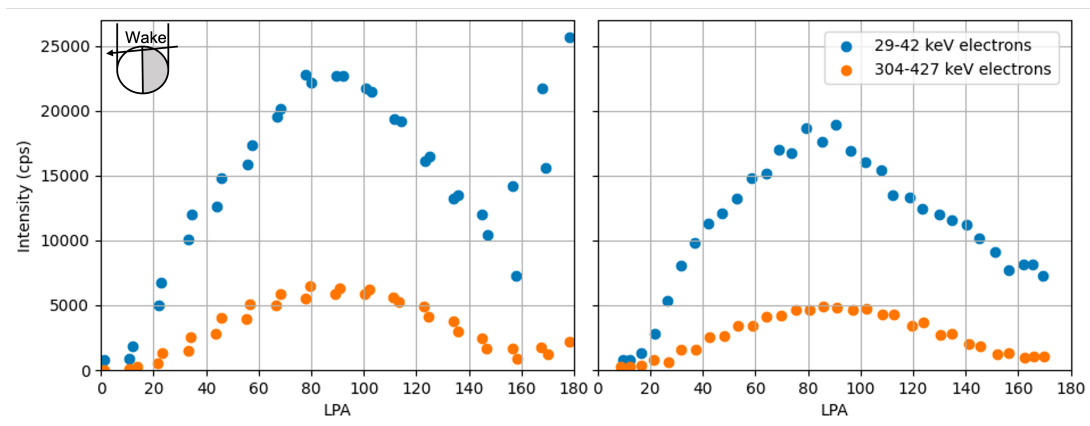


Figure 2.7: Electron Local Pitch Angle distributions of two electron channels of EDP in two different locals during a Galileo encounter with Ganymede (G29) at 28 December 2000. [29].

Jupiter has also been recognised as a dominant quasi-constant isotropic source of MeV electrons in the heliosphere since the 1970s [30]. Studies consistently demonstrated that these electrons mainly propagate along the nominal Parker Spiral. When Earth and Jupiter were located on the same Parker magnetic field line, an increase of MeV electron flux at Earth's orbit was observed [31].

These Jovian electrons are often used as test particles for modelling energetic particle transport. Recent observations by the Parker Solar Probe have detected Jovian electrons as close as 0.28 AU from the Sun, indicating their propagation without significant inhibition by the outward-moving solar wind [32]. Additionally, the importance of comparing multi-spacecraft data of these particles has been

highlighted to constrain influences on their transport process through the interplanetary medium [33]. With RADEM being operational throughout the cruise phase, it can make substantial contributions to these measurements. Moreover, Ulysses and Pioneer 10 detected the presence of Jovian electron jets, short-lived and highly anisotropic [34]. RADEM's inclusion of the DDH will therefore enable measurements of angular distributions and provide significant support to the studies on electron anisotropies. These extend to the observed anisotropies in Jovian jets as well as in Jupiter's trapped particles, as previously discussed.

3 | RADiation hard Electron Monitor

RADEM is composed of four detectors, the Proton Detector Head (PDH), the Electron Detector Head (EDH), the Heavy Ion Detector Head (HIDH) and the Directionality Detector Head (DDH). Each detector is designed to operate in the high particle fluxes of the Jovian System, 2×10^9 electrons/cm²/s and 2×10^8 protons/cm²/s and measure the energy of each particle species on the ranges shown in Table 3.1 [8]. Figure 3.1 shows the most recent version of RADEM's STEP geometry, with beige representing the Aluminum housing, grey representing Tantalum shielding, and brown representing the four detector heads.

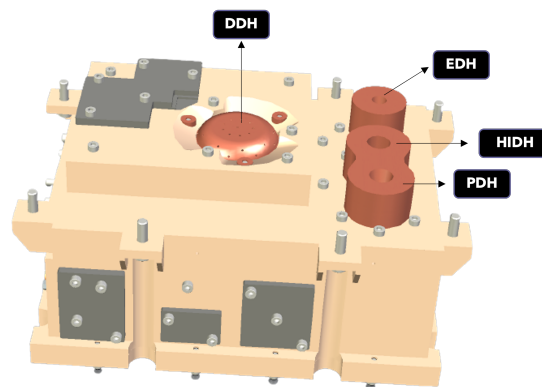


Figure 3.1: RADEM STEP geometry.

Table 3.1: Energy ranges of detection of RADEM for protons, electrons and heavy ions.

Protons (MeV)	Electrons (MeV)	Heavy Ions (MeV)
5 – 250	0.3 – 40	He - O from 8 – 670

3.1 Working Principle

RADEM consists of two types of detectors: three stack detectors, PDH, EDH and HIDH, and one specifically designed for directionality measurements, the DDH. Stack detector construction relies on the profile of the interaction a charged particle has as it crosses the different materials that compose it - absorbers and sensors - to infer the particle's energy. The DDH's design incorporates a new and personalised geometry, as will be explored in detail, but studying the interactions of a charged particle with the detector's materials is also fundamental.

3.1.1 Interaction of particles with matter

As a charged particle travels through a material, it interacts with both the atomic nuclei and electrons, dissipating energy. Ionisation and excitation of the medium's atoms are the primary causes of this loss. The average rate of energy loss per unit of distance of heavy particles in a given medium, also known as the stopping power of a material, can be described by the Bethe-Bloch's formula:

$$-\frac{1}{\rho} \frac{dE}{dx} = K \frac{Z}{A} \frac{z^2}{\beta^2} \left[\ln \left(\frac{2m_e c^2 \beta^2 \gamma^2 T_{max}}{I^2} \right) - 2\beta^2 - \delta - 2 \frac{C_e}{Z} + F \right] \quad (3.1)$$

$$\text{with } K = 2\pi N_a r_e^2 m_e^2 c^2 \quad (3.2)$$

where ρ is the material density, N_a the Avogadro's number, r_e the classical electron radius, m_e the electron rest mass, Z the material's atomic number, z the incoming particle's charge, A the material's mass number, T_{max} the maximum transferred energy in a single collision, I the mean excitation of the material, δ the density correction necessary for higher energies, C_e the shell correction function and F represents the corrections of higher order. β is given by $\beta = 1 - 1/\gamma^2$ and γ by $\gamma = E/mc^2$.

Due to electrons having the same mass as the atomic electrons within the medium and lower than the mass of the medium's nucleus, they will experience different energy losses per collision compared to heavier charged particles. Furthermore, electrons will also lose energy due to radiative processes. Electromagnetic radiation, or Bremsstrahlung, is produced as a result of an electron being accelerated by an atom's electrostatic field within the medium. Altogether, the behaviour of the material's stopping power for electrons will consequently differ from that of heavier charged particles at the same energies. This disparity is evident in Figure 3.2, where the electron, protons and α particles (helium nuclei) stopping power on Silicon is represented. In the range of detection, the proton and α particles stopping power decreases as energy increases while the contrary is true for electrons.

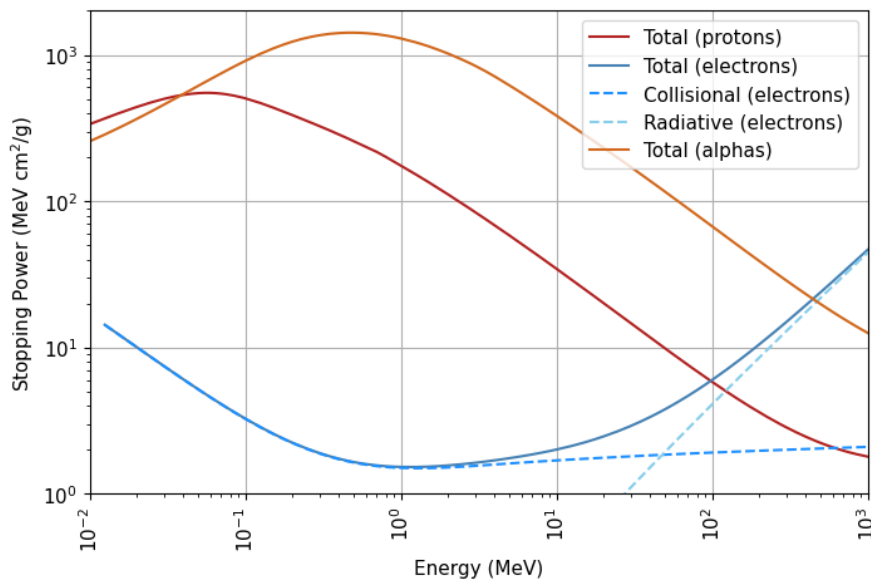


Figure 3.2: Proton and α particle stopping power in Silicon and electron total, radiative and collisional stopping power in Silicon [35, 36, 37].

3.1.2 Silicon Detectors

To detect the passage of particles, Silicon diodes are utilised. Silicon is a semiconductor, characterised by having an electric conductivity between that of an insulator and that of most metals.

When a large number of atoms are arranged to form a crystal, the discrete energy levels of the atom's electrons overlap, creating energy bands. The occupied band with higher energy is known as the valence band and the subsequent as the conduction band. Unlike metals, whose valence and conduction bands are overlapped, semiconductors and insulators have an energy gap that separates them. For semiconductors, this gap is of about 1 eV, while for insulators it exceeds 3 eV. Specifically for silicon, its band gap is approximately 1.12 eV. Silicon's electrical conductivity can be enhanced with the addition of impurities, decreasing its band gap width. If the impurity has a greater number of valence electrons than Silicon (donor), the excess electrons are donated to the conduction band, leading to the formation of a n-type semiconductor. On the other hand, if the impurity has fewer valence electrons (acceptor), a positively charged hole is formed in the valence band. The Silicon becomes a p-type semiconductor. Electrons and holes are the majority charge carriers in n-type and p-type semiconductors, respectively.

When these two semiconductor types are combined, a PN junction is formed. This junction triggers the diffusion of electrons from the n-type layer to the p-type layer and holes in the opposite direction. Simultaneously, as diffusion occurs, an electric potential is created. This potential acts in opposition to the diffusion and increases until the equilibrium is reached, resulting in the establishment of a depletion region. When a negative potential is applied to the p-type layer in respect to the n-type layer, the depletion region is increased until the junction is fully depleted. RADEM silicon sensors operate within this regime with a potential of 90V.

As charged particles crosses a silicon sensor, they interact with the depletion region creating a electron-hole pair. This production takes place when the incoming particles transfers enough energy to excite an electron from the valence band to the conduction band (on average 3.6 eV for Silicon). The quantity of electron-hole pairs produced is therefore proportional to the deposited energy by the incoming particle. The electric field within the depletion region quickly separates the created pair, directing the electrons to the cathode and the holes to the anode. This process results in an electric signal which is subsequently interpreted.

In Figure 3.2 it is apparent that protons with energy below 100 MeV exhibit greater energy loss than electrons while crossing Silicon. Therefore, a greater number of electron-hole pairs will be produced and distinguishing the signal between both particle types can be done by implementing energy cuts in the front-end electronics. Nonetheless, protons with energies exceeding 100 MeV deposit comparable energies to electrons in the relevant energy ranges for detection, resulting in contamination. Based on the particle's stopping power in the materials it passes through and calibration measurements, the energy is estimated from the deepest Silicon detector it reaches in the stack detector. The deeper the particle goes in the stack, the more energetic it is.

3.1.3 Front-End Eletronics

A custom-made ASIC VATA466 was developed by IDEAS [38] for the readout of the charge signals produced by particles interacting with the RADEM's silicon radiation sensors [39]. In total, the ASIC has 32 High-Gain (HG) channels and 4 Low-Gain (LG) channels, each of which may be coupled to a different sensor. The HG channels have two charge discriminators - Low and High Thresholds (LT and HT) - programmable from 2.2 fC to 0.1 pC and from 15 fC to 1 pC, respectively. The LG channels only have one charge discriminator, the LT, programmable from 260 fC to 22.6 pC. The level triggers feed 36 coincidence pattern units and 36 digital counters (one for each pattern unit). It is possible to program individually each coincidence unit for triggering on a specific pattern, masking the 64 HG channels and 4 LG channels thresholds. A special case is using the two thresholds in high-gain channels, which increments a counter when the pulse height is in between the two thresholds [39].

The thresholds of the ASIC channels are programmable in Digital-to-Analogue Converter (DAC) units. IDEAS conducted the calibration from DAC units to units of charge, with the indicative results detailed in Table 3.2. This table includes the measured values for the minimum threshold above noise and maximum threshold, along with the step size, which serves as the conversion factor between DAC and fC. In the absence of a calibration factor from DAC units to MeV, which better relates the flight data with the simulations and theoretical models in comparison, a direct conversion from fC to MeV will be employed. This conversion is derived from first principles, dividing the average energy required to create an electron-hole pair in Silicon by the electron charge. Consequently, the relation $1 \text{ fC} \approx 22.5 \text{ keV}$ is established.

Table 3.2: Minimum threshold above noise, maximum threshold, and step size for the three types of thresholds.

	Minimum Threshold above Noise (fC)	Maximum Threshold (fC)	Step Size (fC)
LG Threshold	260	22800	28
HG Low Threshold	2.2	109	0.1
HG High Threshold	15	1020	1.0

The ASIC also has an internal calibration system that allows to connect each channel to an adjustable pulser generator. In spite of not replacing the actual particle calibration, it can be used to perform functional analysis and adjust to any parametric changes during the mission.

3.2 Detectors

3.2.1 Proton and Electron Detector Heads

The Electron and Proton Detector Heads/Stacks include eight Silicon diodes, which are numbered in Figure 3.3. In order to provide quasi-logarithmic energy channels, several absorbers are used with different materials and thicknesses. Both detectors are surrounded by a copper collimator of 8 mm with an

aperture of 20° and 15° for the PDH and EDH, respectively. Tables 3.3 and 3.4 systematise the materials and dimensions of both sensors and absorbers of the PDH and EDH, respectively.

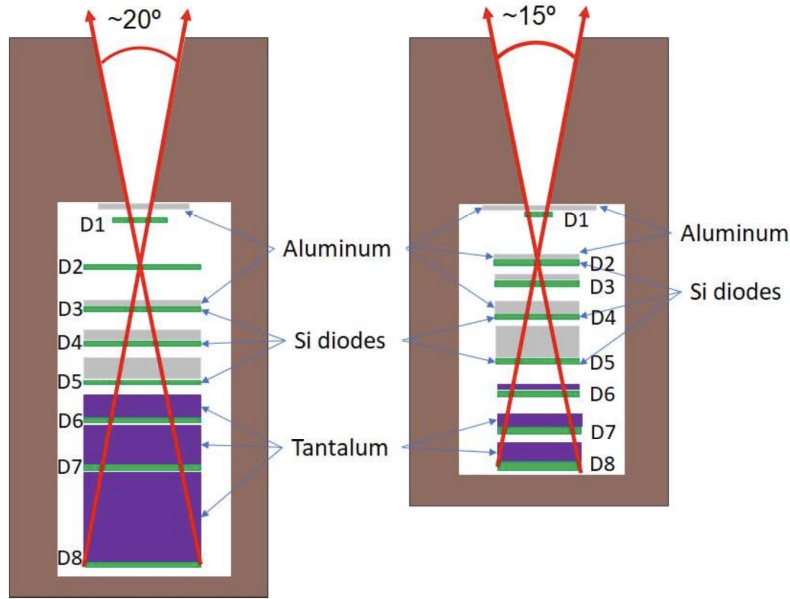


Figure 3.3: Schematic of PDH (left), EDH (right) [24].

Table 3.3: Material, dimensions and theoretical proton and electron energy cutoff of absorbers and sensors of PDH. Numbering follows Figure 3.3, from top to bottom.

Stack element	Material	Diameter (mm)	Thickness (mm)	Cutoff energy (MeV)	
				Proton	Electron
Absorber 1	Al	13	0.2	4	0.15
D1	Si	6	0.32	7	0.3
D2	Si	12	0.32	9.5	0.45
Absorber 2	Al	14	0.4	12.5	0.6
D3	Si	12	0.32	15	0.7
Absorber 3	Al	12	1.2	20	1.25
D4	Si	12	0.32	25	1.5
Absorber 4	Al	12	3.3	35	3
D5	Si	12	0.32	35	3
Absorber 5	Ta	12	2	50	10
D6	Si	12	0.32	50	10
Absorber 6	Ta	12	4.8	80	>1000
D7	Si	12	0.32	80	>1000
Absorber 7	Ta	12	10.8	125	>1000
D8	Si	12	0.32	125	>1000

The EDH has one ASIC chip uniquely assigned to it. Each sensor diode of the EDH is connected to a HG channel. The PDH shares a chip with the HIDH, the PDH sensors connected to the HG channels and the HIDH diodes connected to the LG channels.

To establish if the particle entered by the field-of-view (FOV) of the detector, a coincidence can be imposed between the top diode, D1, and the others. If the condition is not verified, the signal is vetoed since it could not have come from the detector's aperture.

Table 3.4: Material, dimensions and theoretical proton and electron energy cutoff of absorbers and sensors of EDH. Numbering follows Figure 3.3, from top to bottom.

Stack element	Material	Diameter (mm)	Thickness (mm)	Cutoff energy (MeV)	
				Proton	Electron
Absorber 1	Al	14.5	0.4	6	0.35
D1	Si	3	0.32	9	0.4
Absorber 2	Al	8	0.3	12.5	0.5
D2	Si	6	0.32	15	0.7
Absorber 3	Al	6	0.9	17.5	1
D3	Si	6	0.32	20	1.25
Absorber 4	Al	6	1.9	25	2
D4	Si	6	0.32	27.5	2
Absorber 5	Al	6	3.8	40	4
D5	Si	6	0.32	40	4
Absorber 6	Ta	6	1.2	50	7
D6	Si	6	0.32	50	7
Absorber 7	Ta	6	1.7	65	17.5
D7	Si	6	0.32	65	17.5
Absorber 8	Ta	6	2.1	80	35
D8	Si	6	0.32	80	35

3.2.2 Heavy Ion Detector Head

The HIDH is composed of two Silicon sensors and one Aluminum absorber at the top of the detector, shown in Figure 3.4. As previously indicated, HIDH and PDH will share an ASIC chip. HIDH's two sensors are connected to the ASIC's two LG channels. This detector will be able to differentiate ions from Helium to Oxygen with energies between a few MeV to ~600 MeV through the measurement of the ion's Linear Energy Transfer (LET).

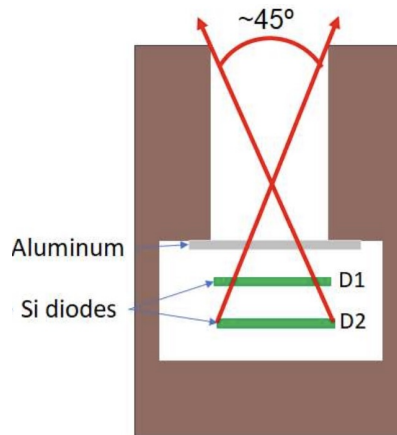


Figure 3.4: Schematic of HIDH [24].

Table 3.5: Material and dimensions of absorbers and sensors of HIDH. Numbering follows Figure 3.4, from top to bottom.

Stack element	Material	Diameter (mm)	Thickness (mm)
Absorber 1	Al	17	0.1
D1	Si	12	0.32
D2	Si	12	0.32

3.2.3 Directionality Detector Head

Due to its mass and power constraints, RADEM could not have the same design as Galileo's EPD, particularly the rotating platform. This was the driving force for the development of the DDH, a directional detector to perform flux angular measurements. The DDH is composed of a toroidal copper collimator with 28 apertures, each with 1 mm diameter and a depth of 8 mm (aperture of $\sim 7.2^\circ$). Figure 3.5 (left) represents a cut view of the DDH concept. The holes point to four zenith directions, 0° , 22.5° , 45° and 67.5° , each having 9 different azimuthal directions spaced by 40° , excluding 0° . The sensors that correspond to the 67.5° direction are phased by 20° from the 22.5° and 45° directions due to the space constraints of the sensor plane, as schematised in Figure 3.5 (right).

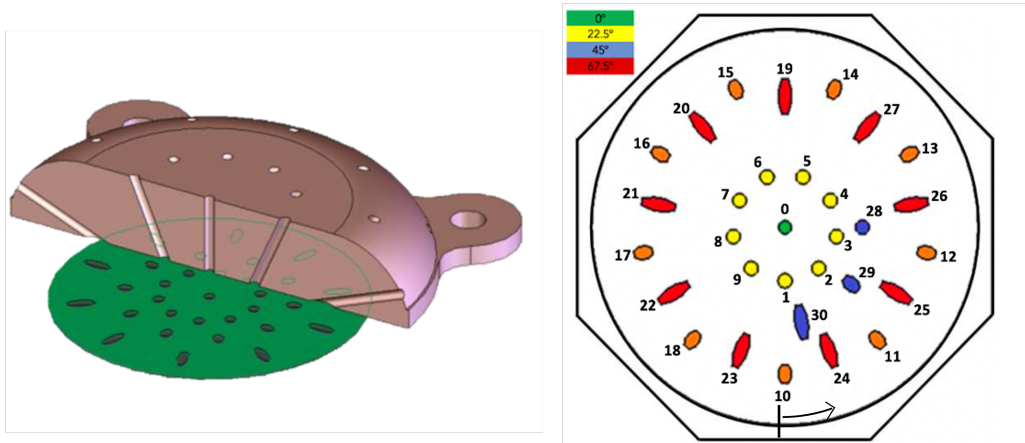


Figure 3.5: Cut view of the DDH (left) [24] and DDH sensor on-flight top-view serialization (right) [40]. The color code corresponds to the different zenith direction: green - 0° ; yellow - 22.5° ; orange - 45° ; red - 67.5° ; blue - background sensors.

The signal sensors placed below the collimator apertures have different areas for different zenith directions, matching the aperture projections on the sensor plane. Steeper angles lead to a larger sensor area as summarised in Table 3.6. Background counting is done with three extra blind sensors located outside the collimator apertures (blue sensors in Figure 3.5 (right)). Each background sensor will have a different area, corresponding to the three possible projection areas. Every pixel (signal or blind sensor) is isolated and connected to a single HG channel of an ASIC chip uniquely dedicated to the DDH.

Table 3.6: Material, dimensions and theoretical proton and electron energy cutoff of absorbers and sensors of DDH.

	Zenith Angle ($^\circ$)	Material	Thickness (mm)	Surface Area (mm 2)	Side Area (mm 2)	Cutoff energy (MeV)	
						Proton	Electron
Absorber	-	Kapton	0.505	-	-	7	0.3
Sensors	0	Si	0.3	0.79	0.94	7	0.3
	22.5	Si	0.3	0.91	1.02	7	0.3
	45	Si	0.3	1.11	1.23	8.5	0.35
	67.5	Si	0.3	2.07	1.91	12.5	0.5

A Kapton absorber with a thickness of $505 \mu\text{m}$ sits between the copper collimator and the sensor plane. It will stop electrons and protons with energies below $\sim 300 \text{ keV}$ and $\sim 7 \text{ MeV}$, respectively. This

value varies slightly for different directions since the linear path length of incoming particles coming from steeper angles will be greater.

3.3 Flight Configuration

Throughout the JUICE mission, RADEM will have the possibility to adapt its detection configurations based on the radiation environment to be encountered. During the cruise phase, GCR and SEP events will be predominant. However, upon reaching Jupiter’s magnetosphere, the energetic electron population will dominate over any other particle type. Thus, it is crucial to determine the best parameters to effectively characterise each environment.

During the initial stage of the cruise phase, the detector stacks, EDH, PDH and HIDH, will operate in non-coincidence mode. This means that each sensor has an independent response, extending its coverage beyond the FOV of each stack. This feature will be particularly relevant in GCR detection due to their highly energetic spectrum, capable of penetrating through the shielding. Nonetheless, obtaining an energy spectrum of the incident particles, which is essential to characterise SEP events and cross-calibrate the DDH, may not be possible.

The thresholds applied to each sensor are used to differentiate between particles, as mentioned in Section 3.1.2, have a large impact in the detectors’ response. Since the DDH will be the focus of this thesis work, Table 3.7 presents the LT and HT of all the DDH sensor channels which are programmed to trigger when the pulse height is in between the given values. As mentioned, to convert from fC to MeV, first principles are used: $1 \text{ fC} \approx 22.5 \text{ keV}$.

Table 3.7: Thresholds of the DDH for the initial stage of the cruise phase.

LT (DAC)	LT (fC)	HT (DAC)	HT (fC)
90	9	345	345

Another adjustable parameter is the time interval during which depositions that fulfil the ASIC’s channel programming are counted. Increasing this time interval will lead to higher statistics but to lower spatial resolution. For the cruise phase the time step is set to one minute.

4 | DDH Response Functions

In order to fully characterise RADEM's behaviour and interpret its data it is crucial to understand how energetic particles interact with it. The space radiation environment, consisting of different types of particles with energies that span multiple orders of magnitude, cannot be replicated on Earth. Furthermore, the interactions between charged particles and the detector are not deterministic, the physical processes involved rather have a stochastic nature. Therefore computational simulations are necessary to describe them. By simulating a sufficient finite number of particles, the outcome of consecutive probabilistic events can be computed and a reliable statistical description of the interactions obtained.

4.1 Geant4 Simulation

Geant4 (GEometry ANd Tracking) is a toolkit that uses a combination of the composition and rejection Monte Carlo methods to simulate the passage of particles through matter [41]. The toolkit is used in diverse areas of science, from High Energy and Nuclear Physics to medical and space applications, undergoing continuous development.

Geant4 enables the creation of a custom application which simulates any geometric configuration and records the chosen output of physical quantities. The geometry model in Geant4 allows a flexible and hierarchical structure for describing an experimental setup, creating volumes to represent different components. A set of simple solids are available which can be described by a minimal set of parameters [42].

Once the dedicated Geant4 application is built, a set of primary particles with diverse characteristics, such as source type and geometry, energy, and distributions in both energy and angle, can be generated. These particles are then tracked as they interact with the computational model of RADEM. The interactions are calculated step-by-step until either all of the particle's energy is deposited or a certain threshold is reached, using various physics models. These models compute the probability of diverse processes, including electromagnetic and hadronic interactions, between the particle and the medium. Users can compile these models into physics lists or use pre-built ones, optimised for specific applications [41].

To obtain the desired output, one of which being the deposited energy on RADEM's sensors, the corresponding volumes are aggregated into sensitive volumes. When a particle interacts with one of them, a snapshot of the physical interaction is taken (hit) and the desired information stored for further analysis. Additionally, Geant4 enables the visualization of geometry, trajectories and hits [42].

4.1.1 RADEM model

The incorporation of both the spacecraft and RADEM geometries into Geant4 is essential to perform an accurate simulation. Given RADEM's complexity and its numerous components, the implementation of geometrical models from CAD (Computer Aided Design) systems is required. To accomplish this, a STEP (Standard for The Exchange of Product Data) file detailing RADEM's geometry (see Figure 3.1) was converted by GUIMesh [43] into a GDML (Geometry Description Markup Language) file. This file is readable by Geant4 and contains the detector's volumes, materials and hierarchy.

Replicating the same level of detail for the spacecraft, whose complexity and size is illustrated in Figure 4.1, presents a significant challenge in terms of simulation time and computational resources. As a compromise between accuracy and time, the spacecraft was converted to a 6-side box of Aluminium and included in the RADEM model [24]. The thickness of each face is given in Table 4.1 according to the axis defined in Figure 4.1.

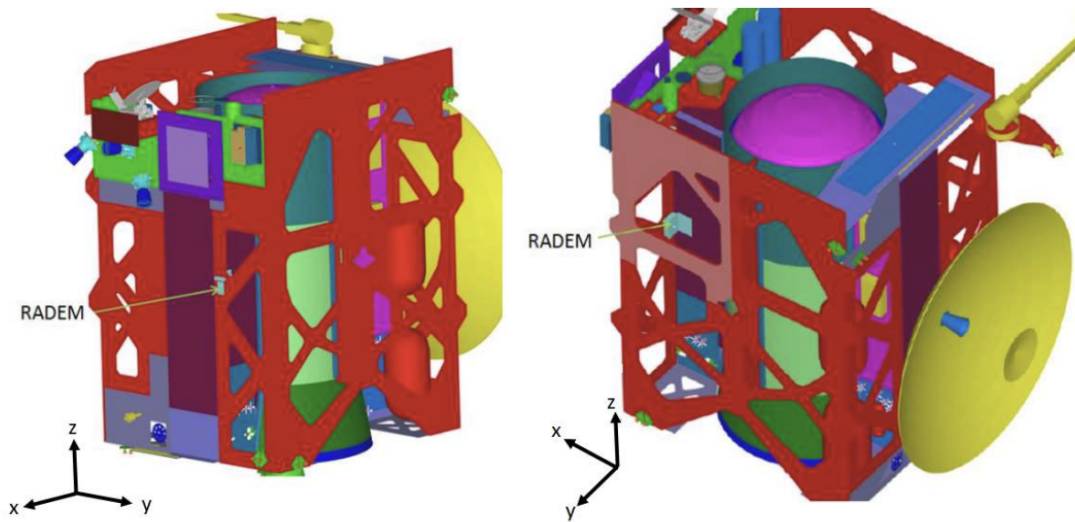


Figure 4.1: Views of the JUICE spacecraft model and RADEM's placement.

Table 4.1: Thickness of the 6-side Aluminum box as the equivalent shielding of JUICE spacecraft at RADEM's faces.

Face	-X	X	-Y	Y	-Z	Z
Al thickness (mm)	1	0.5	10	0	0.5	0

4.2 Response Functions

Following the integration of RADEM's model in Geant4, the particle generation was initiated in order to obtain both electron and proton responses of the DDH. A set of Geant4 simulations were performed in vacuum, generating both types of particles separately. For this, a planar source with a parallelepiped form (six squared faces of 200x200 mm² area) was used, enveloping the entire volume of RADEM. An isotropic angular distribution of both generated electrons and protons was considered. However, while

the protons' energy followed an inverse power law distribution, the electrons' energy followed a flat one. Alongside the used energy distributions, the simulation was divided in several energy intervals to enhance computation efficiency. Lower-energy particles require a larger number of generated particles to achieve a statistically significant response compared to higher energies. Table 4.2 provides the number of protons and electrons generated in each energy interval.

Table 4.2: Energy interval and correspondent number of generated protons and electrons.

Particle	Energy interval (MeV)	Generated particles
Proton	0.1-10	2×10^{10}
	10-100	1.8×10^{10}
	100-300	4×10^8
	300-1000	3.5×10^8
	1000-3000	2.8×10^8
	3000-10000	1.6×10^8
Electron	0.1-0.5	4×10^{10}
	0.5-1	5×10^{10}
	1-2	3×10^{10}
	2-10	4.5×10^{10}
	10-100	2×10^9
	100-400	3×10^9

Each simulation run produces a ROOT [44] file as an output, storing chosen variables within a ROOT tree, essential for the subsequent analysis. All the relevant information was agglomerated in several histograms, ranging from the different conditions under which the particle was generated to the depositions it made in the sensitive volumes.

The response function of a detector quantifies its sensitivity to an incoming particle. It allows a detailed study of each of the particle's properties if relevant for the detector characterisation. For the DDH, two properties are important to consider: the primary energy and the primary angle of emission of each particle. However, in this work, only the primary energy will be thoroughly studied as it has the most significant impact on the analysis to be performed.

A detector's energy response function can be expressed in terms of the channel's geometric factor as a function of the initial energy of the incident particles. This quantity is calculated according to equation 4.1, which considers a hemispherical isotropic angular distribution around the surface normal. It computes the fraction of particles with the same primary energy (E) which deposit enough energy in a given sensor (N_{sensor}) to the total simulated in a surface area A ($N_{incident}$).

$$F_R(E) = A \frac{N_{sensor}(E)}{N_{incident}(E)} \int_0^{2\pi} d\phi \int_0^{\pi/2} \sin\theta \cos\theta d\theta = A\pi \frac{N_{sensor}(E)}{N_{incident}(E)} \quad (4.1)$$

Although the simulation was performed for both protons and electrons, the following analysis of the response functions will focus solely on protons. This is because the available flight data primarily consists of events composed of these particles, such as GCR and SEP. Electrons will be important for future work, as will be discussed at the end of this thesis.

4.2.1 Proton Response Functions

The characterisation of the DDH for protons is a crucial step to understand the data from GCRs and SEPs. Protons will be vital for calibrating each DDH sensor with GCR flight data, especially considering that they are the main constituents of GCRs. Accordingly, simulations were focused on obtaining sufficient statistics to ensure a stable response when applying the theoretical models of GCR. Moreover, the proton characterisation will be centered in the sensor's energy response function. The primary energy of the incident proton directly affects the deposition made in each sensor and consequently the counts registered by it, which is the output obtained from the flight data. The direction of the incident particle will not play a significant role for the GCR analysis as will be discussed.

Deposited Energy vs Incident Energy

The mean deposited energy in a selected sensor, as a function of the proton's primary energy is presented in Figure 4.2.

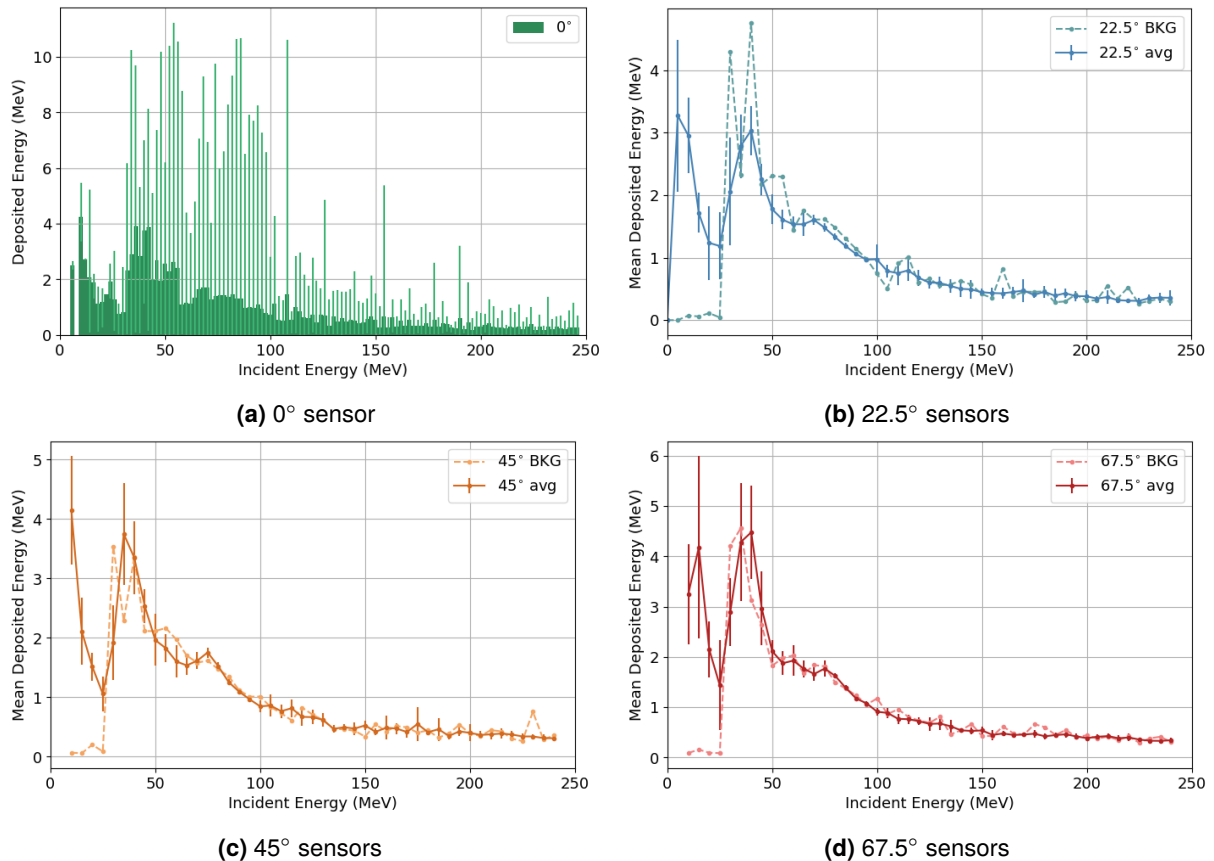


Figure 4.2: Mean deposited energy as a function of proton's incident energy for sensors with same zenith direction.

Figure 4.2a displays this relation for the central sensor with a zenith direction of 0° . The bars represent the mean deposited energy in the respective incident energy bin, with error bars indicating the minimum and maximum values of the deposited energies. This representation was selected to illustrate the dispersion of the deposited energy values for each incident energy which is present in all sensors. It is worth noting

that the dispersion is directly correlated with the statistics available in each bin but still provides a clear demonstration of the spread of deposited energies. Due to the large number of sensors, Figures 4.2b, 4.2c and 4.2d, group the sensors by zenith direction (averaging across the sensors with same zenith angle) and similarly present the mean deposited energy as a function of the protons' incident energy. This procedure was chosen due to the expectation of negligible azimuth variation, given the isotropic angular distribution of the simulated protons. Nonetheless, the mean deposited energies of all sensors are presented in Section A of Appendix A. Notably, the background sensors were excluded from the averaging process due to their distinct behaviour at lower energies, as will be further discussed.

Figure 4.2 shows that for incident energies below 30 MeV, all curves, except for those of background sensors, exhibit the same behaviour. In this energy interval, sensors aligned with an aperture present a decreasing mean energy deposition. For these energies, only protons that are aligned with the sensor's aperture will be able to reach the Silicon sensors, provided they can cross the Kapton layer above. According to Table 3.6, the theoretical energy value from which protons are able to cross the Kapton layer is between 7 MeV and 13 MeV, agreeable with the gap in the initial incident energies. Above these values and as the incident energy increases, the decrease in energy depositions is verified, also in concordance with what was expected from proton's stopping power discussed in Section 3.1.1. It is important to note that initially, the deposited energy should increase with incident energy, as long as the protons stop in the Silicon sensors, collecting all the protons' energy. However, this trend is not as evident in the figures due to the binning used. Once the protons start traversing the sensor, the decreasing behaviour begins. On the other hand, the background sensors register a constant value of very low energy depositions. To reach the background sensors, protons must not only cross the Kapton layer but also the copper collimator, which has a depth of 8 mm. Hence, almost no depositions will be observed in this energy range for the background sensors.

For energies above 30 MeV, all sensors behave the same. Above this energy protons begin to cross the copper collimator, losing energy in the process. Consequently, those reaching the sensor will have significantly lower energies than initially, resulting in higher energy depositions. However, similarly to what occurs to protons with energies below 30 MeV, as their incident energy increases, the mean deposited energy to decreases. In this case it is possible to observe an initial increase in energy deposition as protons stop in the sensor. The energy deposition peaks, and the decreasing trend begins as protons completely cross the Silicon sensor.

Response Functions

The previous analysis is useful to better understand the computed response functions. Figure 4.3 presents the geometric factor for each zenith direction, computed as per Equation 4.1. For the zenith directions 22.5°, 45° and 67.5°, an average was performed across all 9 sensors' responses. The respective background sensors were excluded because, as seen before, they have a different behaviour for lower energy protons. Once more, this averaging is possible due to the expected negligible azimuth dependency due to the isotropic angular distribution of the simulated protons. Nevertheless, all sensors' response functions are presented in Section A of Appendix A. Additionally, no thresholds were applied in the

deposited energies.

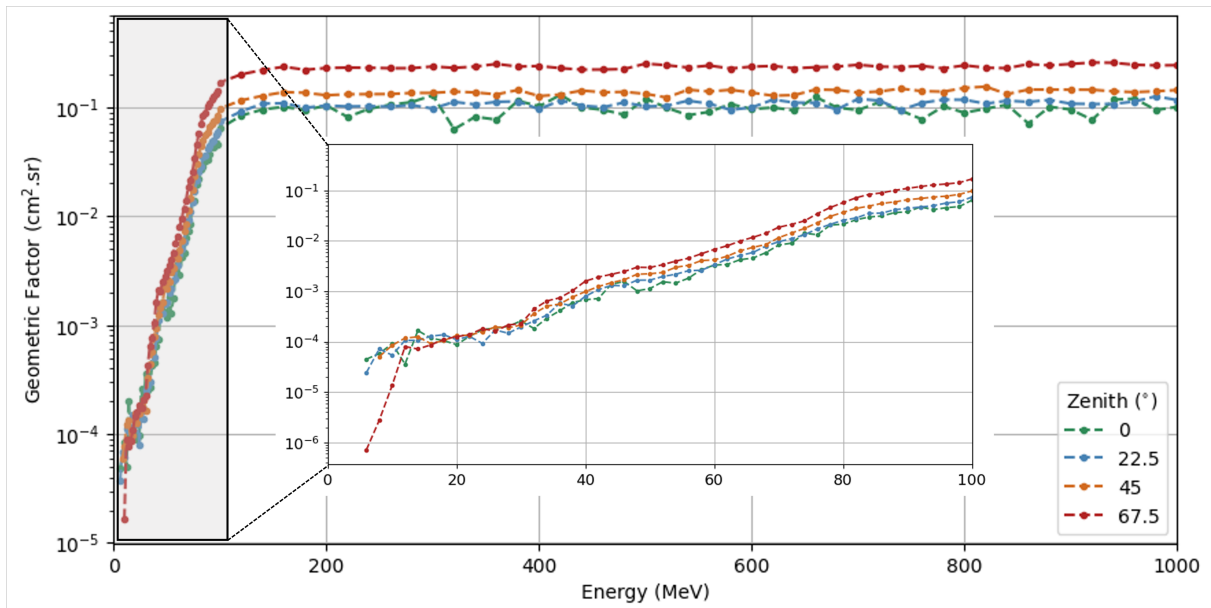


Figure 4.3: Average proton response function of sensors with same zenith direction.

In Figure 4.3, two different regions separated at ~ 100 MeV can be identified. As discussed in Section 2.3.1, trapped protons and electrons within the Jovian magnetosphere can reach energies up to ~ 100 MeV and ~ 1 GeV, respectively. Given the DDH's objective of measuring the angular distribution of electrons, it is crucial to minimise the counts triggered by proton energy depositions in the silicon sensors. This necessity underlies the design of the DDH, whose copper collimator is intended to stop protons with energies up to 100 MeV.

For energies below 100 MeV, various correlations can be made with the precedent analysis. Firstly, it is possible to see that each curve begins at different energy values. The first sensors to register depositions are the ones with zenith 0° and 22.5° , followed by the 45° and, finally, the 67.5° ones. This disparity is due to the presence of the Kapton layer above the sensors, which imposes a cut-off energy for the incident particles. Particles aligned with a sensor of a greater zenith angle must travel a longer path through the Kapton, requiring a higher energy to cross it. Secondly, up to 30 MeV, the geometric factor of different zenith directions is roughly the same. As discussed, at these energies, only protons aligned with the collimator apertures reach the silicon sensors. Given that the FOV of each sensor is approximately the same, a similar geometric factor is expected. Finally, from 30 MeV upwards, it was observed that protons begin to cross the collimator, resulting in an increased number of protons reaching each sensor. Between 30 MeV and 100 MeV, the number of protons reaching the sensors through the collimator rises, consequently increasing the geometric factor.

For energies above 100 MeV all protons are capable of crossing the collimator. Therefore, the geometric factor will reach its maximum and remain at this value as energy increases. It is evident that, at these energies, there is a correlation between sensor's zenith and geometric factor. The higher the zenith angle, the higher its geometric factor. Since protons can cross the collimator and do not need to be aligned with the sensor's aperture to reach it, the sensor's areas will have a major influence in the number of

protons that arrive at the sensor. As explained in Section 3.2.3, sensors with a higher zenith will have a larger area due to the aperture projection in the Silicon plane. As a result, they will register more events when compared to sensors of lower zenith angles as long as the protons can arrive from any direction. The GCR protons will have energies predominantly in this range, therefore a directional analysis is not possible.

Figure 4.4 gathers the average response function of each zenith direction along with the respective background sensor for direct comparison. Below 30-40 MeV, the background sensors present a lower geometric factor since very few protons can cross the collimator. Above 40 MeV, this value increases and so does the response function of the background sensors which begins to converge towards the average response function of the sensors with the same zenith. Notably, sensors with lower zenith angles show a more pronounced difference between sensors and their respective backgrounds, potentially allowing for a better peak-to-background differentiation. Nevertheless, the fluctuation in the geometric factor of the background sensors for energies below 40 MeV suggests that additional simulations in this range would be beneficial to achieve a higher statistical significance.

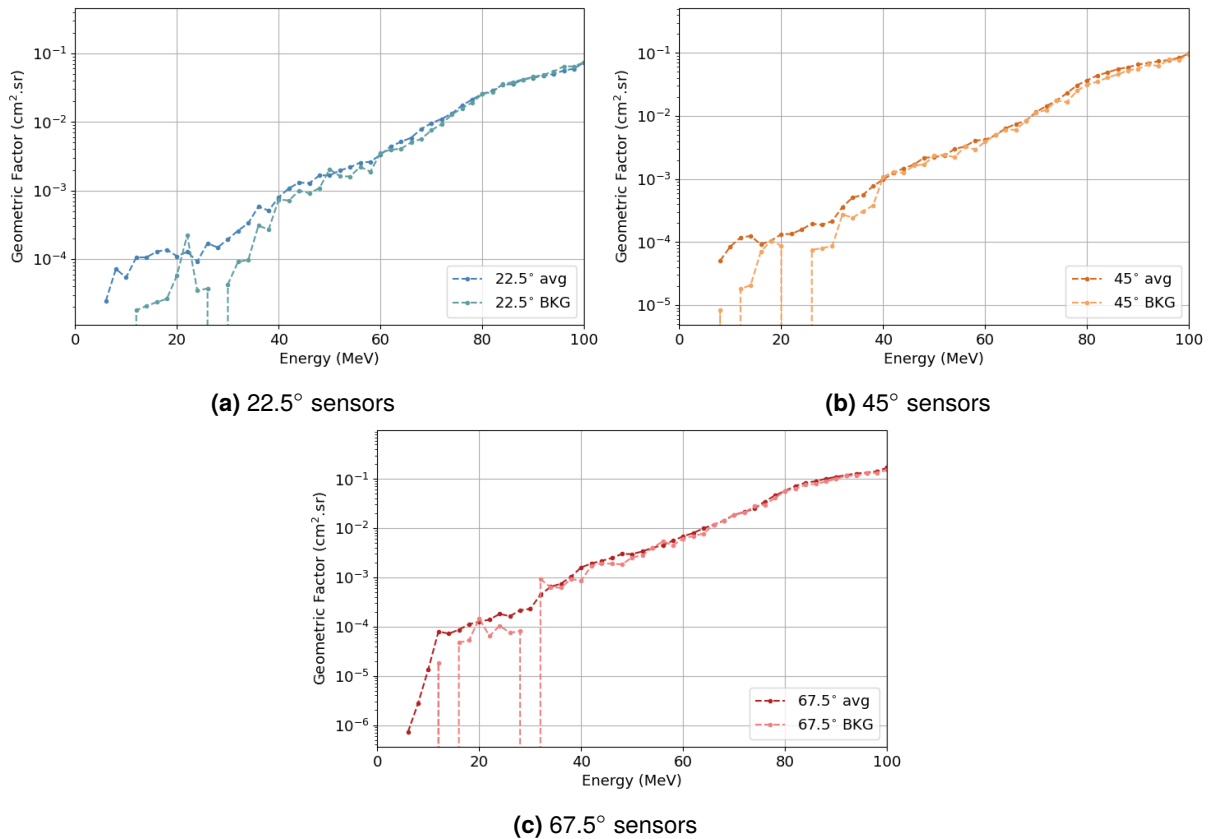


Figure 4.4: Average proton response function of sensors with same zenith direction and respective background sensor.

Threshold Implementation

The thresholds play a crucial role in the detector’s operation, determining which events are vetoed or accepted based on the ASIC’s configuration. For each sensor of the DDH, two programmable thresholds

are available, the LT and HT. In this analysis, it will be explored how varying these thresholds impacts the proton response functions. In the following analysis, the LT will always be operated in coincidence, accounting only for depositions above this value, while the HT will be in anti-coincidence, serving the opposite role. Furthermore, this will be performed for each threshold separately to better understand their individual influence.

Firstly, the LT was scanned, with three values chosen to demonstrate the behaviour of the response function: 0.05 MeV, 0.2 MeV and 0.4 MeV. All zenith directions exhibited a similar behaviour. Only the results for sensors with zenith 67.5° are shown in Figure 4.5. This Figure displays the average response function of the nine sensors with zenith direction 67.5° and of the respective background sensor. The response functions of the remaining sensors are shown in Section A of Appendix A.

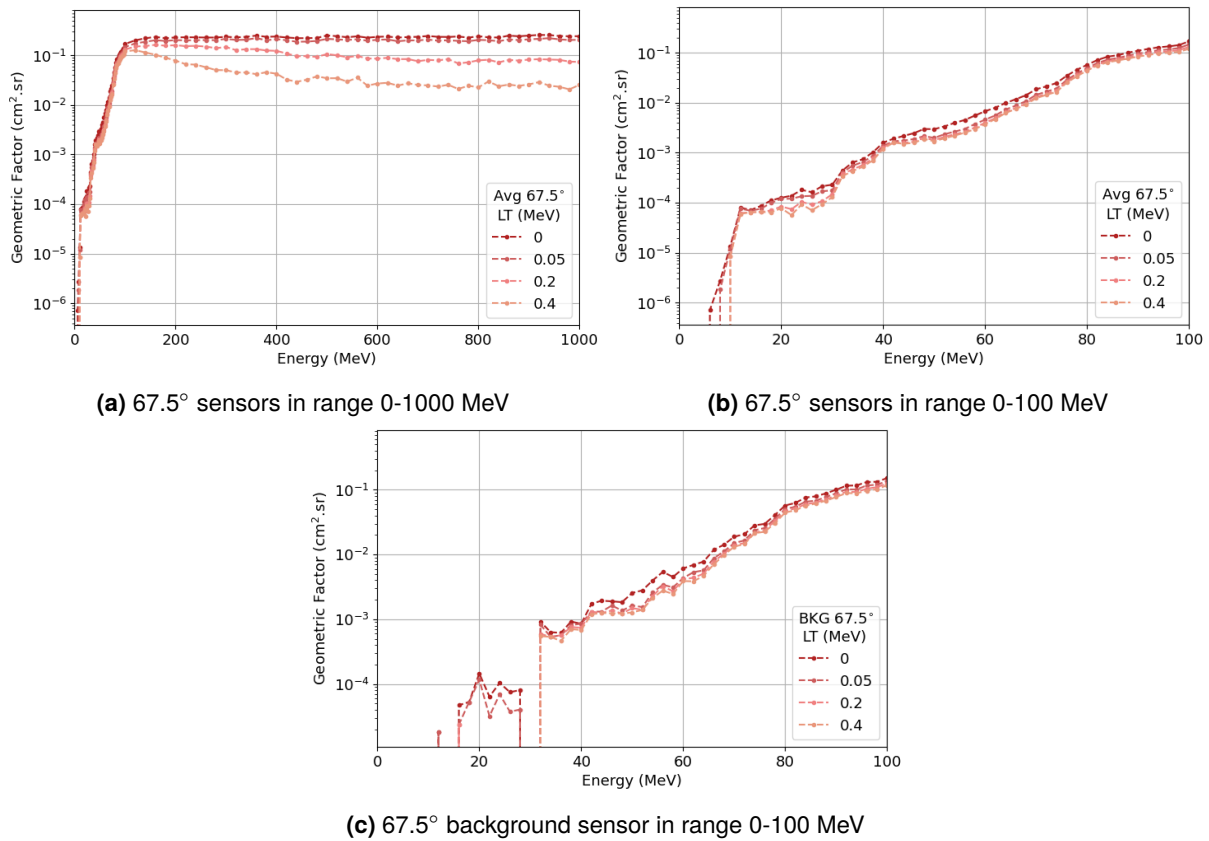


Figure 4.5: Average proton response function of sensors with 67.5° zenith direction for three values of LT.

Figure 4.5a focuses in protons with incident energies above 100 MeV. As seen in Figure 4.2d, protons with these energies deposit less energy in the sensors. Thus, by applying a minimum threshold for deposited energy, several protons that reach the sensor will be excluded from the geometric factor computation, decreasing its value. This decrease will be more pronounced as incident energy increases, since the deposited energy of more protons will fall below the LT value. Consequently, a higher LT results in the exclusion of more protons, leading to a lower geometric factor.

Figure 4.5b shows less energetic incident protons. Similar to protons with energies above 100 MeV, in regions where the mean energy deposition is lower, more protons are excluded by higher LTs, resulting in

a lower geometric factor. This difference is also more noticeable with higher LT values. This is evident in the energy ranges of 15-30 MeV and above 45 MeV, which coincides with the regions of lower mean deposited energy pictured in Figure 4.2d. The same behaviour is observed in the background sensor's response function, displayed in Figure 4.5c. However, it is worth noting that for LT values of 0.2 MeV and 0.4 MeV, the response function only starts around 30 MeV, excluding the protons that cross the collimator with energies lower than the LT.

Once more, a scan was performed for the HT, with four values selected to illustrate its impact in the proton response functions: 9 MeV, 7 MeV, 5 MeV and 3 MeV. The response functions of sensors at different zeniths showed similar behaviour to the applied HT. As done in the LT analysis, only the sensors of zenith 67.5° are presented in Figure 4.6. The response functions for the remaining zenith directions are provided in Section A of Appendix A.

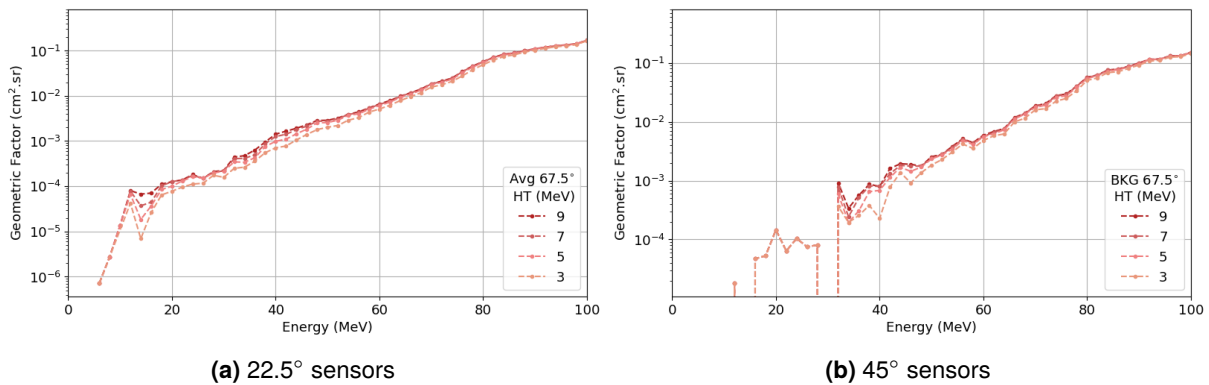


Figure 4.6: Average proton response function of sensors with same zenith direction and respective background sensor.

When applying a HT, if the energy deposited by a proton in the sensor is above its value, it will be excluded from the geometric factor computation. Therefore, the impact of the HT in the proton response function for incident energies above 100 MeV is negligible. In fact, the influence of the applied HT, up to certain values, is only expected to be visible in the energy ranges where no LT influence is observed. This is demonstrated in Figure 4.6a, where the greatest influence is seen for incident energies up to ≈ 15 MeV and in the range 30-50 MeV. These regions coincide with the peaks observed in the mean deposited energy displayed in Figure 4.2d. Unlike what was observed in the LT analysis, no influence on the response function of the background sensor is expected in the initial 30 MeV of incident energies, since the energy depositions in this range are very low. This can be seen in Figure 4.6b, where the difference in the geometric factor is only apparent in the energy range 30-50 MeV.

The conclusions obtained from the LT and HT analysis have implications in the GCR detection. Given that the GCR's energy spectrum exhibits higher proton fluxes in energies above 100 MeV, it is anticipated that the LT will exert a more pronounced influence on the counts recorded by the DDH. However, the HT will still play a significant role, particularly in vetoing heavy ions. By first principles, these particles deposit more energy than protons but will constitute a minority in GCR.

5 | DDH Flight Data Analysis

The JUICE spacecraft was successfully launched on April 14, 2023. Before officially entering its cruise phase, all subsystems and instruments underwent commissioning activities during the Near Earth Commissioning Phase (NECP) in which their proper functioning is verified. This phase began after the completion of the Launch and Early Orbit Phase (LEOP), a critical period for establishing the first communications with the spacecraft, unfolding the solar arrays and confirming its trajectory alignment.

The commissioning activities started on April 16, during which both RADEM's instrument operation and radiation monitoring performances were evaluated. Various tests were conducted including health status checks, ASIC's pulse generator tests, as well as GCR detection in single and coincidence mode. The results from the commissioning demonstrated the proper operation of all DDH sensors. During the GCR detection, scans of the LT were performed whose analysis is presented in this Chapter in detail.

RADEM, due to its role in housekeeping and radiation monitoring, will be in constant operation. During the 8-year cruise phase, the radiation environment will be dominated by GCR and occasional SEP events, all of which will be measured by RADEM. RADEM started collecting data in August 31, 2023 with the flight configurations for cruise phase presented in Section 3.3. In this chapter the measurements made by the DDH channels will be studied and compared with available physical models.

5.1 Galactic Cosmic Rays Data

During commissioning, all DDH sensors demonstrated proper functionality with no operational errors. Nevertheless, the data obtained from these sensors needs to be validated according to theoretical and physical models. This will certify their correct operation in both housekeeping and scientific applications and contribute to better characterising the detector. With the first months of data, the GCR, due to their uniform and almost isotropic flux, are a useful tool for probing and validating these measurements.

5.1.1 Sensor Rate Variation

Throughout the months under analysis, all DDH sensors presented a coherent behaviour excluding two, $45^{\circ}:0^{\circ}$ and $45^{\circ}:80^{\circ}$. Figure 5.1 shows the count rates per unit area during the month of October 2023, which had no SEP events, with one hour binning. It displays three selected sensors from each zenith direction, 22.5° (first row), 45° (middle row) and 67.5° (third row). It also includes the two channels

mentioned above, $45^\circ:0^\circ$ (middle left) and $45^\circ:80^\circ$ (middle right). The data of the remaining sensors is presented in section B of Appendix B.

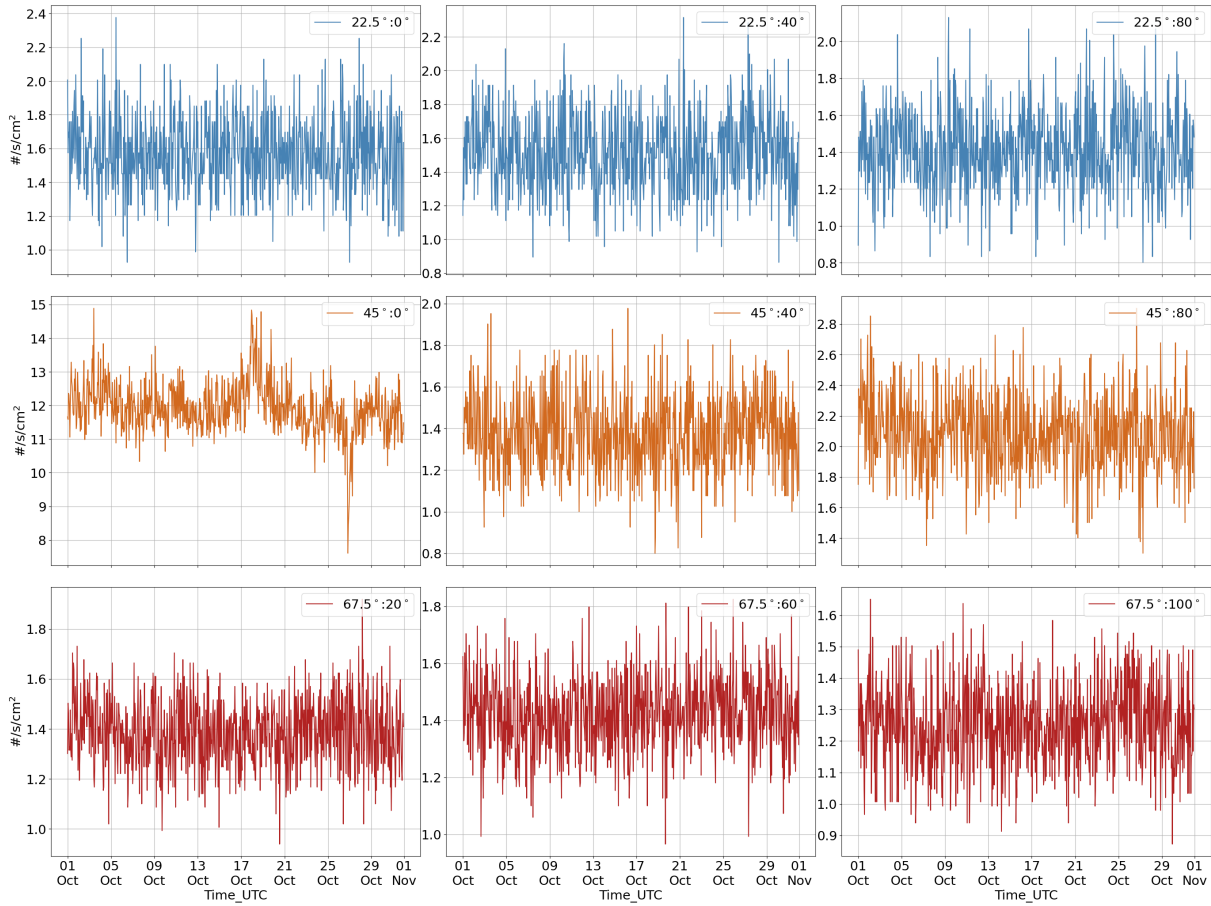


Figure 5.1: Rate per unit area during the month of October for nine selected sensors of the DDH.

The sensors $45^\circ:0^\circ$ and $45^\circ:80^\circ$, part of the group of nine sensors pointing to the 45° zenith direction, during the months under study showed consistently higher counts compared to the others. This revealed high levels of electronic noise, requiring an increase of the sensors' ASIC channel's LT to address the issue. For this reason, the data from these sensors is not reliable and will not be included in the analysis.

The fluctuations and rates across the available months with data were further examined. To achieve this, for each month, a large period of days where no SEP events occurred was selected. This ensured not only large statistics but also that the recorded data solely belonged to GCR. During these time periods and for each sensor separately, all the registered counts were summed and subsequently divided by the total duration, therefore obtaining an average rate during that period. Additionally, the average rate of the sensors that point in the same zenith direction were computed. This allowed a study of each sensor's behaviour and deviation to the mean of the respective group. Figure 5.2 groups this information into eight sub-images, each corresponding to a different period from September 2023 to April 2024. The dashed lines represent the average rate of the sensors with the same zenith direction (and area), while the shadowed area represents the interval of one standard deviation from the mean value.

Figure 5.2a, corresponding to the first month data being collected, reveals the anticipated relation of proportionality between sensor area and registered counts/rate. Although, it is important to note that this

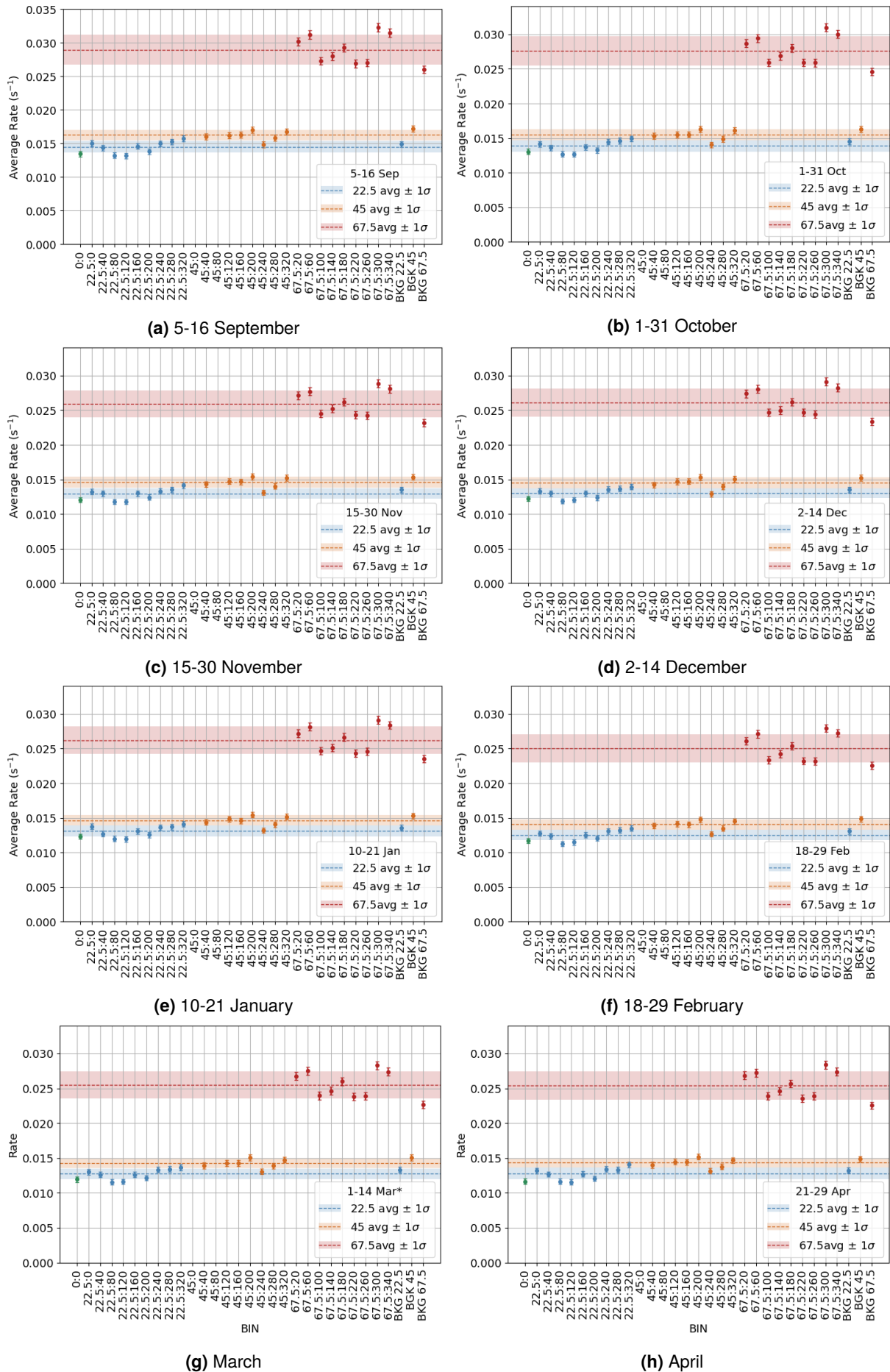


Figure 5.2: Sensor average rates of GCR during different time periods from September 2023 to April 2024.

behaviour is only true for GCR. Because its spectrum is highly energetic, the collimator of the DDH will not stop most of the incident particles but will rather act as an absorber. Additionally, the apertures will not significantly impact the counts, implying that the background sensors should exhibit similar rates to the remaining group with the same area. This proportionality is also in agreement with the response function of protons in Section 4.2.1 which represent 90% of the GCR's constituent particles. For protons with energies above 100 MeV, which can traverse the entire collimator, sensors with larger areas have larger geometric factors. For energies below 100 MeV, protons may either be stopped or align with the apertures, resulting in a residual geometric factor compared to protons with energies over 100 MeV. This discrepancy is further accentuated by the energy spectrum of GCR which extends to extremely high energies and peaks in the hundreds of MeV range, leading to negligible counts from lower energy protons.

Ideally, where all the sensors have the same thresholds and noise levels, it is expected the rate in each sensor to be proportional to its area. As such, the expected order is: Rate (0°) < Rate (22.5°) < Rate (45°) < Rate (67.5°), with the angle representing the zenith direction. This tendency is clear, specifically when comparing the averages made with the sensors with the same area (dashed lines), whose values are presented in Table 5.1.

Table 5.1: Average rate and standard deviation of DDH sensors with same zenith direction for the periods considered from September 2023 to April 2024.

Zenith	September			October			November		
	Avg. Rate (s^{-1})	σ (s^{-1})	σ (%)	Avg. Rate (s^{-1})	σ (s^{-1})	σ (%)	Avg. Rate (s^{-1})	σ (s^{-1})	σ (%)
0°	0.01348	-	-	0.01303	-	-	0.01202	-	-
22.5°	0.01453	0.00088	6.1	0.01386	0.00081	5.8	0.01297	0.00078	6.0
45°	0.01628	0.00077	4.8	0.01549	0.00078	5.0	0.01460	0.00079	5.4
67.5°	0.02898	0.00224	7.7	0.02762	0.00213	7.7	0.02594	0.00195	7.5

Zenith	December			January			February		
	Avg. Rate (s^{-1})	σ (s^{-1})	σ (%)	Avg. Rate (s^{-1})	σ (s^{-1})	σ (%)	Avg. Rate (s^{-1})	σ (s^{-1})	σ (%)
0°	0.01223	-	-	0.01230	-	-	0.01168	-	-
22.5°	0.01302	0.00072	5.5	0.01310	0.00078	6.0	0.01253	0.00075	6.0
45°	0.01451	0.00082	5.7	0.01461	0.00075	5.1	0.01404	0.00072	5.2
67.5°	0.02609	0.00199	7.6	0.02618	0.00199	7.6	0.02502	0.00201	8.0

Zenith	March			April		
	Avg. Rate (s^{-1})	σ (s^{-1})	σ (%)	Avg. Rate (s^{-1})	σ (s^{-1})	σ (%)
0°	0.01194	-	-	0.01166	-	-
22.5°	0.01273	0.00076	6.0	0.01279	0.00082	6.4
45°	0.01428	0.00070	4.9	0.01432	0.00066	4.6
67.5°	0.02548	0.00196	7.7	0.02539	0.00200	7.9

An additional comparison can be made between the ratio of sensor total areas ($2 \times A_{\text{surface}} + A_{\text{lateral}}$) and their corresponding average rate ratios. Three relations using values from September are shown in Equations 5.1, 5.2 and 5.3. The relations hold within the margin of error among all sensors; however, a more significant difference is observed between sensors with smaller areas. This indicates that the sensors are being affected differently by electronic noise, threshold or a combination of both, especially

when comparing the group of zenith angles 0° and 22.5° to the group of zenith angles 45° and 67.5° . These results remain consistent across every month.

$$\frac{Area(0^\circ)}{Area(22.5^\circ)} = \frac{2.51}{2.85} = 0.88 \rightarrow \frac{Rate(0^\circ)}{Avg.Rate(22.5^\circ)} = \frac{0.1348}{0.1453} = 0.93 \pm 0.06 \quad (5.1)$$

$$\frac{Area(22.5^\circ)}{Area(45^\circ)} = \frac{2.85}{3.45} = 0.83 \rightarrow \frac{Avg.Rate(22.5^\circ)}{Avg.Rate(45^\circ)} = \frac{0.1453}{0.1628} = 0.89 \pm 0.07 \quad (5.2)$$

$$\frac{Area(45^\circ)}{Area(67.5^\circ)} = \frac{3.45}{6.04} = 0.57 \rightarrow \frac{Avg.Rate(45^\circ)}{Avg.Rate(67.5^\circ)} = \frac{0.1628}{0.2898} = 0.56 \pm 0.05 \quad (5.3)$$

Examining Table 5.1, it is also evident that the sensor with largest area corresponds to the one with the highest standard deviation (%), indicating a greater dispersion of each sensor's rate around the average of the group. However, the standard deviation relative to the measurements of 45° sensors can be significantly affected by the absence of data from the noisy sensors $45^\circ:0^\circ$ and $45^\circ:80^\circ$. As a result, a clear relation between area and standard deviation cannot be obtained.

Additionally, a study of the average rate's error for each sensor was conducted over the selected periods of time from every month. As expected due to the relation between counts and sensor areas, sensors with larger area exhibit a more stable response compared to smaller ones, as they have higher statistics. Table 5.2 displays the average rate in the selected period of September and respective error for each sensor, also illustrated in Figure 5.2a.

Table 5.2: Average rate error for each sensor in the selected period of September 2023.

Sensor	Avg. Rate ($\times 10^{-2} s^{-1}$)	δ (%)	Sensor	Avg. Rate ($\times 10^{-2} s^{-1}$)	δ (%)	Sensor	Avg. Rate ($\times 10^{-2} s^{-1}$)	δ (%)
22.5°:0°	1.439 ± 0.041	2.83	45°:0°	-	-	67.5°:20°	3.016 ± 0.059	1.96
22.5°:40°	1.377 ± 0.040	2.89	45°:40°	1.537 ± 0.042	2.74	67.5°:60°	3.092 ± 0.060	1.93
22.5°:80°	1.267 ± 0.038	3.02	45°:80°	-	-	67.5°:100°	2.589 ± 0.055	2.11
22.5°:120°	1.262 ± 0.038	3.02	45°:120°	1.551 ± 0.042	2.73	67.5°:140°	2.578 ± 0.055	2.12
22.5°:160°	1.401 ± 0.040	2.87	45°:160°	1.559 ± 0.042	2.72	67.5°:180°	2.807 ± 0.057	2.03
22.5°:200°	1.326 ± 0.039	2.95	45°:200°	1.634 ± 0.043	2.66	67.5°:220°	2.682 ± 0.056	2.07
22.5°:240°	1.437 ± 0.041	2.83	45°:240°	1.422 ± 0.040	2.85	67.5°:260°	2.615 ± 0.055	2.10
22.5°:280°	1.463 ± 0.041	2.81	45°:280°	1.517 ± 0.042	2.76	67.5°:300°	2.990 ± 0.059	1.96
22.5°:320°	1.512 ± 0.042	2.76	45°:320°	1.607 ± 0.043	2.68	67.5°:340°	2.893 ± 0.058	2.00
BKG 22.5°	1.427 ± 0.041	2.84	BKG 45°	1.651 ± 0.044	2.64	BKG 67.5°	2.495 ± 0.054	2.15

While sensors of zenith 67.5° exhibit a smaller error, the difference between sensors of zeniths 22.5° and 45° is less pronounced. These results align with the previous relations obtained in Equations 5.2 and 5.3, which relate the registered counts in each group of sensors. On average the 67.5° sensors have almost 50% more counts than 45° sensors, but the latter only have around 10% more counts than 22.5° sensors, resulting in a similar error. This behaviour is consistent throughout the months under study.

The deviation of each sensor's rate to the average of its zenith group was studied. From Figure 5.2 is clear that all sensors have a consistent response over the months under study, presenting small variations in their deviation from the respective mean. These deviations however, hold significant importance in the study of the directionality of incoming particles.

As previously discussed, it is not possible to study the directionality of incoming GCR. Nonetheless,

one expects to have a rate proportional to the area of the sensors and independent of the its azimuth's direction. Consequently, sensors pointing in the same zenith direction and their corresponding background sensor should have the same rate. However, the sensors' rate consistently deviate from the average rate of the zenith group. This consistency suggest potential differences in the sensors' electronic noise or in the calibration factors relating the thresholds' DAC units to MeV. Since all sensors are configured with the same thresholds, even minor calibration differences can result in the observed deviation.

The deviations observed pose a challenge for the angular distribution analysis, namely in the SEP events which will be discussed in Chapter 5.2 . To conduct a directionality analysis accurately, particles traversing the copper collimator must be excluded. These particles, arriving at the sensor, may have been originated from random directions unrestricted by the sensor's apertures and, therefore, hold no significance in this analysis. The background sensors play a crucial role in this regard. The background sensors measure these particles, enabling for a direct subtraction of counts from their respective sensors. However, for this subtraction to be accurate and not be underestimated or overestimated, all sensors must operate under identical configurations. Accordingly, the deviations being analysed are an indicator that a correction must be applied to future directionality analysis.

An analysis of each sensors' deviation to the respective zenith group average was conducted for each month. The percentage deviation was computed for every month and sensor, with the respective values listed in Section B of Appendix B. To determine the correction factor needed for each sensor's data, averages over the respective sensors' percentage deviations were calculated. These correction factors, along with their errors, are presented in Table 5.3. The correction factor's sign indicates whether the quantity should be added or subtracted. Furthermore, the error, derived from the standard deviation of the values used in the averaging process, provides a insight into their variability. By employing a substantial dataset spanning multiple months, the statistical fluctuations are minimised, aiming for a robust correction factor that accurately reflects the sensor fine-tuning.

Table 5.3: Correction factor to apply to each DDH sensor data.

Sensor	Correction Factor (%)	Sensor	Correction Factor (%)	Sensor	Correction Factor (%)
22.5°:0°	-2.7 ± 1.1	45°:0°	-	67.5°:20°	-4.5 ± 0.7
22.5°:40°	1.1 ± 1.0	45°:40°	1.7 ± 0.5	67.5°:60°	-7.4 ± 0.6
22.5°:80°	9.0 ± 0.5	45°:80°	-	67.5°:100°	5.9 ± 0.4
22.5°:120°	8.8 ± 0.7	45°:120°	-0.6 ± 0.8	67.5°:140°	3.4 ± 0.6
22.5°:160°	0.3 ± 0.6	45°:160°	-0.3 ± 0.5	67.5°:180°	-1.3 ± 0.5
22.5°:200°	4.5 ± 0.6	45°:200°	-5.3 ± 0.4	67.5°:220°	6.7 ± 0.6
22.5°:240°	-4.0 ± 0.7	45°:240°	9.5 ± 1.0	67.5°:260°	6.5 ± 0.5
22.5°:280°	-4.9 ± 0.5	45°:280°	3.6 ± 0.5	67.5°:300°	-11.5 ± 0.4
22.5°:320°	-8.1 ± 1.0	45°:320°	-3.5 ± 0.6	67.5°:340°	-8.3 ± 0.5
BKG 22.5°	-4.1 ± 0.6	BKG 45°	-5.1 ± 0.7	BKG 67.5°	10.6 ± 0.5

Table 5.3 reveals that three sensors exhibit a larger error compared to the correction factor value, namely sensors: 22.5°:160°, 45°:120° and 45°:160°. These sensors are closer to their respective group averages, resulting in minimal corrections. Consequently, the fluctuation in their deviation will lead to values that can be either positive or negative. Moreover, the errors associated with the correction factors of sensors with zenith 22.5° are generally higher, followed by the 45° sensors and finally, the 67.5° ones.

However, is noteworthy that the 67.5° sensors tend to exhibit higher deviations from the average.

5.1.2 Data Validation

After conducting a comprehensive analysis of the flight data from each DDH sensor, it becomes essential to validate it. Despite the majority of sensors exhibiting the expected behaviour, ensuring the accuracy of the collected data is necessary. This validation process involved comparing the observed data with theoretical models of GCR.

The International Standard Organisation (ISO), specifies a model for GCR in Geostationary orbit - ISO15390 -, establishing the model's parameters and characteristic variations in the GCR's particles (protons, nuclei from Z=2 to 92 and electrons) beyond Earth's magnetosphere [45]. The expected proton flux was obtained by PyCreme [46], a Python tool that incorporates a method to generate the GCR flux based on the ISO15390 model. This tool requires as input the 13-month smoothed monthly total sunspot number of at least 2 solar-cycle, obtained from [47], to compute monthly differential fluxes. Figure 5.3 shows the computed GCR proton differential fluxes for five selected months.

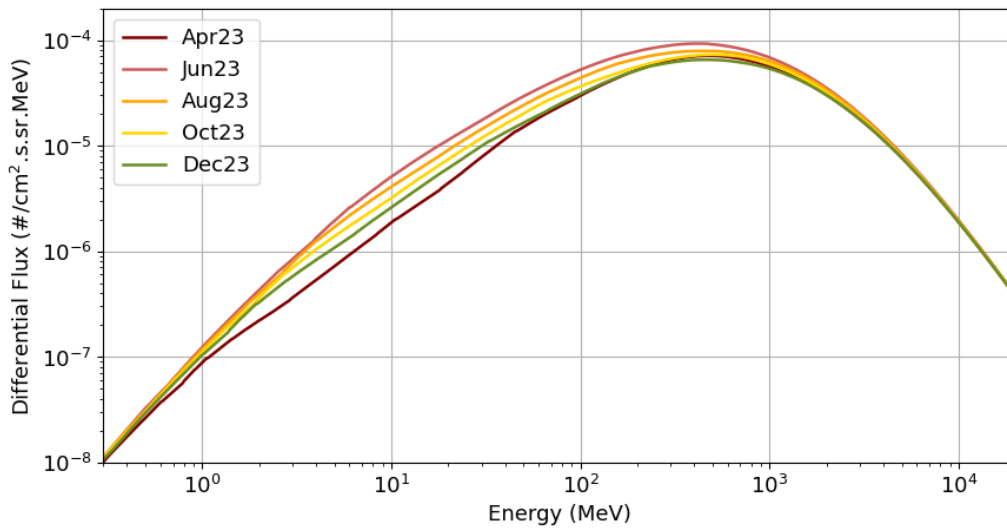


Figure 5.3: GCR proton differential fluxes computed with PyCreme for five selected months.

The GCR proton flux was extracted for the month of October, 2023, to enable a direct comparison with the flight data from that period. The simulated rate in each sensor of the DDH was computed according to Equation 5.4, where $F_R(E)$ is the proton response function of a given sensor and ϕ the expected flux of protons computed with PyCreme. For this comparison to be possible, the threshold values programmed into the ASIC channels during data acquisition (Table 3.7) were applied to the proton response function. The thresholds used in the simulated response functions are given in MeV, therefore the ideal conversion from fC to MeV (1 fC \approx 0.0225 MeV) was applied. Figure 5.4 displays the average rate per unit area during the month of October, showing the simulated values along with the flight measurements made by all DDH sensors.

$$R_{sim} = \int F_R(E) \phi(E) dE \quad (5.4)$$

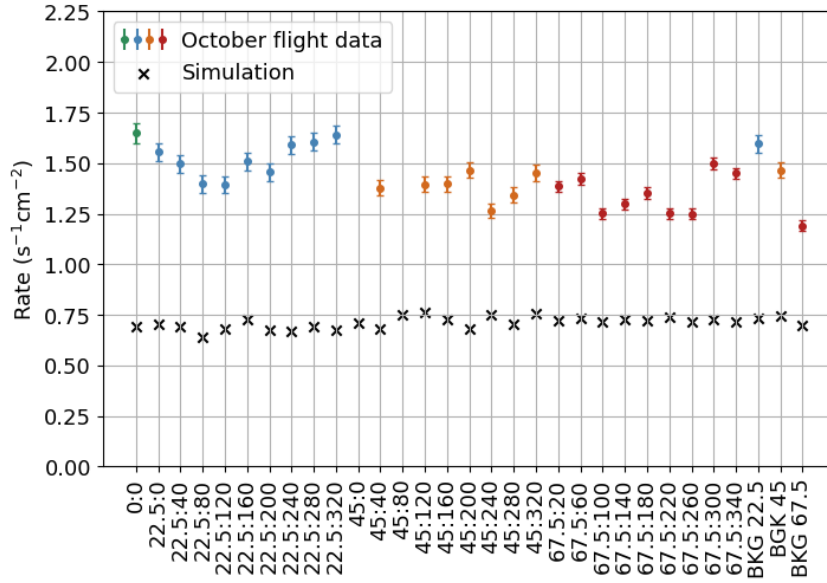


Figure 5.4: Average rate per unit area for each DDH sensor during the month of October and simulated rates using PyCreme. The flight data is coloured according to the zenith angle of the sensor: 0° (green), 22.5° (blue), 45° (orange) and 67.5° (red).

In Figure 5.4, it is visible that while the computed rates have roughly the same value, the flight data exhibits variations among sensors with different areas. Notably, sensors with smaller areas display higher rates per unit area. The mean of the October’s average flight rate for sensors with the same zenith angle was computed. These values are presented in Table 5.4, as well as the mean value of the simulated rate for the same period. Additionally, it includes the ratio between these two values.

Table 5.4: Mean value of the average flight data rate for sensors with same zenith direction and simulated rate during the month of October, 2023. Additional ratio between these two values.

Zenith (°)	0	22.5	45	67.5
Avg. Rate ($\text{s}^{-1} \text{cm}^{-2}$)	1.65 ± 0.05	1.52 ± 0.09	1.40 ± 0.07	1.33 ± 0.10
Avg. Rate Simulation ($\text{s}^{-1} \text{cm}^{-2}$)	0.71 ± 0.03			
$\frac{\text{Avg. Rate}}{\text{Avg. Rate Simulation}}$	2.32	2.14	1.97	1.87

It is noticeable from the presented values that there are differences between each zenith direction, one of which, the gap between the theoretical and experimental value. The flight rate is approximately twice as high as the expected, with the difference being more pronounced for sensors of lower zenith angles. Although, it is important to note that the computed rate only includes the contribution of protons. While protons make up the majority of GCR particles, there is also a contribution from heavy ions that has not been considered yet and will help reduce the disparity between the measured and theoretical values. However, the anticipated increase in the simulated rate will not be able to completely bridge the gap. Additionally, GCR models inherently have associated errors, so having a factor of 2 difference is still within an acceptable range.

More importantly, the sensors’ characterisation may play an even bigger role, as approximations were made for the simulated rate computation. As mentioned, the applied LT in the proton response function was calculated based on first principles. Despite there being an experimental correlation between DAC

and fC, the conversion from DAC to MeV is still unknown. The ideal correlation that was used, not only may yield a different conversion coefficient that truly relates DAC and MeV, but also does not account for the electric noise of the sensors. Therefore, the true LT to be applied in the simulations could be significantly different from the one used so far.

5.1.2.1 Simulated LT scan

To further investigate the reasons for the observed increase in GCR compared to the expected value, the influence of the LT on GCR detection was studied. Monthly fluxes of GCR protons were extracted from PyCreme for the period from April 2023 to January 2024. Additionally, a scan of the LT was conducted in the proton response functions, which were then used in Equation 5.4 to compute the simulated rate for each month. To assess the impact in each zenith direction, an averaging over sensors with the same zenith angle was performed. Figure 5.5 displays the monthly simulated rates alongside the average rate measured by the DDH, presented separately for each zenith angle. Furthermore, for each zenith angle, the expected rate for an ideal LT of 9 fC is presented in grey, corresponding to the programmed LT value of every sensor for the cruise phase, 90 DACs.

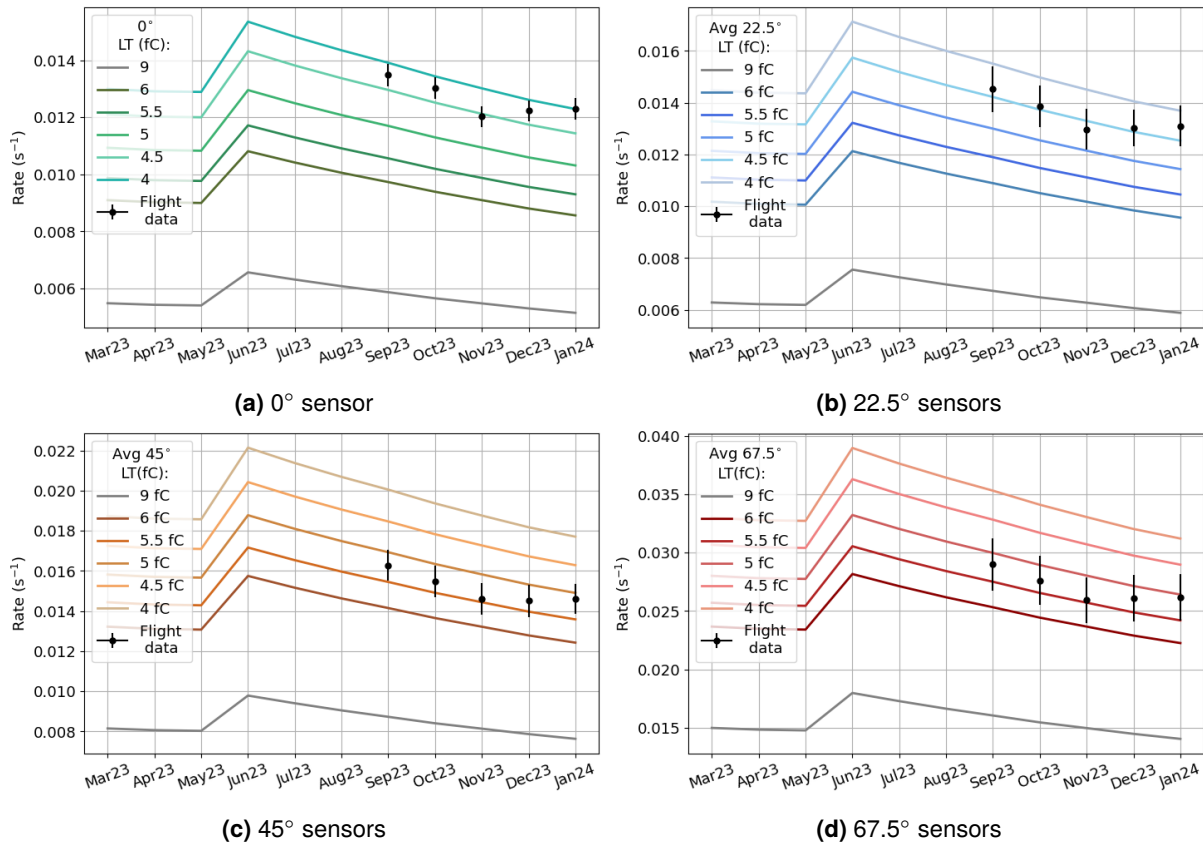


Figure 5.5: Simulated rates using PyCreme for the period from April 2023 to January 2024 and flight data of the GCR average rate from each month. These values are averaged over the sensors with same zenith direction.

Firstly, upon a quick look at Figure 5.5, it becomes apparent that the flight data follows a similar trend to the rate obtained from the GCR model, both displaying a decreasing tendency at similar levels over

the presented months. However, it is notable that the flight data consistently shows a higher rate than expected (grey line). Once more, this discrepancy is more pronounced in sensors with a lower zenith angle. Accordingly, the LT curves that closely match the flight data points have a lower LT value. This is due to the increased number of protons that will be accounted for the response function and contribute to a higher simulated rate. The observed difference in LT values is more apparent in sensors with smaller areas as well.

As previously discussed, the ideal conversion between fC and MeV may not accurately represent their true relationship, especially since the electronic noise of the sensors was not considered. This relation might even differ from sensor to sensor. As seen before, all sensors consistently exhibited small deviations from the average rate of their zenith direction group during GCR measurements. Now, it is also possible to see different behaviours in sensors with distinct areas, a difference suggested in Equations 5.1, 5.2 and 5.3. Consistent with the conclusions drawn from these equations, Figure 5.5 shows that sensors at 45° and 67.5° share a similar LT, ~ 5 fC, whose theoretical curve is the nearest to the flight data points. Conversely, sensors at 0° and 22.5° have a different LT value, closer to 4 fC, which better matches the theoretical curve with the flight data. These observations highlight that the DDH sensors are not all operating under the same conditions, either due to calibration factors, electronic noise or both. This variability could potentially pose a challenge in the directionality analysis of future events. Therefore, it is crucial to conduct a comprehensive characterisation and calibration of all the sensors.

5.1.2.2 Commissioning LT scan

During the NECP, a scan of the ASIC's LT for GCR detection was conducted, forming the basis for in-flight calibrations. The measurements obtained by each sensor at different LT values can be directly compared with the expected from GCR models. It establishes a direct relationship between the DAC units of the thresholds applied in the ASIC channel and the corresponding values in MeV used in the simulations. For this analysis, four sensors, each from a different zenith direction, were selected at random.

In this phase, the counting time interval was set to 500 seconds. The LT value was programmed to change every 20 time intervals, allowing to collect data with the same LT setting for almost 3 hours. Figure 5.6 relates the LT settings with the rate registered in four different sensors, each corresponding to a different zenith direction. During this process, the channel's HT was deactivated, thus the only constraint being the LT.

The scan was conducted in intervals of 10 DACs, starting at 90 DACs, the value chosen for the beginning of the cruise phase. Comparing the rates obtained in April (during commissioning) when the LT was set at 90 DACs with the GCR rate registered during the month of October, an excess of 50% to 80% is observed for April in all sensors. Although a decrease might be expected from April to October as the solar maximum is approached, this discrepancy seems excessive. According to the theoretical flux presented in Figure 5.5, the rates in both months were expected to be around the same value. This suggests that housekeeping parameters, i.e., the temperature, might have differed between the two phases, possibly due to the LT scan being conducted early in the mission where some parameters may not have stabilised yet. If this is the case, the obtained conversion factors may not apply for recent measurements.

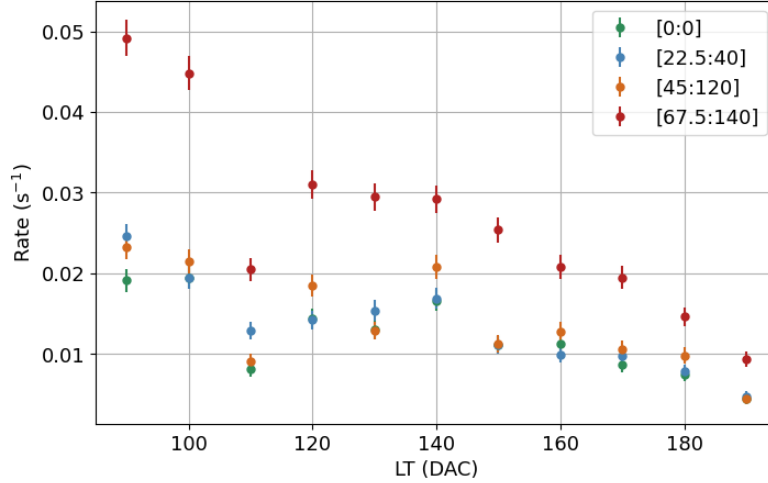


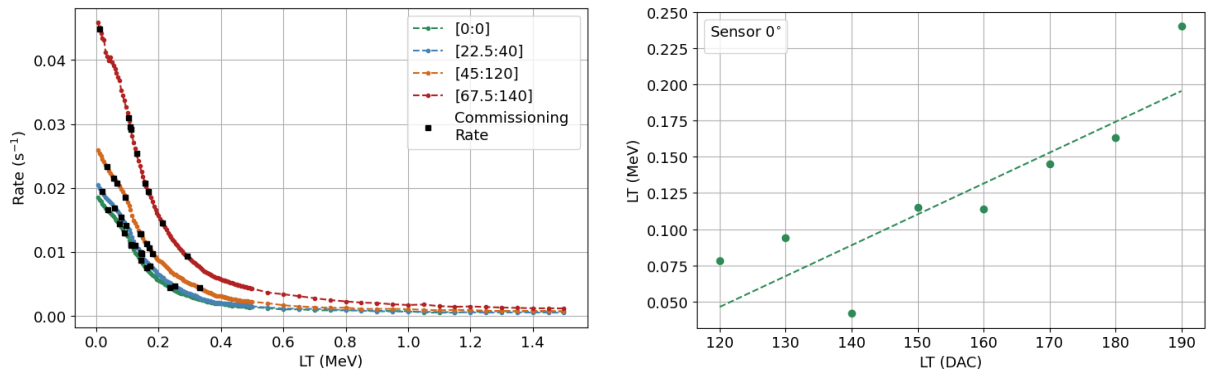
Figure 5.6: Relation between LT value and count rate registered in four different sensors during the NECP, one corresponding to a different zenith direction.

Additionally, for certain LT values, the rates of sensors at zenith angles of 22.5° and 45° exhibit similar values. Despite the difference in sensor areas, it was previously noted that sensors at a zenith angle of 22.5° showed more counts than expected compared to those at 45° . In some cases, sensors at 22.5° displayed higher rates than some at 45° , making this observation not unexpected. Nonetheless, its variation may be due to low statistical significance, and the counting time for a given LT should be increased accordingly. Increased counting time is especially important for higher thresholds, since lower counts rates are expected.

On the other hand, the expected decrease is observed in the rate as the LT value is increased, with the exception of the LT of 110 DACs. This data point will be excluded from the remaining analysis due to its outlier behaviour. The results obtained allow for a direct comparison between the LT set during flight and the LT imposed in the simulation that generate the same rate value. To achieve this, a detailed LT scan was conducted for the simulated rates of the four different sensors, resulting in the curves presented in Figure 5.7a. The LT values were incorporated into the computation of the proton response functions, which were subsequently applied to the April's proton flux, generated by PyCreme [46]. The black squares in the figure indicate the rates found during the commissioning scan, each corresponding to a different in-flight LT value. Correlating these values with the corresponding x-value of the simulated curve will provide the conversion factor from DAC to MeV. Figure 5.7b illustrates the relation between these units, derived for the sensor positioned at a zenith angle of 0° . A linear regression was performed on the presented points using the minimum mean square method. The regression results are summarised in Table 5.5, which also includes the parameters for the other sensors.

Table 5.5: Linear regression parameters for the four sensors under study, relating DAC and MeV units.

Sensor	$m (\times 10^{-3} \text{ MeV/DAC})$	$b (\times 10^{-1} \text{ MeV})$
[0:0]	2.13 ± 0.51	-2.10 ± 0.79
[22.5:40]	2.16 ± 0.34	-2.00 ± 0.51
[45:120]	2.20 ± 0.46	-1.77 ± 0.68
[67.5:140]	2.52 ± 0.32	-2.32 ± 0.48



(a) Simulated rate of the four different sensors for different LT values. Black squares indicate the registered rates during the commissioning scan. (b) Relation between DAC and MeV for the central sensor of zenith 0° .

Figure 5.7

In Table 5.5, the conversion factor between DAC and MeV is denoted by \mathbf{m} . For the first three sensors, this factor is lower than the ideal conversion factor. This value can be calculated by multiplying the known conversion from DAC to fC (1 DAC = 0.1 fC) by the ideal conversion from fC to MeV (1 fC \approx 0.0225 MeV), resulting in 1 DAC \approx 0.00225 MeV. Only the studied sensor at a zenith angle of 67.5° exhibits a higher conversion factor. The parameter \mathbf{b} is directly correlated with the electronic noise of the sensors. All its values are negative because, for the simulated rate to match the flight data, the LT needs to be lower than the converted value to compensate for the counts originating from noise. However, it is worth noting that the parameter values are highly influenced by the data points; removing one data point can significantly alter the parameters.

This analysis, despite giving satisfactory results, strongly indicates that this procedure would benefit from a more detailed and customised study. Firstly, as housekeeping parameters such as temperature and voltage significantly impact RADEM's detector measurements, they should be meticulously controlled. Ideally, their influence should be systematically studied. Secondly, this study would benefit from increased statistical data by extending the duration of data collection. This extension should be personalised based on their expected rates, which vary with sensor area and applied threshold. Finally, obtaining more data points would enhance the results, as only 10% of the available DAC range of the ASIC's channel were utilised.

5.2 Solar Energetic Particle Events

Since the start of RADEM's operation until April 2024, more than ten SEP events were registered by RADEM. Following the detailed study of the DDH sensor measurements of GCR, new insights can be brought for SEP analysis, both in terms of methodological approaches and in understanding of the sensor's response. This section centres on the analysis of the SEP event that occurred between the 24th and 26th March 2024, specifically focusing on the observations made by the DDH sensors.

Figure 5.8 displays the raw count rates per unit area of all DDH sensors during the March SEP event.

The sensors are grouped according to their azimuth angles. While the 22.5° and 45° sensors share the same azimuths, the 67.5° sensors are phased by 20° due to space limitations. For presentation purposes, sensors with zenith directions of 22.5° and 45° that share the same azimuth angle are grouped with the nearest 67.5° sensor. In this case, the sensor which has an azimuth difference of 20° was chosen. Similarly to the GCR analysis, the sensors 45°:0° and 45°:80° are excluded from this study due to their unreliable data. The central sensor, 0°:0°, is presented in the upper left panel of Figure 5.8.

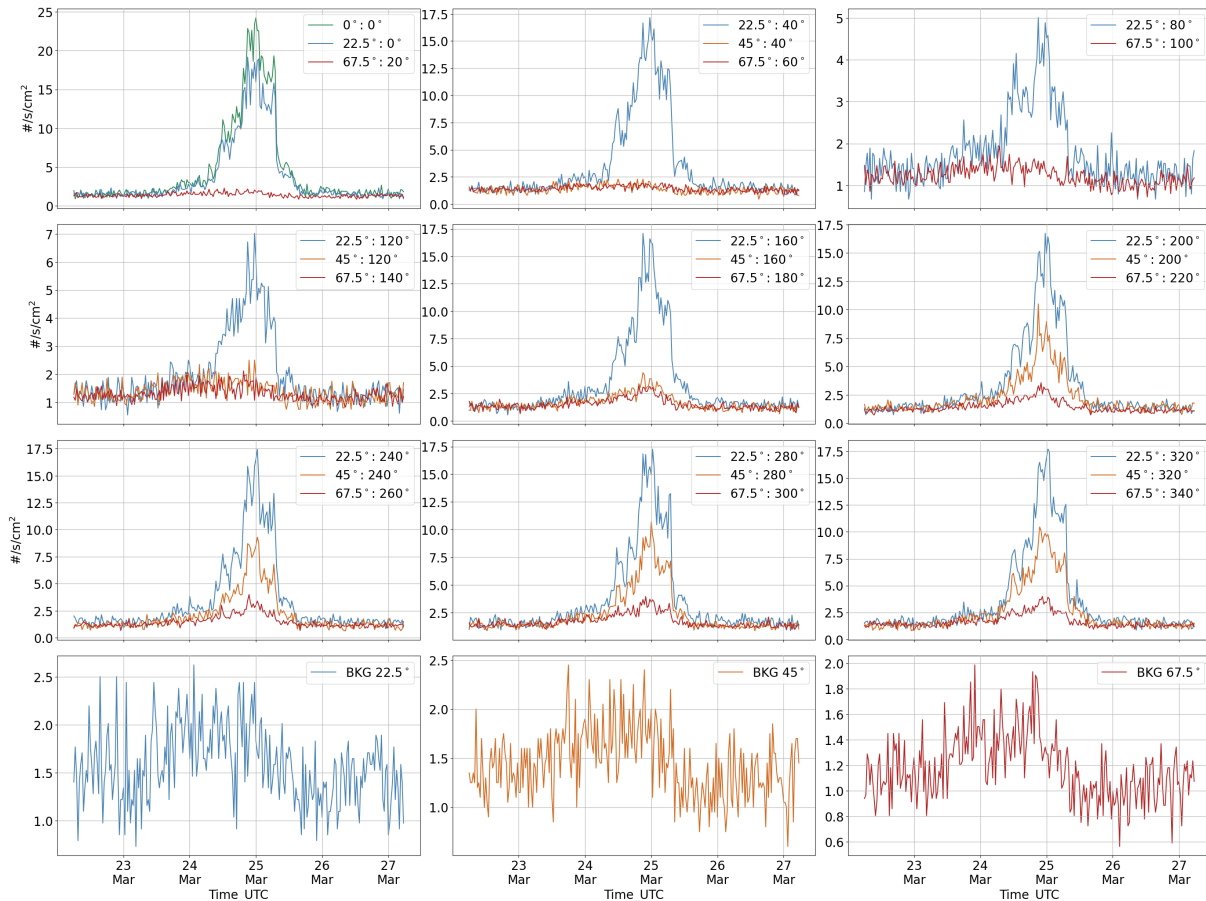


Figure 5.8: Count rate per area of DDH sensors during the March SEP event with integration time of 30 minutes.

In Figure 5.8, a difference between sensors with different zenith angles can be seen. Across all azimuth directions, the rate per unit area is consistently higher for sensors with lower zenith angles. Additionally, in the upper left image, it is also seen that the central sensor exhibits a higher rate than sensors positioned at a zenith angle of 22.5°.

Besides the discrepancy between zenith direction, there is a notable difference between sensors with different azimuth angles. For the 22.5° sensors, those with azimuth angles of 80° and 120° exhibit a decrease in rate of approximately 25% compared to the other sensors in the same zenith group. A similar trend is observed for the 45° sensors, also noticeable at the azimuth angle of 160°, though to a lesser extent. The 67.5° sensors display the same pattern across azimuth angles ranging from 20° to 140°.

The last row of Figure 5.8 presents the rate per unit area of the three background sensors. Notably, this particular SEP event exhibits a lower background rate compared to the rates recorded by the signal

sensors. This will provide a higher signal-to-background ratio, reducing the impact of statistical errors on the analysis process. Moreover, the observed differences between directions make this event particularly intriguing for further analysis.

5.2.1 Rate correction and Background Subtraction

To ensure the accuracy of the analysis for this event, a few corrections are required. As discussed in Section 5.1.1, measurement deviations were observed among DDH sensors with the same zenith angle, despite similar values being expected. This discrepancy was found to negatively impact background subtraction for future directionality analysis. To address this, a correction factor was computed for each sensor.

The correction factors listed in Table 5.3 were applied to the DDH sensors by adding/subtracting the computed percentage value to/from the directly measured data presented in Figure 5.8. Figure 5.9 shows this correction applied to three sensors, each from a different zenith direction, selected for having the highest correction factor.

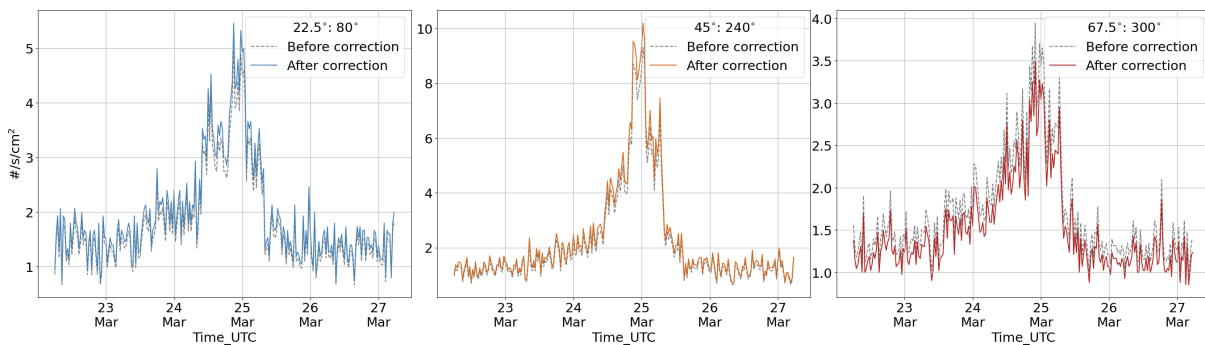


Figure 5.9: Correction factor applied to three selected sensors during the March SEP event, each from a different zenith direction, 22.5°:80°, 45°:240° and 67.5°:300°.

After applying the correction factors, the next step is to subtract the background measurements from the DDH sensors to eliminate penetrating particles. The subtraction is done directly between the corrected data of each sensor and its respective background sensor. The resulting plots are presented in Figure 5.10. The figure shows the SEP's rate per unit area of the DDH sensors, grouped by azimuth angle as in Figure 5.8. Additionally, each plot includes the 67.5° sensor which has an azimuth angle of -20° relative to the grouped 22.5° and 45° sensors. This presentation was chosen to better visualise the differences over the azimuth angle.

Figure 5.10 presents the final computed rate which retains similar structural features observed in Figure 5.8. The raw data indicated that the background sensors exhibited much smaller rates compared to the signal sensors. Consequently, the differences in the SEP's structures after subtracting the background counts were relatively minor. Nonetheless, the removal of background counts resulted in a vertical downward shift. This shift is primarily caused by the subtraction of GCR contributions, which penetrate the DDH collimator and are counted as background. Notably, prior to the SEP event where only GCR contributions are expected, the rate oscillates around zero in all sensors, serving as a reliable indicator of

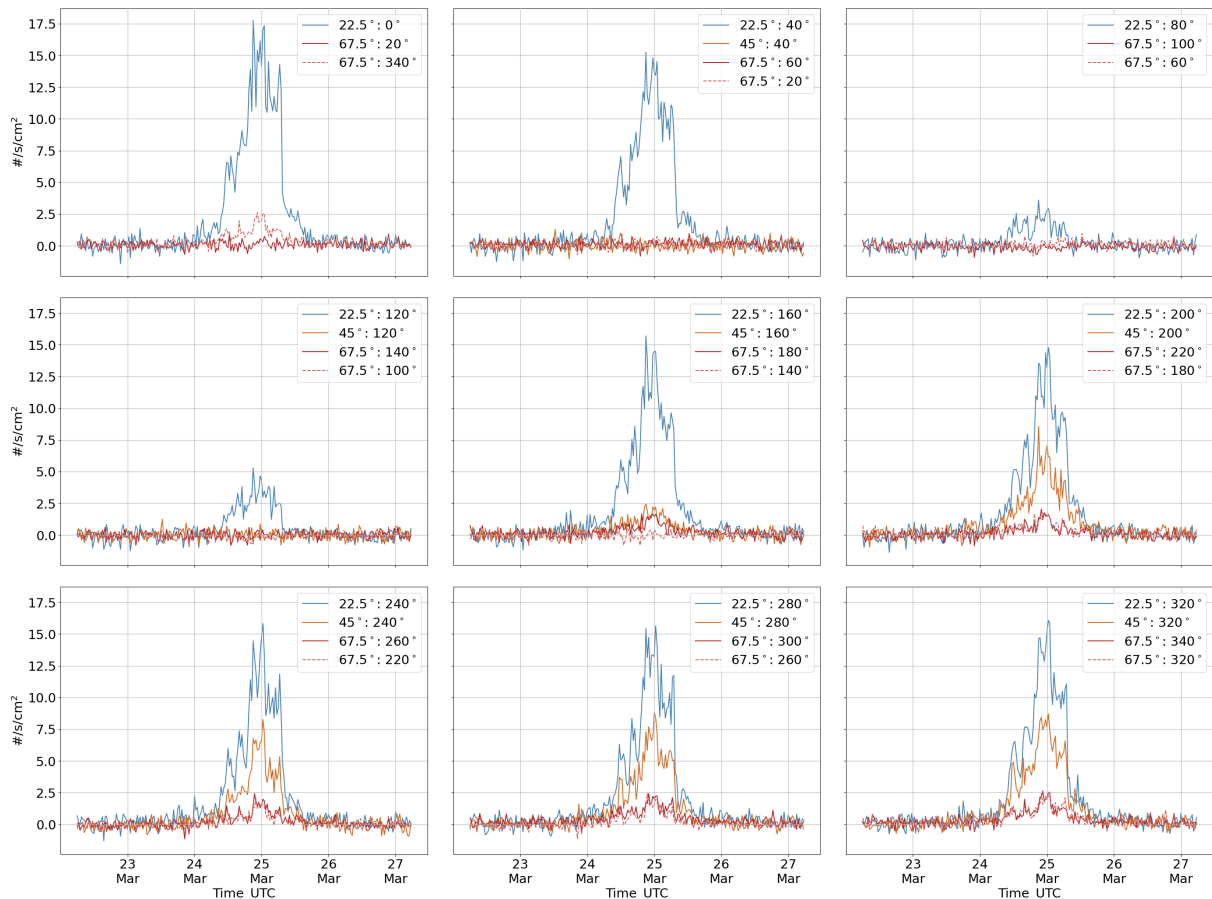


Figure 5.10: March SEP's corrected rate per unit area of the DDH sensors.

the applied corrections.

SEP events are mainly consisted of protons and to a lesser extent, electrons and ions. Based on the notable difference observed between the background counts and the counts registered by the other sensors, taking only protons into consideration, it can be inferred that the majority of protons involved had energies below 100 MeV. This deduction is drawn because protons with energies above this threshold would cross the collimator, reaching background sensors as well as others. Furthermore, by comparing the proton energy response function of a sensor from a given zenith angle with its respective background (Figure 4.3), it is seen that background sensors have a similar response to the average of their zenith group for proton energies above ~ 40 MeV. Given the considerable difference observed between the counts registered by the signal sensors and respective backgrounds, it can be further expected that most of the protons' energies were below 40 MeV. Figure 5.11 assembles the rate per unit area registered by the first five detectors of the PDH. Sensor D2 was excluded due to its high electronic noise. It is possible to see that, already for the D5 detector, the counts are significantly low. Protons need a minimum energy of 35 MeV to reach this sensor, supporting the expectations based solely on the DDH data, where most of the protons' energies were below 40 MeV.

The variations in count rates across sensor directions are also evident in Figure 5.10. First, the rate per unit area is consistently higher for sensors with lower zenith angles across all azimuth directions. Throughout the analysis of the GCR data, it was concluded that the DDH sensors exhibited variations in

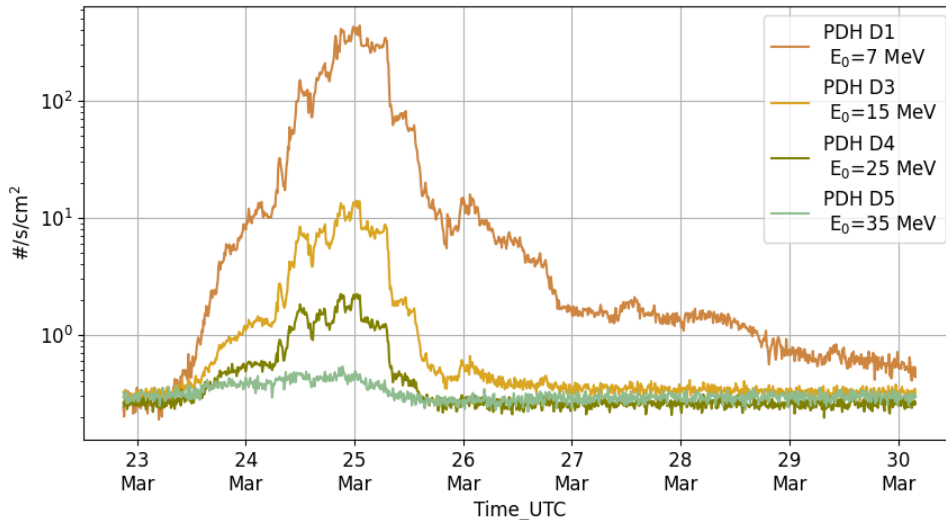


Figure 5.11: Rate per unit area of the March SEP event registered by the sensors D1, D3, D4 and D5 of the PDH. E_0 is the cut-off energy of the given sensor for protons.

their operational conditions, particularly in their thresholds, due to the difference in conversion factors, electronic noise, or both. This leads to differences that were particularly observed between sensors of zenith 0° , 22.5° and sensors of zenith 45° , 67.5° in Figure 5.5. The first group, when compared to the second one, presented a higher gap between the flight data and the simulated rates for the on flight threshold (9 fC). This can therefore be a reason for the observed differences between zenith angles, a topic that will be further explored in the next section.

Secondly, in Figure 5.10, a significant reduction in counts is also observed for azimuth angles between 20° and 160° . For sensors with a zenith angle of 22.5° , this reduction is only evident for azimuth angles of 80° and 120° . Additionally, it is noticeable that within these intervals, the sensors with zenith angles of 45° and 67.5° have their counts reduced almost to zero. These observed differences in count rates, both in azimuth and zenith, may indicate an anisotropy in the studied SEP. This topic will be discussed in the next section after analysing the time evolution of the event.

5.2.2 Time evolution of event

For a more detailed analysis and comparison of rates among different directions, the SEP was divided into intervals, as shown in Figure 5.12. These intervals were chosen by separating the visible features in the measurements of sensor $0^\circ:0^\circ$. Unfortunately, RADEM was the only operating instrument on JUICE, meaning that no other characteristics of the interplanetary environment such as magnetic field, solar wind, i.e., were available to provide context about the particle population.

The first subplot, Figure 5.13a, corresponds to the initial time interval, selected before the SEP begins. During this period, it is expected that by performing the background subtraction, the rates of the sensors will be close to zero. This is observable for most of the sensors whose error bars enclose the zero value. This is a good indicator that the methods applied for the SEP analysis are accurate.

From Figure 5.13c to Figure 5.13g, the angular distributions are similar despite the changes in the

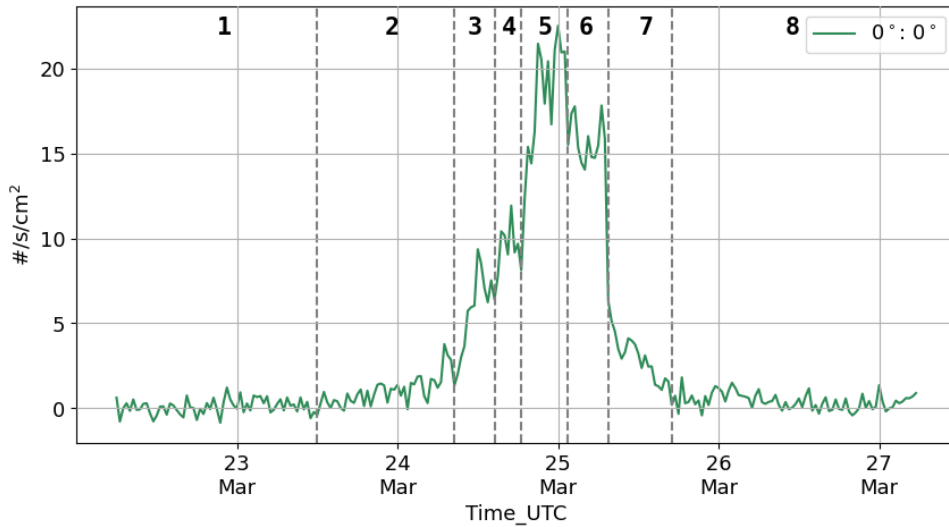


Figure 5.12: Rate per unit area of the March SEP event registered by the sensor 0°:0° and chosen time intervals for posterior analysis.

absolute values of the average rate. As previously discussed, there are clear differences across zeniths and azimuths. The origins of such discrepancies are crucial to understand the angular distribution of the SEP event.

The presence of a higher rate for lower zenith angles is consistent across all azimuth angles. As noted earlier, it is likely that all sensors have their relative counts under or overestimated due to differences in threshold settings, such as DAC to MeV coefficients and electronic noise. This, however, is challenging to evaluate. The GCR calibration performed during the commissioning phase did not yield reliable results that could be further applied. This calibration will be repeated in the future, as it is critical for understanding the sensor's response. Additionally, since the incident particle energy spectrum is unknown, the implications of these differences are not quantitatively tangible. With the information of the particle spectrum along with correct calibration factors, simulations could be performed in order to study the influence of such factors. Nonetheless, the observed differences seem too significant to be solely attributed to these factors. Particularly, the difference between sensors at zenith angles of 45° and 67.5°, which did not show much discrepancy in GCR measurements, can show a difference of more than 50% in this event.

From previous work during the development of the DDH, the response of the detector to the JUICE Radiation Environment was studied [40]. The zenith distribution was analysed for two phases of the Jupiter mission: the Ganymede 5000 km orbit phase (Phase 5a) and the Europa flybys (Phase 2). An isotropic flux of electrons was generated for this study with the expected energy fluxes of Figure 2.6. The obtained results are presented in Figure 5.14, where the count rates corresponding to each direction were averaged over the respective nine azimuthal sensors.

Despite the omnidirectionality of the generated flux, each direction exhibited different sensitivities, both between zeniths and phases. These variations arise not only from the angular dependence of the electron energy threshold set by the absorber and the sensor areas, but also from the variability of electron spectra hardness. The spectral hardness is a measure of the energy distribution, indicating the relative proportion of high-energy particles to low-energy ones. Comparing the phases under analysis in Figure

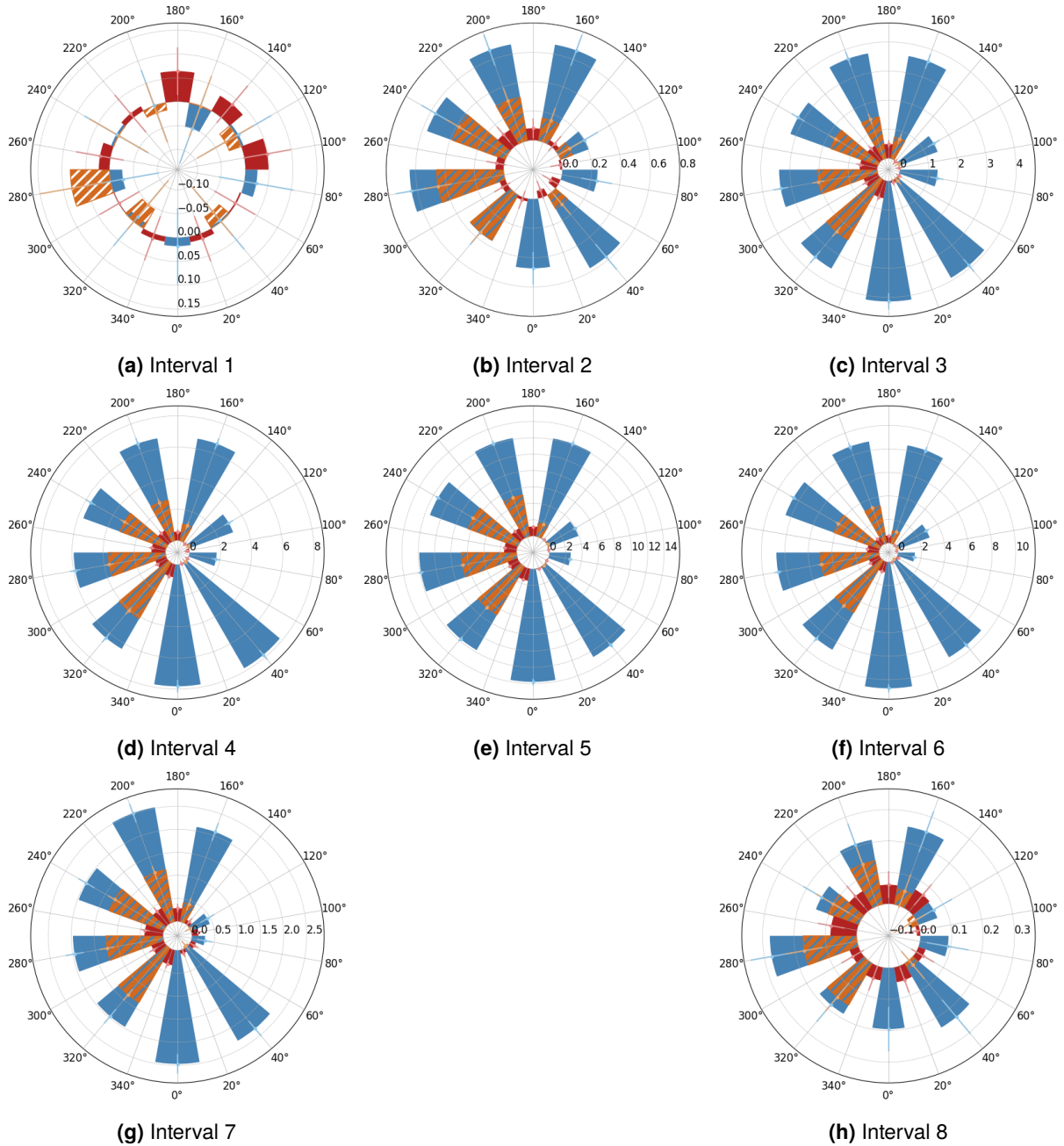


Figure 5.13: Average rate per unit area ($\text{s}^{-1}\text{cm}^{-2}$) of the DDH sensors for the chosen intervals. Each colour bar corresponds to a different zenith direction: 22.5° (blue), 45° (orange) and 67.5° (red). The angular values represent the azimuth direction of each sensor.

2.6a, Phase 2 not only has a higher electron flux at higher energies than Phase 5a, but also presents a lower flux at lower energies (below 10 MeV). Therefore, Phase 2 exhibits a harder electron spectrum than Phase 5a. This difference, along with the other mentioned factors, impacts the direction sensitivity and signal-to-background ratio.

The same principles can be applied to the SEP. Different sensitivities should be expected for different zenith angles during the event under study, particularly a higher sensitivity for lower zenith angles. However, because the energy spectrum is not available at the moment, further investigation is not possible. During the event, both the PDH and EDH were collecting data in non-coincidence mode, making it difficult to

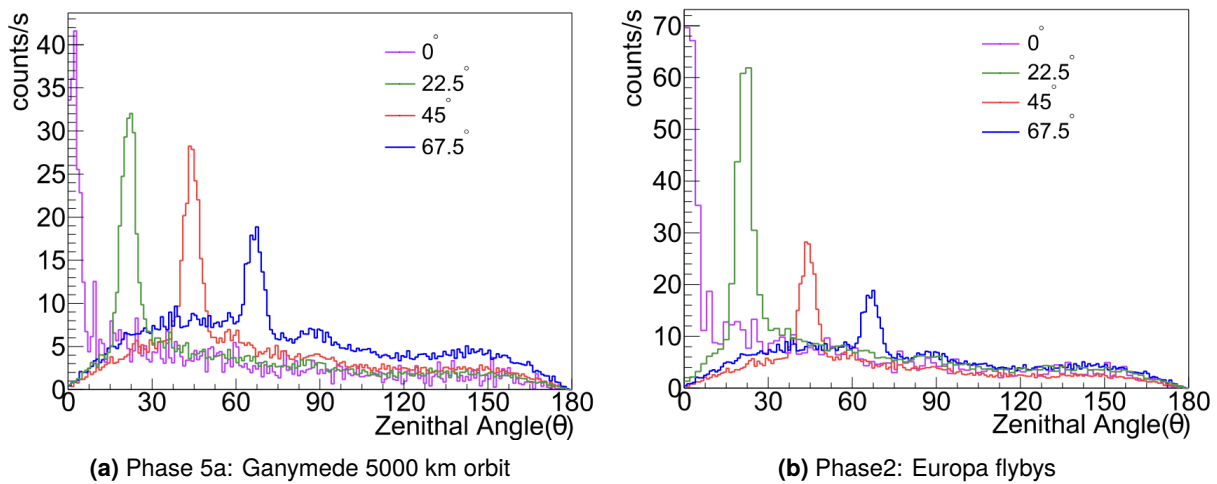


Figure 5.14: Average electron count rates over sensors with same zenith angle for two phases of the JUICE mission. Electrons were simulated omnidirectionality and according to the expected fluxes for each phase. [40]

obtain the particle's energy spectrum. Consequently, it is impossible to conclude whether the observed difference is due to the anisotropy of the event, different sensitivities and calibrations or both. This highlights the importance of inter-calibrating the DDH with the other detector heads to obtain a more accurate description of the flux angular variability.

For the azimuth directions in the mentioned figures (Figures 5.13c to 5.13g), there is a clear reduction in counts around azimuth 90°. For the 22.5° zenith sensors, all azimuths — except for 80° and 120° — have rates that do not vary by more than 20%. However, when comparing these sensors to the ones at azimuths 80° and 120°, reductions of more than 60% are observed. The same reduction pattern is noted in the 45° zenith sensors at azimuths 40°, 120° and 160°, while the remaining azimuth directions yield similar values. It is worth remembering that the 45°:0° and 45°:80° sensors are not represented due to their unreliable data. Finally, the 67.5° zenith sensors show reduced counts in four azimuth directions: 20°, 60°, 100°, and 140°, with rates that can reach zero. The consistency of the decrease in counts around azimuth 90° across all zeniths may indicate an anisotropy of the registered event. Additionally, sensors with higher zenith angles seem to be more affected, showing a significant decrease in their rates over a larger azimuth interval.

It is important to note that the sensors with an azimuth of 90° point in the direction of the -y axis. This corresponds to the side of the spacecraft's vault, as illustrated in Figure 4.1. It is possible that this structure shadows part of the sensor's FOV, attenuating or even stopping incoming particles. To test this hypothesis, the same analysis was performed for two more intense SEP events recorded by the DDH. The decrease in counts in the sensors surrounding the azimuth 90° is also present, although to a lesser extent. It is therefore possible that the observed decrease is a consequence of the vault's shadowing. However, further study is necessary to understand its impact on the sensors' operation.

6 | Summary and outlook

In this thesis, the first flight data analysis of the DDH was performed. The main objectives were to characterise the DDH sensors' response to incident particles and to analyse GCR and SEP event observations made during JUICE's first year of cruise.

Proton and electron Monte Carlo simulations were performed using Geant4 to obtain the response functions of all DDH sensors. The sensor's energy response function of protons were thoroughly studied to comprehend the data, GCR and SEP, as they mainly consist of protons. The differences between sensors of different zeniths and between signal and background sensors were quantified in order to evaluate flight observations. The impact of both low and high thresholds on proton detection was also investigated. Moreover, the observations made during the analysis were found to validate the design of the DDH for its primary objective: measuring the angular distribution of electrons in the Jovian magnetosphere.

To analyse GCRs, large time periods of each month (from September 2023 to April 2024) with no SEP events were selected. For each month, the observed data showed the expected proportionality between rate and zenith angle, consequence of the sensors' area. However, a discrepancy on relative counts was found between sensors of different zeniths, specifically between zeniths 0° , 22.5° and 45° , 67.5° . This suggested differences in operational conditions, such as electronic noise levels and thresholds. Additionally, consistent deviations from a given sensor's rate to its group's average rate (formed by the sensors with same zenith) were observed, while, according to the simulations, similar rates were expected. Based in the percentage deviations between each sensor's rate and the average rate of its group, correction factors were computed. The maximum computed percentage deviation, in absolute value, was of 11.5% for the $67.5^\circ:300^\circ$ sensor, and the minimum was of 0.3% for sensors $22.5^\circ:160^\circ$ and $45^\circ:160^\circ$. These correction factors are important for directionality analysis, as they allow for a more accurate background subtraction, reducing over or underestimations of the sensors' rate.

Absolute GCR count rate was also compare to the ISO 15390 theoretical model. The monthly expected proton flux from April 2023 to January 2024 were obtained. By applying the theoretical LT used in flight, the expected monthly rates were computed for each DDH sensor. These values were directly compared with the GCR flight rates obtained during October, revealing a discrepancy of approximately a factor of two. This difference was more pronounced for zeniths 0° and 22.5° than for the others. Despite the theoretical model having an associated error, the calibration of the DDH sensors is a more likely source for this gap. During the simulated rate computation, first principles were applied to the LT value, which do not accurately account for the real conversion from DAC to MeV or the presence of electronic noise.

The impact of LT on GCR count rate was thus studied by applying different LT values to the expected proton flux for the months under study. The obtained values were after compared with the flight rate. The flight rates of sensors with zenith angles 0° and 22.5° were closer to the computed rates with an ideal LT of 4.5 fC, rather than the LT used in flight (9 fC). Sensors with zenith angles 45° and 67.5° had flight rates that were closer to those computed for an ideal LT of 5.5 fC, further indicating the difference in threshold and electronic noise between these two groups. Once again, the calibration of the DDH sensors proves to be crucial for the detectors' operation and analysis.

Additionally, the LT scan performed during the NECP was studied, aiming to establish a relation between DAC and MeV and characterise the sensors' electronic noise. However, higher than expected rates were observed, attributed to unstable housekeeping parameters, naemly temperature, that likely affected data acquisition, specifically electronic noise levels. Consequently, the results are not reliable. Moreover, due to the relatively small DDH sensor areas, their calibration with GCR data needs extended acquisition times and would benefit from a broader range of tested thresholds.

The March SEP event, chosen for its high intensity, low background, and observed directional differences, was also analysed. The energy of most incident protons during this event was concluded to be below 40 MeV, consistent with the counts observed in the PDH. The SEP's angular distribution was determined by applying the correction factors computed from the GCR data analysis, followed by background subtraction to each DDH sensor. It was found that sensors with smaller zenith angles consistently showed higher counts across all azimuths. However, this behaviour could not be solely attributed to a potential anisotropy of the SEP event. The sensitivity of each zenith detector is highly dependent on the energy threshold set by the absorber and the sensor areas, as well as the spectra hardness. Sensitivity to these parameters is higher for lower zenith angles and therefore a higher rate is expected for these detectors. Additionally, a discrepancy in counts was noticeable across azimuth directions, particularly around the 90° direction. This reduction in counts was observed in two other events as well, suggesting a potential issue with this particular direction. One possible explanation could be the presence of the spacecraft's vault, which aligns in this direction, potentially affecting particle detection.

This work was the first to comprehensively validate RADEM data. The thorough analysis of GCRs, used to characterise the DDH, and of the registered SEP event provided new insights into its performance and operation.

6.1 Future Work

As observed on multiple occasions, the lack of a reliable conversion between DAC to MeV, coupled with unknown levels of electronic noise, makes it extremely difficult to characterize the DDH. Therefore, conducting a new threshold scan of the DDH sensors using GCR data is imperative. From the NECP test, it was concluded that the duration of data collection should be increased and customized according to the expected rates, which are highly dependent on sensor area and applied threshold, along with testing a broader range of thresholds. This calibration is already planned and will be conducted in the near future for the LT of all DDH sensors. Additionally, future calibrations of the HT should be performed, along with

investigations into how housekeeping parameters influence both LT and HT.

In this thesis, only protons were considered for the simulated rates when computing the DAC to MeV coefficients from the NECP LT scan. Future work should also include α particles and even some heavier nuclei to build a more accurate model.

Inter-calibration of the DDH sensors with the PDH and EDH is also a crucial step for the directionality analysis. The sensitivities of each zenith need to be assessed according to incoming particles' energy spectrum to accurately determine their angular distributions. In August 2024, the JUICE spacecraft will perform a Moon-Earth flyby, presenting a significant opportunity for angular measurements. This flyby also marks the first opportunity to inter-calibrate RADEM with other instruments onboard JUICE, such as JoEE (Jovian Energetic Electrons), part of the Particle Environmental Package (PEP) of JUICE.

The Earth flyby will also provide an opportunity to validate the measured data and the performed calibration. Theoretical models of the Earth's radiation belts and trapped particles should be employed, along with the computed response functions for electrons and protons, to obtain the expected measurements.

To conclude, the DDH sensors with azimuth directions close to 90° should be investigated using SEP observations and the future Moon-Earth flyby to find the root cause for their lower count rate. The potential influence of the spacecraft's vault should be assessed.

Appendices

A | Complementary figures - Response Functions

Proton Deposited energy vs Incident energy

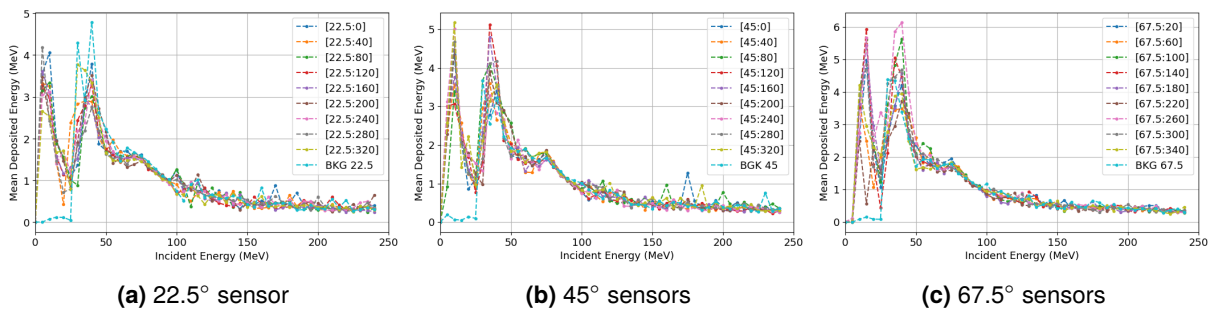


Figure A.1: Deposited energy as a function of the proton incident energy for all DDH sensors.

Proton response Functions

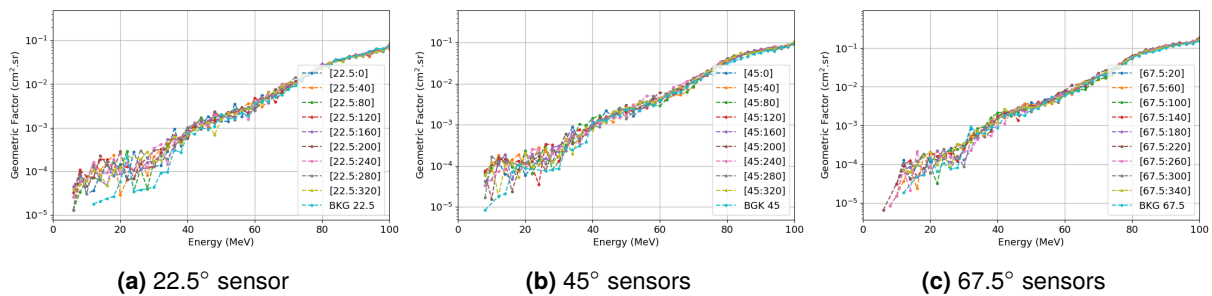


Figure A.2: Proton energy response function of all DDH sensors.

Threshold Implementation

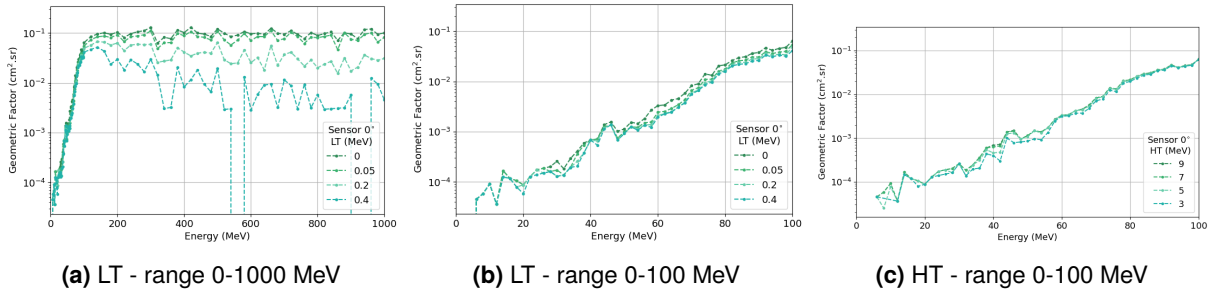


Figure A.3: Proton response function of the central sensor, 0° zenith direction for three values of LT and HT.

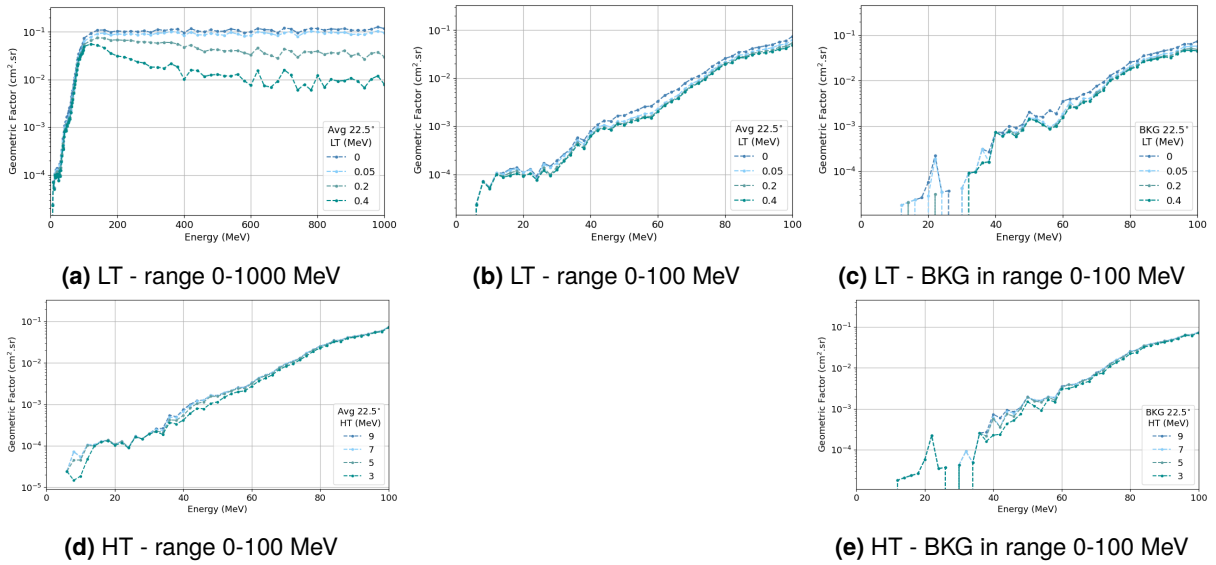


Figure A.4: Average proton response function of sensors with 22.5° zenith direction for three values of LT and HT.

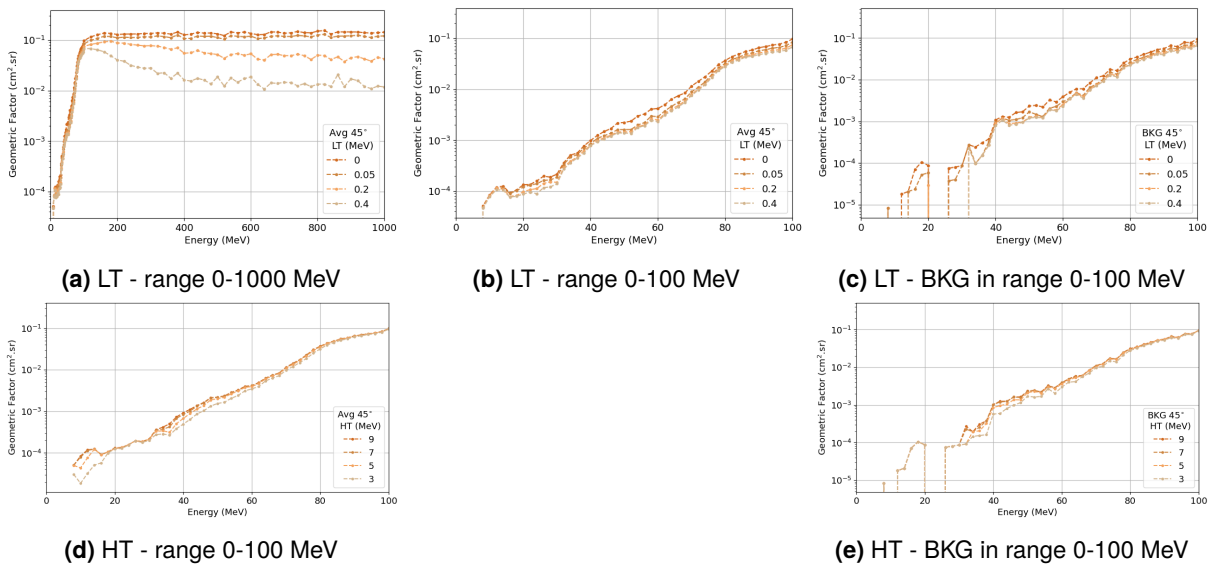


Figure A.5: Average proton response function of sensors with 45° zenith direction for three values of LT and HT.

B | Complementary data - GCR

Rate per unit area during month of October

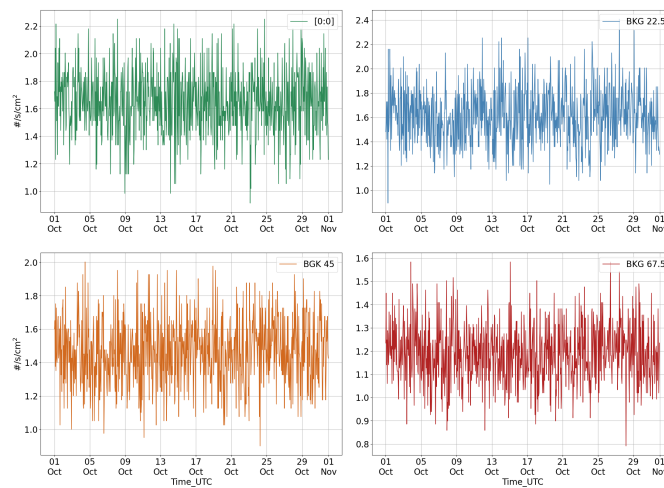


Figure B.1: Rate per unit area during the month of October for the central sensor, 0°:0°, and background sensors of all zeniths of the DDH.

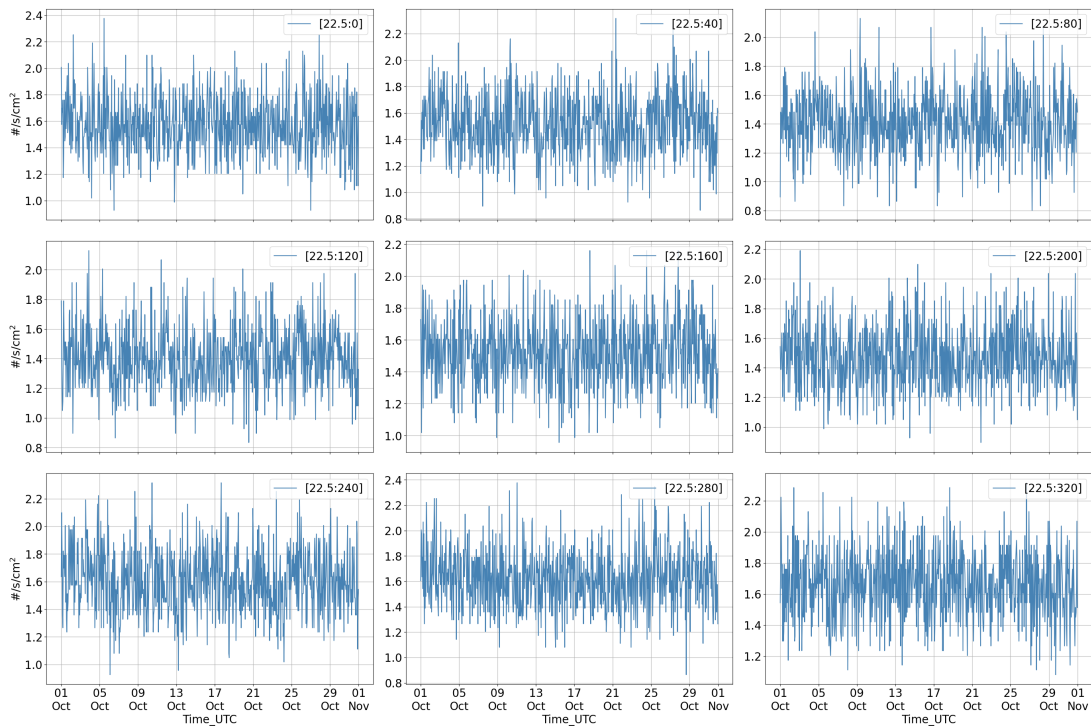


Figure B.2: Rate per unit area during the month of October for the nine azimuth sensors with zenith 22.5° of the DDH.

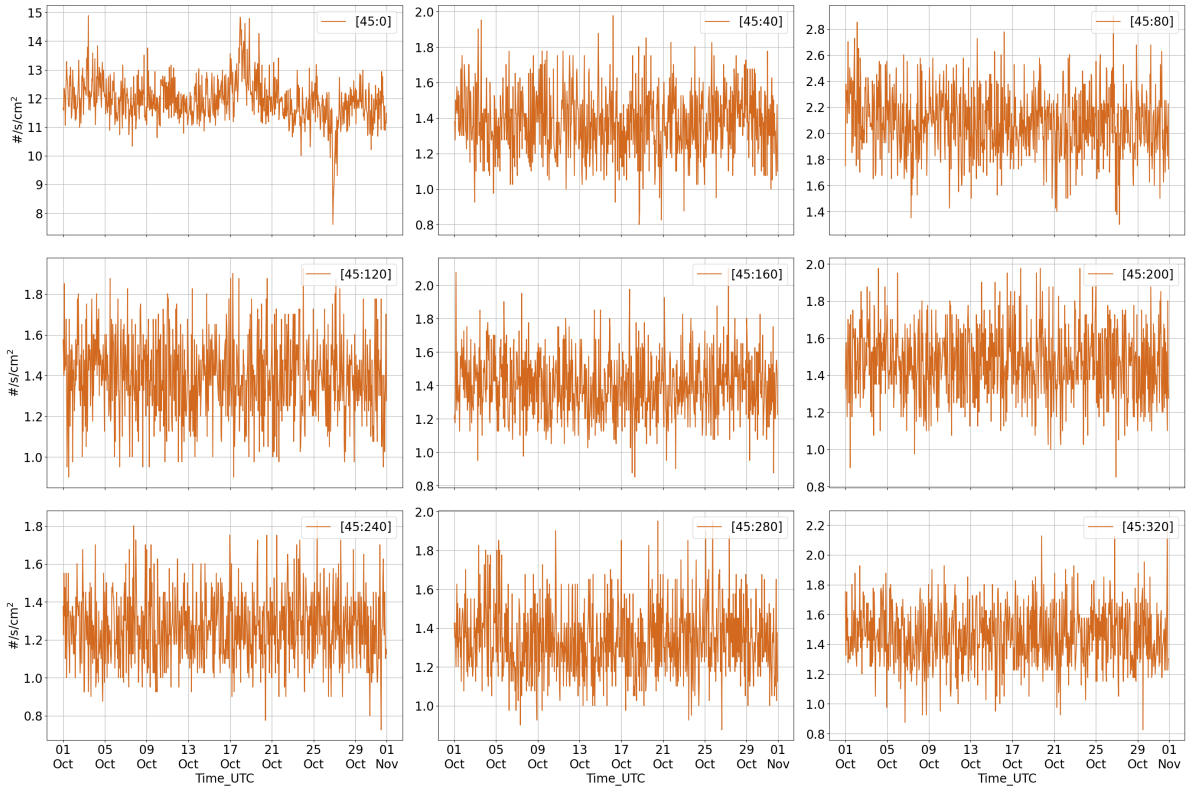


Figure B.3: Rate per unit area during the month of October for the nine azimuth sensors with zenith 45° of the DDH.

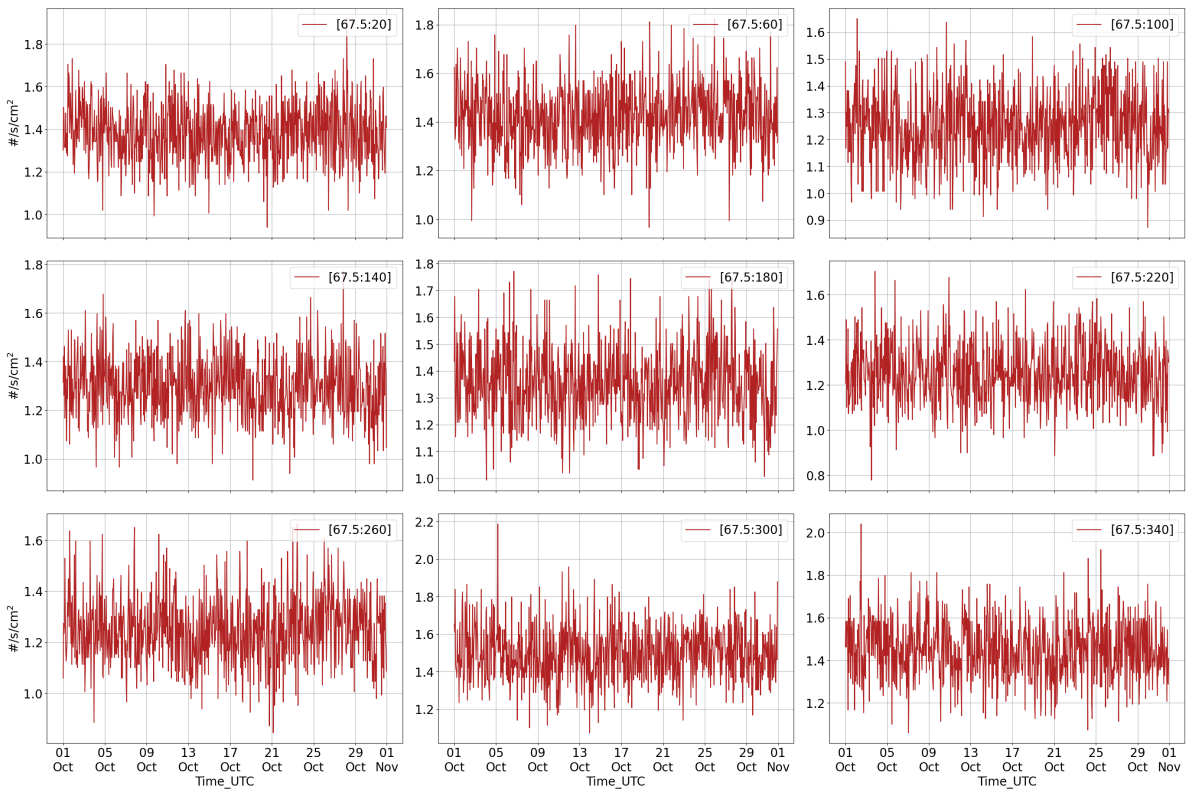


Figure B.4: Rate per unit area during the month of October for the nine azimuth sensors with zenith 67.5° of the DDH.

Correction factors

Table B.1: Correction factor computed for each DDH sensor (September, October and November).

Sensor	Correc. Factor (%)			Sensor	Correc.Factor (%)			Sensor	Correc. Factor (%)		
	Sep	Oct	Nov		Sep	Oct	Nov		Sep	Oct	Nov
22.5°:0°	-3.5	-2.0	-2.0	45°:0°	-	-	-	67.5°:20°	- 4.2	- 3.8	- 4.6
22.5°:40°	1.0	1.7	-0.1	45°:40°	1.4	1.2	1.9	67.5°:60°	- 7.7	- 6.5	- 6.8
22.5°:80°	8.9	8.4	9.3	45°:80°	-	-	-	67.5°:100°	5.8	6.2	5.6
22.5°:120°	9.3	8.6	9.3	45°:120°	0.6	0.0	-0.8	67.5°:140°	3.4	2.8	2.7
22.5°:160°	-0.7	1.0	-0.2	45°:160°	0.0	-0.3	-0.4	67.5°:180°	- 1.1	- 1.4	- 0.9
22.5°:200°	4.7	4.4	4.1	45°:200°	-4.8	-5.0	-5.5	67.5°:220°	7.1	6.2	6.4
22.5°:240°	-3.3	-4.3	-2.7	45°:240°	8.8	9.3	10.3	67.5°:260°	6.7	6.4	6.5
22.5°:280°	-5.2	-5.4	-4.4	45°:280°	2.8	3.9	3.9	67.5°:300°	-11.4	-12.2	-11.3
22.5°:320°	-8.7	-7.7	-8.9	45°:320°	-3.0	-4.1	-4.2	67.5°:340°	- 8.7	- 8.6	- 8.3
BKG 22.5°	-3.5	-4.8	-4.4	BKG 45°	-5.8	-5.0	-5.2	BKG 67.5°	10.1	10.9	10.7

Table B.2: Correction factor computed for each DDH sensor (December, January and February).

Sensor	Correc. Factor (%)			Sensor	Correc.Factor (%)			Sensor	Correc. Factor (%)		
	Dec	Jan	Feb		Dec	Jan	Feb		Dec	Jan	Feb
22.5°:0°	-2.2	-4.9	-1.8	45°:0°	-	-	-	67.5°:20°	- 4.9	- 3.8	- 4.3
22.5°:40°	0.3	3.1	1.3	45°:40°	1.8	1.6	1.1	67.5°:60°	- 7.5	- 7.5	- 8.4
22.5°:80°	8.8	8.5	10.0	45°:80°	-	-	-	67.5°:100°	5.6	5.6	6.8
22.5°:120°	7.4	8.9	8.4	45°:120°	-1.3	-1.7	-0.7	67.5°:140°	4.3	4.1	3.1
22.5°:160°	0.4	0.0	0.1	45°:160°	-1.4	0.3	0.0	67.5°:180°	- 0.4	- 1.8	- 1.4
22.5°:200°	5.0	4.2	3.8	45°:200°	-5.5	-5.6	-5.1	67.5°:220°	5.5	7.0	7.2
22.5°:240°	-4.1	-3.9	-4.3	45°:240°	11.2	9.7	9.7	67.5°:260°	6.6	6.0	7.5
22.5°:280°	-4.8	-4.8	-5.5	45°:280°	3.8	3.9	4.0	67.5°:300°	-11.5	-11.3	-11.7
22.5°:320°	-7.0	-7.7	-7.7	45°:320°	-3.6	-3.8	-3.3	67.5°:340°	- 8.2	- 8.4	- 8.8
BKG 22.5°	-3.8	-3.6	-4.4	BKG 45°	-5.1	-4.5	-5.7	BKG 67.5°	10.6	10.1	9.9

Table B.3: Correction factor computed for each DDH sensor (March and April).

Sensor	Correc. Factor (%)		Sensor	Correc.Factor (%)		Sensor	Correc. Factor (%)	
	Mar	Abr		Mar	Abr		Mar	Abr
22.5°:0°	-2.3	-3.2	45°:0°	-	-	67.5°:20°	- 5.0	- 5.7
22.5°:40°	0.9	0.8	45°:40°	2.6	2.2	67.5°:60°	- 7.9	- 7.2
22.5°:80°	9.2	8.9	45°:80°	-	-	67.5°:100°	6.0	5.9
22.5°:120°	8.7	9.6	45°:120°	0.1	-1.0	67.5°:140°	3.3	3.2
22.5°:160°	1.0	0.6	45°:160°	0.1	-0.7	67.5°:180°	- 2.0	- 1.1
22.5°:200°	4.5	5.6	45°:200°	-5.5	-6.0	67.5°:220°	6.7	7.4
22.5°:240°	-4.6	-4.8	45°:240°	8.7	8.2	67.5°:260°	6.2	5.8
22.5°:280°	-5.3	-4.1	45°:280°	2.9	3.8	67.5°:300°	-11.0	-11.8
22.5°:320°	-7.3	-9.9	45°:320°	-3.2	-2.5	67.5°:340°	- 7.4	- 7.8
BKG 22.5°	-4.7	-3.4	BKG 45°	-5.6	-3.8	BKG 67.5°	11.1	11.2

Bibliography

- [1] C. Plainaki *et al.* 'Planetary space weather: scientific aspects and future perspectives'. In: *Journal of Space Weather Space Climate* 6:A31 (2016).
- [2] J. A. Van Allen D. N. Baker. 'Revised Pioneer 10 absolute electron intensities in the inner Jovian magnetosphere'. In: *Journal of Geophysical Research* 82, 4 (1977), pp. 681–683.
- [3] J. A. Van Allen *et al.* 'Pioneer 11 observations of energetic particles in the jovian magnetosphere'. In: *Science* 188, 4187 (1975), pp. 459–462.
- [4] S. M. Krimigis *et al.* 'The Low Energy Charged Particle (LECP) experiment on the Voyager spacecraft'. In: *Space Science Reviews* 21 (1977), pp. 329–354.
- [5] E. Keppler *et al.* 'The ULYSSES energetic particle composition experiment EPAC'. In: *Astronomy and Astrophysics Supplement Series* 92, 2 (1992), pp. 317–331.
- [6] D. J. Williams *et al.* 'The Galileo Energetic Particles Detector'. In: *Space Science Reviews* 60 (1992), pp. 385–412.
- [7] S. J. Bolton *et al.* 'The JUNO Mission'. In: *Space Science Reviews* 213 (2017), pp. 5–37.
- [8] M. Pinto *et al.* 'Beam test results of the RADEM Engineering Model'. In: *Nuclear Instruments and Methods in Physics Research Section A: Accelerators, Spectrometers, Detectors and Associated Equipment* A 958 (2020).
- [9] J. Team. 'JUperiter ICy moons Explorer: Exploring the emergence of habitable worlds around gas giants'. In: *ESA/SRE(2014)* issue 1 (2014).
- [10] O. Grasset *et al.* 'JUperiter ICy moons Explorer (JUICE): An ESA mission to orbit Ganymede and to characterise the Jupiter system'. In: *Planetary and Space Science* 78 (2013), pp. 1–21.
- [11] J. Team. 'JUICE Environment Specification'. In: *JS-14-09* issue 5, rev 5 (2017).
- [12] ESA. *Juice's journey to Jupiter*. URL: https://www.esa.int/ESA_Multimedia/Images/2022/12/Juice_s_journey_to_Jupiter (visited on 22/11/2023).
- [13] M. F. Vogt *et al.* 'Solar Wind Interaction With Jupiter's Magnetosphere: A Statistical Study of Galileo In Situ Data and Modeled Upstream Solar Wind Conditions'. In: *Journal of Geophysical Research: Space Physics* 124 (2019), issue 12.
- [14] NOAA/NWS. *Solar Cycle Progression*. URL: <https://www.swpc.noaa.gov/products/solar-cycle-progression> (visited on 23/05/2024).

- [15] M. Pinto *et al.* 'The BepiColombo Environment Radiation Monitor, BERM'. In: *Space Science Reviews* 218, 54 (2022).
- [16] J. Rodríguez-Pacheco *et al.* 'The Energetic Particle Detector - Energetic particle instrument suite for the Solar Orbiter mission'. In: *Astronomy and Astrophysics Special Issue* 642, 7 (2019).
- [17] D. J. MacComas *et al.* 'Integrated Science Investigation of the Sun (ISIS): Design of the Energetic Particle Investigation'. In: *Space Science Reviews* 204 (2016), pp. 187–256.
- [18] L. Beringer *et al.* (Particle Data Group). 'Review of Particle Physics'. In: *Physical Review D*. 86, 010001 (2012).
- [19] T. Honig *et al.* 'Multi-point galactic cosmic ray measurements between 1 and 4.5 AU over a full solar cycle'. In: *Annales Geophysicae* 37 (2019), pp. 903–918.
- [20] E. Roussos *et al.* 'Long- and Short-term Variability of Galactic Cosmic-Ray Radial Intensity Gradients between 1 and 9.5 au: Observations by Cassini, BESS, BESS-Polar, PAMELA, and AMS-02'. In: *The Astrophysical Journal* 904 (2020), p. 165.
- [21] C. M. Jackman *et al.* 'Large-Scale Structure and Dynamics of the Magnetotails of Mercury, Earth, Jupiter and Saturn'. In: *Space Sci Rev* 182 (2014), pp. 85–154.
- [22] K. K. Khurana *et al.* 'The Configuration of Jupiter's Magnetosphere'. In: *Jupiter: The Planet, Satellites and Magnetosphere* Cambridge University Press (2004).
- [23] E. Roussos *et al.* 'The in-situ exploration of Jupiter's radiation belts'. In: *Experimental Astronomy* 54 (2021), pp. 745–789.
- [24] M. Pinto. 'Development of a Directionality Detector and Radiation Hardness Assurance for RADEM, the ESA JUICE mission Radiation Monitor'. PhD thesis. Universidade de Lisboa - Instituto Superior Técnico, 2019.
- [25] J. I. Vette D. M. Sawyer. 'AP-8 Trapped Proton Environment for Solar Maximum and Solar Minimum'. In: *NSSDC/WDC-A-R&S* 76-06 (1976).
- [26] J. I. Vette. 'The AE-8 Trapped Electron Model Environment'. In: *NSSDC/WDC-A-R&S* 91-24 (1991).
- [27] A. Sicard-Piet *et al.* 'JOSE: A New Jovian Specification Environment Model'. In: *IEEE Transactions on Nuclear Science* 58 (2011), pp. 923–931.
- [28] Q. Nénon *et al.* 'Pitch Angle Distribution of MeV Electrons in the Magnetosphere of Jupiter'. In: *Journal of Geophysical Research: Space Physics* 127 (Aug. 2022). doi: [10.1029/2022ja030627](https://doi.org/10.1029/2022ja030627). (Visited on 17/10/2022).
- [29] D. J. Williams. 'Energetic electron beams in Ganymede's magnetosphere'. In: *Journal of Geophysical Research* 109 (2004), A09211.
- [30] D. L. Chenette *et al.* 'Burst of Relativistic Electrons From Jupiter Observed in Interplanetary Space With the Time Variation of the Planetary Rotation Period'. In: *Journal of Geophysical Research* 79, 25 (1974), pp. 3551–3558.

- [31] B. J. Teegarden *et al.* 'Interplanetary MeV Electrons of Jovian Origin'. In: *Journal of Geophysical Research* 79, 25 (1974), pp. 3615–3622.
- [32] J. G. Mitchell *et al.* 'First Measurements of Jovian Electrons by Parker Solar Probe/ISoIS within 0.5 au of the Sun'. In: *The Astrophysical Journal* 933 (2022), pp. 171–178.
- [33] R. D. Strauss *et al.* 'Jovian Electrons in the Inner Heliosphere: Opportunities for Multi-spacecraft Observations and Modeling'. In: *The Astrophysical Journal* 961 (2024), pp. 57–70.
- [34] P. Dunzlaff *et al.* 'Jovian Electrons in the Inner Heliosphere: Opportunities for Multi-spacecraft Observations and Modeling'. In: *Journal Of Geophysical Research* 115 (2010), A10106.
- [35] NIST. *ESTAR - stopping-power and range tables for electrons*. URL: <https://physics.nist.gov/PhysRefData/Star/Text/ESTAR.html> (visited on 03/12/2023).
- [36] NIST. *PSTAR - stopping-power and range tables for protons*. URL: <https://physics.nist.gov/PhysRefData/Star/Text/PSTAR.html> (visited on 03/12/2023).
- [37] NIST. *ASTAR - stopping-power and range tables for helium ions*. URL: <https://physics.nist.gov/PhysRefData/Star/Text/ASTAR.html> (visited on 06/05/2024).
- [38] IDEAS (Integrated Detector Electronics AS). *Radiation Detection and Imaging*. URL: <https://ideas.no>.
- [39] T. A. Stein *et al.* 'Front-end readout ASIC for charged particle counting with the RADEM instrument on the ESA JUICE mission'. In: *Proc. SPIE 9905, Space Telescopes and Instrumentation 2016: Ultraviolet to Gamma Ray* (2016).
- [40] M. Pinto *et al.* 'Development of a Directionality Detector for RADEM, the Radiation Hard Electron Monitor Aboard the JUICE Mission'. In: *IEEE Transactions on Nuclear Science* 66 (2019), No. 7.
- [41] CERN. *GEANT4 A simulation toolkit, Physics Reference Manual Release 11.2*. 2023. URL: <https://geant4-userdoc.web.cern.ch/UsersGuides/PhysicsReferenceManual/fo/PhysicsReferenceManual.pdf>.
- [42] CERN. *GEANT4 A simulation toolkit, Book For Application Developers Release 10.7*. 2020. URL: <https://geant4-userdoc.web.cern.ch/UsersGuides/ForApplicationDeveloper/BackupVersions/V10.7/fo/BookForApplicationDevelopers.pdf>.
- [43] P. Gonçalves M. Pinto. 'GUIMesh: A tool to import STEP geometries into Geant4 via GDML'. In: *Computer Physics Communications* 239 (2019), pp. 150–156.
- [44] F. Rademakers R. Brun. 'ROOT - An Object Oriented Data Analysis Framework'. In: *Nuclear Instruments and Methods in Physics Research, A* 389 (1997), pp. 81–86.
- [45] A. Nymmik *et al.* 'INTERNATIONAL ISO STANDARD'. In: *Space Environment Technologies* (2004).
- [46] M. Pinto *et al.* 'Parametric evaluation of the SEE rate on the SEU and SEL monitors aboard the Alphasat using the IRPP model'. In: *IEEE Transactions on Nuclear Science* 70, 8 (2023), pp. 1821–1828.

[47] Royal Observatory of Belgium. *Sunspot Index and Long-term Solar Observations*. URL: <https://www.sidc.be/SILSO/> (visited on 29/04/2023).